Remote Sensing of Environment 302 (2024) 113963

Contents lists available at ScienceDirect

Remote Sensing of Environment

journal homepage: www.elsevier.com/locate/rse

Review

Continuity between NASA MODIS Collection 6.1 and VIIRS Collection 2 land products

Miguel O. Román [a,*], Chris Justice [b], Ian Paynter [a,*], Peter B. Boucher [a], Sadashiva Devadiga [c], Arthur Endsley [e], Angela Erb [f], Mark Friedl [g], Huilin Gao [h], Louis Giglio [b], Josh M. Gray [i,j], Dorothy Hall [k,l], Glynn Hulley [m], John Kimball [e], Yuri Knyazikhin [g], Alexei Lyapustin [n], Ranga B. Myneni [g], Praveen Noojipady [c,d], Jiabin Pu [g], George Riggs [l,d], Sudipta Sarkar [c,d], Crystal Schaaf [f], Deep Shah [h], Khuong H. Tran [o], Eric Vermote [c], Dongdong Wang [b], Zhuosen Wang [c,k], Aisheng Wu [d], Yongchang Ye [o], Yu Shen [o], Shuai Zhang [h], Shuai Zhang [f], Xiaoyang Zhang [o], Maosheng Zhao [c,d], Carol Davidson [c,d], Robert Wolfe [c]

[a] Leidos, Inc, 1750 Presidents St, Reston, VA 20190, USA
[b] Department of Geographical Sciences, University of Maryland, 2181 LeFrak Hall, College Park, MD 20742, USA
[c] Terrestrial Information Systems Laboratory, Code 619, NASA/Goddard Space Flight Center, 8800 Greenbelt Road, Greenbelt, MD 20771, USA
[d] Science Systems and Applications (SSAI), Inc, 10210 Greenbelt Rd, Lanham, MD 20706, USA
[e] Numerical Terradynamic Simulation Group, The University of Montana, 32 Campus Drive, Missoula, MT 59812, USA
[f] School for the Environment, University of Massachusetts Boston, 100 Morrissey Blvd, Boston, MA 02125, USA
[g] Department of Earth and Environment, Boston University, 685 Commonwealth Ave, Boston, MA 02215, USA
[h] Department of Civil and Environmental Engineering, Texas A&M University, 3136 TAMU, 201 Dwight Look, College Station, TX 77843, USA
[i] Department of Forestry and Environmental Resources, NC State University, 2800 Faucette Dr, Raleigh, NC 27695, USA
[j] Center for Geospatial Analytics, NC State University, 2800 Faucette Dr, Raleigh, NC 27695, USA
[k] Earth System Science Interdisciplinary Center (ESSIC), University of Maryland, 5825 University Research Court, Suite 4001, College Park, MD 20740, USA
[l] Cryospheric Sciences Laboratory, Code 615, NASA/Goddard Space Flight Center, Greenbelt, MD 20771, USA
[m] Jet Propulsion Laboratory, California Institute of Technology, 4800 Oak Grove Dr, Pasadena, CA 91109, USA
[n] Climate and Radiation Laboratory, Code 613, NASA/Goddard Space Flight Center, 8800 Greenbelt Road, Greenbelt, MD 20771, USA
[o] Geospatial Sciences Center of Excellence, Department of Geography and Geospatial Sciences, South Dakota State University, 1101 Medary Ave., Brookings, SD 57007, USA

ARTICLE INFO

Edited by Zhe Zhu

Keywords:
MODIS
VIIRS
Continuity
Satellite
NASA

ABSTRACT

This paper provides a review and summary status of the research underway by the NASA Terra Aqua Suomi-NPP Land Discipline Team to provide continuity of global land data products from the NASA Moderate resolution Imaging Spectroradiometer (MODIS) to the Visible Infrared Imaging Radiometer Suite (VIIRS). The two MODIS instruments on the NASA Earth Observing System Terra (morning overpass) and Aqua (afternoon overpass) platforms have provided more than twenty years of data. The peer-reviewed land products generated from MODIS are now being transitioned to production using VIIRS inputs, with the intention of providing dynamic continuity for the Aqua observations. As part of that process, the products from the two instruments are undergoing intercomparison and evaluation. These results are provided where available and show promising levels of agreement and accuracy in all cases. The paper also offers options for establishing continuity of Terra MODIS data products.

1. Introduction

The Moderate Resolution Imaging Spectroradiometer (MODIS) is the primary global imager on the Terra and Aqua platforms, which are the flagship missions for the National Aeronautics and Space Administration (NASA) Earth Observing System (EOS). For >20 years, MODIS

* Corresponding authors.
E-mail addresses: miguel.o.roman@leidos.com (M.O. Román), ian.l.paynter@leidos.com (I. Paynter).

https://doi.org/10.1016/j.rse.2023.113963
Received 8 August 2023; Received in revised form 18 November 2023; Accepted 16 December 2023
Available online 3 January 2024

instruments have provided views of the entire surface of Earth every 1–2 days at resolutions ranging from 250 m to 1 km (Salomonson et al., 2006). However, plans are now being developed for the end-of-life of the Terra and Aqua MODIS platforms and the continuity of the MODIS data products. In this review, continuity describes the persistence or functional replacement of each MODIS product beyond the end-of-life of Terra and Aqua MODIS platforms, and this review focuses on the status of the research underway by the NASA Terra, Aqua, and Suomi National Polar-orbiting Partnership (TASNPP) Land Discipline Team to directly achieve continuity of global land data products from MODIS, primarily by using the Visible Infrared Imaging Radiometer Suite (VIIRS). In the broader context, Essential Climate Variables (ECVs) derived from MODIS will achieve continuity from a variety of sources and methods.

The NASA EOS was designed to meet the observation needs for Mission to Planet Earth, a program initiated in the 1990s to focus scientific efforts on earth observation. The EOS satellite missions included numerous spaceborne sensors designed to study different aspects of the Earth system and provide satellite observations to advance Earth System Science. This unprecedented program of observations, data systems, and science has made an outstanding contribution to understanding the Earth System (King and Platnick, 2018). The flagship missions for EOS are the Terra platform, with a 10:30 AM overpass time and launched on December 18th, 1999, and the Aqua platform, with a 1:30 PM overpass and launched on May 4th, 2002. These two large platforms (6.8 × 3.5 m) included five and six instruments, respectively. The MODIS is the primary global imager on both platforms, providing near-daily coverage at resolutions ranging from 250 m to 1 km (Salomonson et al., 2006). The MODIS instrument was designed to meet the observation needs for monitoring and characterizing the land, atmosphere, and oceans. As a science instrument, considerable attention has been given to calibration (Xiong and Barnes, 2006). The MODIS instruments were designed with a nominal five-year life but are still operating >20 years later, which is a testament to the quality of the instrument design and engineering (Xiong et al., 2020; Parkinson, 2022).

For the land community, the MODIS instruments built on the heritage of the National Oceanic and Atmospheric Administration (NOAA) Advanced Very High Resolution Radiometer (AVHRR) and the Landsat instruments. At the time, MODIS represented a significant boon for observations thanks to the rich selection of spectral bands, useful spatial resolution, and high-quality geometric and radiometric performance (Justice et al., 1998). An important requirement for the MODIS instrument team was the generation of peer-reviewed, standard data products designed to meet the needs of the broader science and applications communities. For each standard product (Table 1), a peer-reviewed Algorithm Theoretical Basis Document (ATBD) and User Guide were generated, and a significant investment was made in Quality Assurance (QA), product accuracy assessment (validation), and uncertainty characterization (Justice et al., 2002; Morisette et al., 2002; Masuoka et al., 2011; MODIS Land, 2023a).

The MODIS land products have undergone incremental improvements and full-record reprocessing through six major collections and have been made easily accessible through the NASA Distributed Active Archive Centers. The use of the data products from MODIS and number of publications (>22,000) have been unprecedented for NASA's Earth Science program (https://modis.gsfc.nasa.gov/sci_team/pubs/). The longevity of the program and the reliability of the data stream has meant that a long-term data record has been developed with sufficient duration to create a climate record, enabling time-series research on land surface changes and trends (e.g., Zubkova et al., 2022; Roy et al., 2022). This research is particularly important as the global climate is changing and extreme weather events are occurring with increasing frequency, providing a strong case for continuing this data record. MODIS data are now integrated into numerous science data analysis and modeling frameworks, and numerous applications have been developed using the MODIS products in operational monitoring systems by the United States Department of Agriculture (USDA), the United States Forest Service (USFS), and many other agencies around the world. Because of the development of operational decision support systems that are dependent on MODIS, there is a strong interest in data continuity.

Table 1
MODIS and VIIRS products discussed in this continuity study.

Product Description	MODIS Products[1, 2]	VIIRS Products[2, 3]
Surface Reflectance	MOD09	VNP09
Leaf Area Index (LAI) and the Fraction of Photosynthetically Active Radiation (FPAR)	MCD15	Vxx15
Downward Shortwave Radiation (DSR) and Photosynthetically Active Radiation (PAR)	MCD18	Vxx18
Evapotranspiration (ET)	MxD16	Vxx16
Global Land Surface Phenology (LSP)	MCD12	VNP22
Gross Primary Production (GPP) and Net Primary Production (NPP)	MxD17	Vxx17
Land Surface Temperature and Emissivity (LST&E)	MxD11, MxD21	Vxx21
Surface Products derived using Multi-Angle Implementation of Atmospheric Correction (MAIAC)	MCD19	VCD19
Global Water Reservoir (GWR)	MxD28	Vxx28
Normalized Difference Snow Index (NDSI) and Cloud-gap Filled Snow-Cover Extent (SCE)	MOD10	VNP10
Burned Area	MCD64	Vxx64
Bidirectional Reflectance Distribution Function (BRDF), Nadir BRDF-Adjusted Reflectance (NBAR), and Albedo	MCD43	Vxx43

[1] A prefix of "MOD" indicates a product from Terra MODIS, and "MCD" indicates a product from the combination of Terra and Aqua MODIS.
[2] Lower-case x is used as a wildcard in product names to indicate that the product name is a reference to multiple child products.
[3] A prefix of "VNP" indicates a product from SNPP VIIRS; "VJ1" indicates a product from JPSS-1 VIIRS; and "VCD" indicates a product from the combination of SNPP and JPSS-1 VIIRS.

Such is the value of MODIS data across many scientific communities that data collection will continue even as the orbits of Terra and Aqua drift during their terminal stages. The drifting of Terra and Aqua from their established orbits will impact the viewing angle, distances, and overpass time of MODIS observations. While there are potential implications of orbital drift for certain MODIS land products, as discussed in this review, the changes in observation characteristics at the end of such a lengthy data record may also offer unique insights. The opportunities for novel research afforded by continuing MODIS observations during orbital drift are a topic of discussion in the Earth observation and land remote sensing communities, facilitated by NASA's solicitation of input and coordination of a dedicated workshop.

Consistent long-term satellite data records such as from MODIS require close attention to instrument calibration and performance. For example, the NOAA AVHRR long-term record consisted of data from successive NOAA satellites with multiple versions of the same instrument, requiring cross-calibration (Vermote and Kaufman, 1995; Cao et al., 2004, 2008; Kalluri et al., 2021). Development of a long-term data record using AVHRR and MODIS data is described by Pedelty et al. (2007). The Landsat data record, which started in 1972, also consists of data from different incarnations of the Landsat instruments, which have been modified as the technology and user needs have evolved. Such dynamic data continuity between instruments requires extensive and careful cross-calibration and data characterization between them, and these are reviewed here for MODIS land data products.

The NASA MODIS instruments were originally designed to meet research needs and were never considered as operational; but with their longevity, their use has evolved as they continue to provide long-term data records. The Integrated Program Office, initially through the NPOESS Preparatory Project (NPP) (NASA, NOAA, DoD) and subsequently with NPOESS/JPPS (NASA, NOAA), had the vision to include many of the capabilities of the MODIS instrument in the design and requirements for VIIRS, which was also intended to follow up on the

AVHRR (Murphy, 2006). As such, VIIRS is a natural data source for continuity of many MODIS land products and exemplifies a successful transition from research to operations, particularly for the land discipline (Justice et al., 2013) (Fig. 1). VIIRS instruments are currently operating on SNPP (launched in 2011) (Justice et al., 2013), NOAA-20 (launched in 2017), and NOAA-21 (launched in November 2022).

A comparison of the MODIS and VIIRS instruments is shown in Table 2. The VIIRS imager instrument, although different from MODIS in design and sensor characteristics, provides dynamic continuity of global coverage at coarse resolution (375 m to 750 m) with some comparable spectral bands (Vis, NIR, SWIR, and Thermal) and radiometric resolution. In some respects, VIIRS offers enhancements over the MODIS instrument. For example, VIIRS was originally designed to meet Department of Defense requirements, which led to new features, including: a uniform pixel size from resampling across the scan, the higher spatial resolution of the I-Band (375 m) for fire monitoring and land surface temperature estimation, and the additional Day/Night Band (DNB) for night-light detection. As is the case for MODIS and VIIRS, long-serving data sources are frequently replaced by more technologically advanced instruments and missions that may have

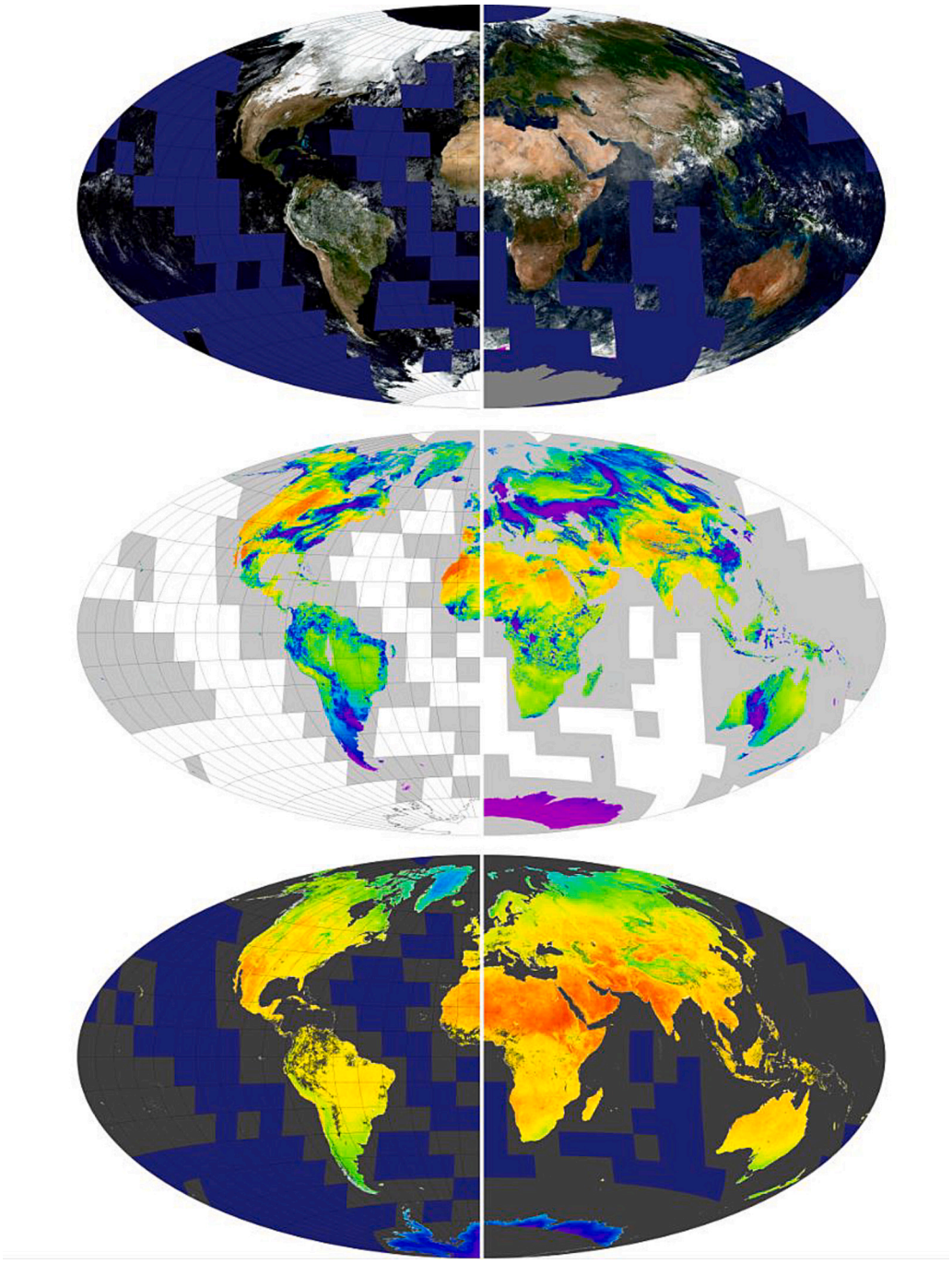

Fig. 1. Examples of MODIS images (left side) paired with their VIIRS counterparts (right side) from the Land Data Operational Product Evaluation (LDOPE) Global Browse, providing a visual demonstration of the general compatibility between MODIS and VIIRS. From top to bottom the product pairs are false-colour based on Surface Reflectance from MODIS (MYD09A1, bands 1, 4, and 3) and VIIRS (VNP09A1, bands M5, M4, and M3); Downward Shortwave Radiation from MODIS (MCD18A1) and VIIRS (VNP18A1); and 8-day Land Surface Temperature from MODIS (MOD11A2) and VIIRS (VNP21A2), used instead of the base daily products for more complete global coverage.

Table 2
A comparison of MODIS and VIIRS instrument bands.

MODIS			VIIRS		
Band[1]	Spectral Range [μm]	Spatial Resolution [m]	Band[2]	Spectral Range [μm]	Spatial Resolution [m]
1	0.620–0.670	250	I1	0.600–0.680	375
			M5	0.662–0.682	750
2	0.841–0.876	250	I2	0.850–0.880	375
			M7	0.846–0.885	750
3	0.459–0.479	500	M3	0.478–0.488	750
4	0.545–0.565	500	M4	0.545–0.565	750
5	1.230–1.250	500	M8	1.230–1.250	750
6	1.628–1.652	500	I3	1.580–1.640	375
			M10	1.580–1.640	750
8	0.405–0.420	1000	M1	0.402–0.422	750
9	0.438–0.448	1000	M2	0.436–0.454	750
10	0.438–0.493	1000	M2	0.436–0.454	750
			M3	0.478–0.488	750
12	0.546–0.556	1000	M4	0.545–0.565	750
13	0.662–0.672	1000	I1	0.600–0.680	375
			M5	0.662–0.682	750
14	0.673–0.683	1000	I1	0.600–0.680	375
			M5	0.662–0.682	750
15	0.743–0.753	1000	M6	0.739–0.754	750
16	0.862–0.877	1000	I2	0.850–0.880	375
			M7	0.846–0.885	750
20	3.660–3.840	1000	I4	3.550–3.930	375
			M12	3.610–3.790	750
21	3.929–3.989	1000	I4	3.550–3.930	375
			M13	3.970–4.130	750
22	3.929–3.989	1000	I4	3.550–3.930	375
			M13	3.970–4.130	750
23	4.020–4.080	1000	M13	3.970–4.130	750
26	1.360–1.390	1000	M9	1.371–1.386	750
29	8.400–8.700	1000	M14	8.400–8.700	750
31	10.780–11.280	1000	I5	10.500–12.400	375
			M15	10.260–11.260	750
32	11.770–12.270	1000	I5	10.500–12.400	375
			M16	11.540–12.490	750

[1] MODIS bands that do not have any overlap with VIIRS bands are not included in the table.
[2] VIIRS bands that do not have any overlap with MODIS bands are not included in the table.

objectively better specifications. Regardless, any change in instrument characteristics or performance requires effort to achieve consistency between the original and replacement data products. Numerous studies have examined the relationship between the MODIS and VIIRS instruments (e.g., Skakun et al., 2018; Hall et al., 2019; Benedict et al., 2021; Lyapustin et al., 2023), and recent efforts to create long-term and successful continuity between MODIS and VIIRS at the data product level are summarized and described here.

Relevant considerations for continuity between MODIS and VIIRS go beyond the instrument specifications and performance to include observation characteristics such as overpass time, viewing conditions, and repeat frequency. For MODIS, the morning and afternoon overpass times together provide some ability to sample the diurnal cycle of surface phenomena, an improved sampling of sun/surface viewing conditions, and increased opportunity for cloud free observations. Hence, the morning and afternoon data from Terra and Aqua MODIS are included in the Fire, BRDF/Albedo, Land Surface Temperature and Emissivity (LST&E), and Leaf Area Index (LAI) products, and the loss of the combination of a morning and afternoon overpass presents a challenge for continuity of these products. For the Terra AM overpass, there is no planned NASA or NOAA mission that could provide continuity. A variety of options for ensuring data continuity for Terra are proposed in Section 3. For the afternoon orbit continuity is ensured through to at least 2037, with JPSS-4 and its VIIRS instrument due for launch in 2032.

The rest of the review is structured as follows. Section 2 discusses the cross-calibration efforts necessary to allow VIIRS products to provide continuity for MODIS products. Section 3 details the approach to quality control, validation, and assessment of continuity between MODIS and VIIRS. Section 4 provides a series of subsections about the state of continuity on a product-by-product basis, providing information on the derivation algorithms for the product, any available validation of continuity, the status of continuity efforts, and the potential impacts of the drifting orbits of the Terra/Aqua MODIS satellites. Readers interested in the continuity status of a particular MODIS product may wish to focus their attention on the relevant subsection of Section 4, then proceed to Section 5 for a discussion of the options for MODIS product continuity other than VIIRS, and finally to Section 6 for summarizing conclusions. To aid the reader in understanding the relevant work for each section, the primary authors for sections and subsections are provided throughout.

2. Cross-calibration of VIIRS with MODIS

Primary authors: Eric Vermote and Aisheng Wu.

2.1. Introduction to cross-calibration

Cross-calibration analyses can be powerful tools to achieve continuity, helping to ensure accuracy of data products and time-series analyses. Cross-calibration analyses consist of band-to-band comparisons between remote sensing instruments and ground-truth sites, recalibrating those datasets such that their values better match a reference dataset. As the Terra and Aqua satellites carrying the MODIS instruments approach their end-of-life, a cross-calibration analysis was performed to demonstrate the ability of VIIRS instruments to continue the long-term data record collected by MODIS.

The relative accuracy of the MODIS and VIIRS instruments is around ±2% compared to ground-truth data (Xiong et al., 2007). Thus, the

differences between data from these sensors can be as large as 4%. For example, even the different VIIRS instruments on-board the SNPP and NOAA-20 satellites show differences of 2% to 6.5% before calibration (Fig. 2), a level of uncertainty that could affect many scientific applications in the transition from MODIS to VIIRS (Lyapustin et al., 2014a, 2014b). To ensure the accurate continuity between MODIS and VIIRS, data from the different MODIS and VIIRS instruments and further calibrated datasets was evaluated to ensure that their raw values agree to within the required margin of 1% (Wang et al., 2012).

2.2. Methodology for cross-calibration

To achieve cross-calibration, the VIIRS calibration procedure was adjusted such that the VIIRS data better matched with MODIS Aqua datasets. The VIIRS datasets were recalibrated, rather than those from MODIS, since VIIRS has a shorter data record than MODIS and therefore involved substantially less effort than would re-processing the extensive MODIS data record.

VIIRS and MODIS are generally calibrated to a global network of benchmarking sites known as Benchmark Land Multisite Analysis and Intercomparison of Products (BELMANIP2) (Baret et al., 2006). The BELMANIP2 sites provide a standard network of validation sites for earth observation data that are spread across a variety of continents and biomes.

We aimed to adjust the VIIRS calibration such that it matched that of MODIS. However, there are differences in the spectral response of the VIIRS and MODIS instruments that did not allow for a direct adjustment of the VIIRS calibration on the BELMANIP2 sites (Fig. 2). Therefore, our approach relied on three different techniques: (1) The near-infrared (NIR) VIIRS I2 band and MODIS band 2, which are spectrally similar (Fig. 3), were directly cross-calibrated on the BELMANIP2 sites on a monthly basis; (2) The VIIRS NIR adjusted calibration was transferred to the VIIRS visible bands by comparing data collected over Deep Convective Clouds (DCC) (Doelling et al., 2011, 2012; Vermote and Kaufman, 1995), areas of dense cloud cover with very high spectral reflectance; (3) The adjusted VIIRS NIR calibration equation was transferred to the VIIRS short wave infrared (SWIR) bands by comparing data from sun-glint observations (Vermote and Kaufman, 1995).

2.3. BELMANIP2 sites cross-calibration

Fig. 4 shows the ratio between MODIS Aqua (Collection 6.1) and VIIRS monthly data after the VIIRS calibration described in the previous section for the NIR band (I2 for VIIRS and M2 for MODIS). Seasonal variations exist, but they are very small (about ±0.5%). There are also small, long-term trends (0.1% per year). In summary, the potential residual uncertainty is acceptable given the improvement from the original 4% magnitude of differences (Fig. 2).

2.4. Visible/NIR intercalibration using deep convective clouds (DCCs)

Following a similar calibration approach to that used by Vermote and Kaufman (1995), data from high altitude DCCs over the Pacific Ocean were used to derive monthly average ratios between the visible and the NIR VIIRS bands. Fig. 5 shows the ratios for the VIIRS red band (I1) for both SNPP and NOAA-20. The monthly variation was about ±0.5%, which was similar to the magnitude of variability observed by Vermote and Kaufman (1995), demonstrating that this method is a very robust way to transfer the NIR calibration. The same results were observed in other visible bands (not shown here).

2.5. SWIR/NIR intercalibration using sun glint

Sun-glint observations over high-altitude Lake Titicaca were used to intercalibrate the SWIR bands to the NIR bands, following an approach similar to that of Vermote and Kaufman (1995). We used sun-glint observations instead of DCC observations, because DCC are not white in the SWIR spectral region. Fig. 6 shows the results for each SWIR band (MODIS: M8, M10, M11; VIIRS: I3). Despite the reduced number of cases analyzed (there were limited numbers of suitably strong sun-glint occurrences available), the relative stability of the intercalibration ratio (±1%; Fig. 7) showed that this was a viable technique for calibrating the SWIR bands.

2.6. Summary

Table 3 summarizes the cross-calibration coefficients to be applied for the VIIRS data. The cross-calibration coefficients in Table 3 can be applied to an observed reflectance value of y to adjust it to its calibrated value of y' by the equation $y' = y(A + Bx(Year - C))$ where A, B, and C are constants, x is the wavelength in nanometers, and $Year$ is the year of the observation. In general, those adjustment coefficients are well within the uncertainty of the absolute calibration of the VIIRS instruments (±4%). These coefficients are also comparable in the visible to NIR range, which is consistent with what is expected from the absolute calibration error budget. Given the agreement between MODIS and VIIRS exceeded that between the VIIRS instruments, this analysis confirms the viability and the high accuracy of using VIIRS to continue the MODIS data record.

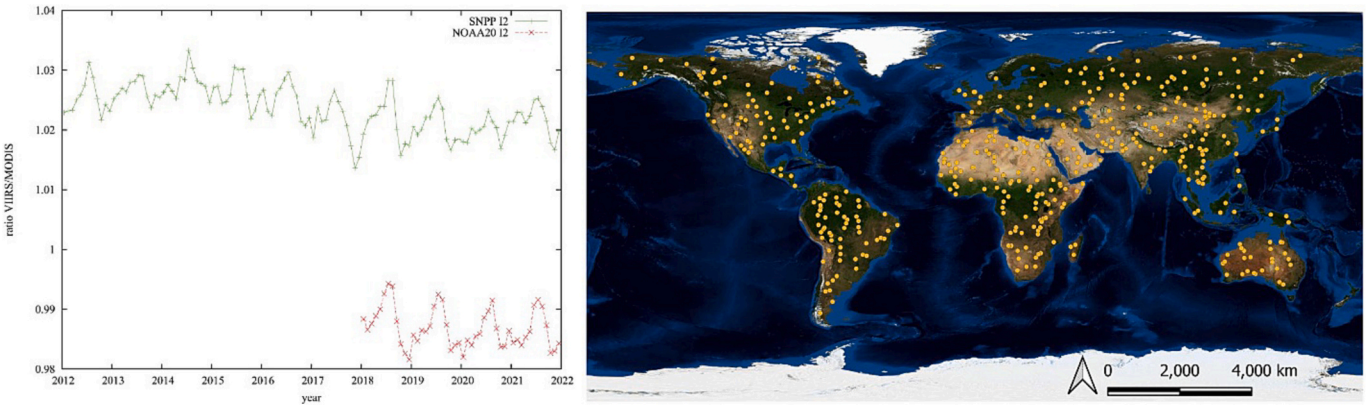

Fig. 2. Monthly cross comparison of the VIIRS (green: SNPP, red: NOAA-20) and MODIS Aqua SR products (left side) for the BELMANIP2 sites (orange dots on the map right side) prior to VIIRS calibration described in section 2.2. It should be noted that since these were not top-of-atmosphere observations, the observed bias could have been influenced by spectral response differences. (For interpretation of the references to colour in this figure legend, the reader is referred to the web version of this article.)

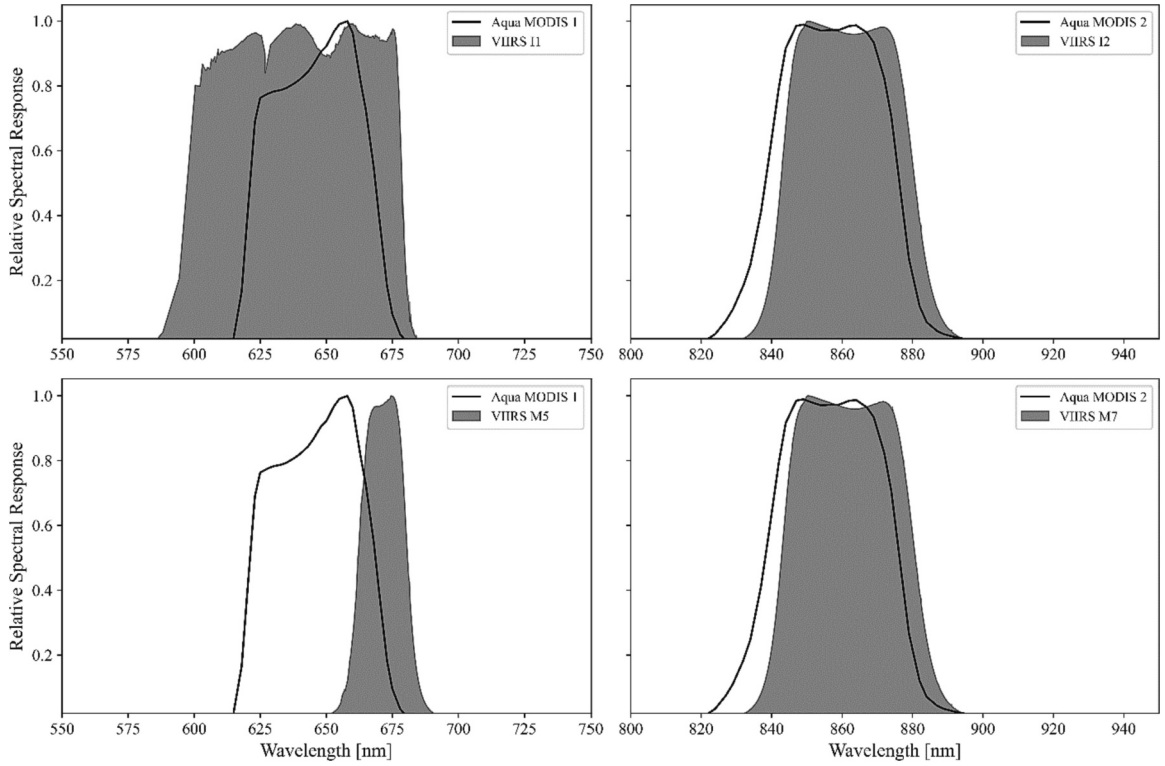

Fig. 3. Relative spectral response functions for MODIS/Aqua and VIIRS sensors in the red and NIR spectral domain. (For interpretation of the references to colour in this figure legend, the reader is referred to the web version of this article.)

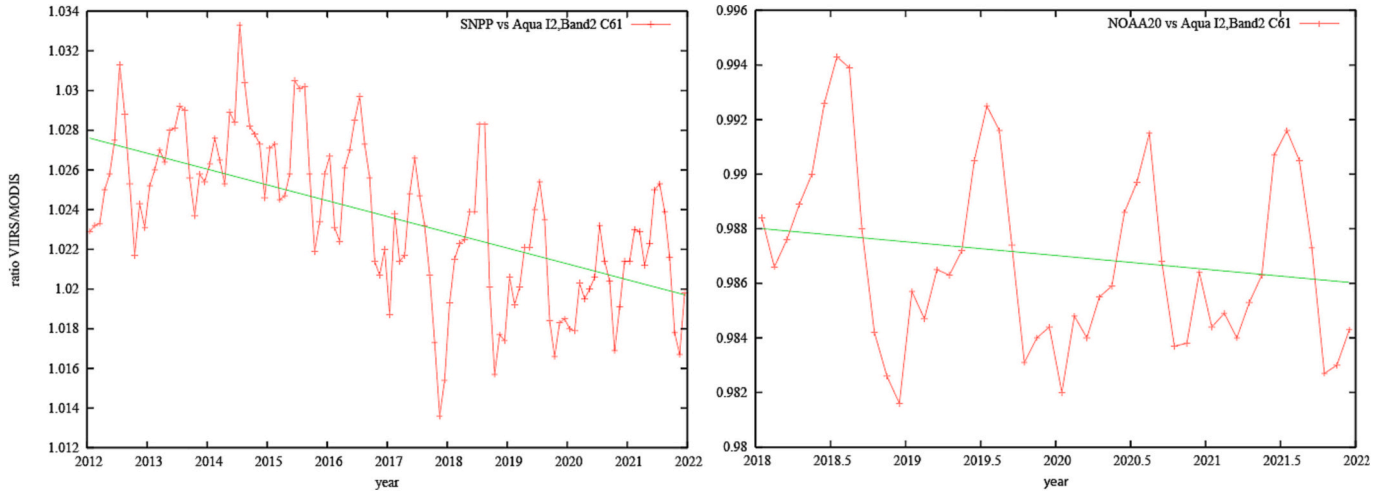

Fig. 4. Cross comparison of VIIRS after calibration as described in section 2.2 with MODIS Aqua in the NIR over BELMANIP2 sites for SNPP (left) and NOAA-20 (Right). The green line is the long-term trend. (For interpretation of the references to colour in this figure legend, the reader is referred to the web version of this article.)

3. Assessment of continuity of remote sensed land data products from C61 MODIS to C2 VIIRS by the MODIS/VIIRS Land Data Operational Product Evaluation (LDOPE) team

Primary authors: Sadashiva Devadiga, Sudipta Sarkar, and Praveen Noojipady. This section is relevant to MODIS and VIIRS products discussed in this continuity study.

3.1. Introduction: remotely sensed product quality assessment

The Land Data Operational Product Evaluation (LDOPE) Facility, established at the time of launch of NASA's EOS Terra mission in 1999, has functioned as the centralized facility assisting the NASA land science team in assessing the quality of the land data products generated at the NASA MODIS Science Investigator-led Processing System (MODIS SIPS, also known as MODAPS) by processing MODIS data from Terra and subsequently from MODIS on Aqua (launched in 2002). There were five collection reprocessing events of the MODIS products prior to establishing the NASA VIIRS Land SIPS in 2016. LDOPE has been instrumental in ensuring the scientific quality and collection-level consistency of these products, using matured and proven quality assessment (QA) tools and processes designed and implemented in-house at the LDOPE

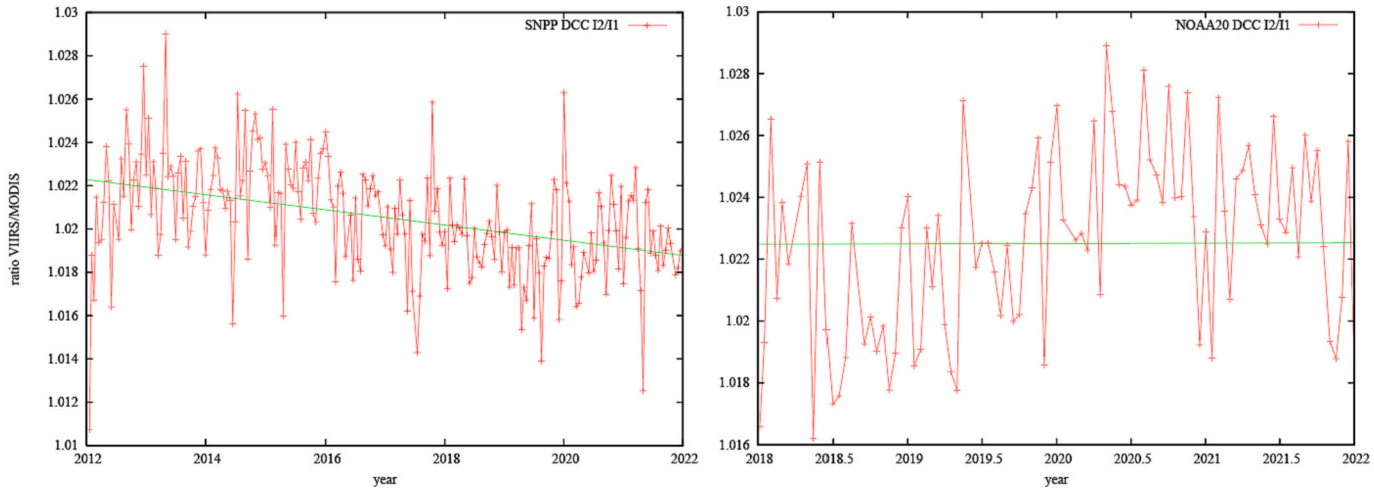

Fig. 5. Ratios of VIIRS Red (I1) with NIR (I2) over Deep Convective Clouds for SNPP (left) and NOAA-20 (right). The green line shows the long-term trend. (For interpretation of the references to colour in this figure legend, the reader is referred to the web version of this article.)

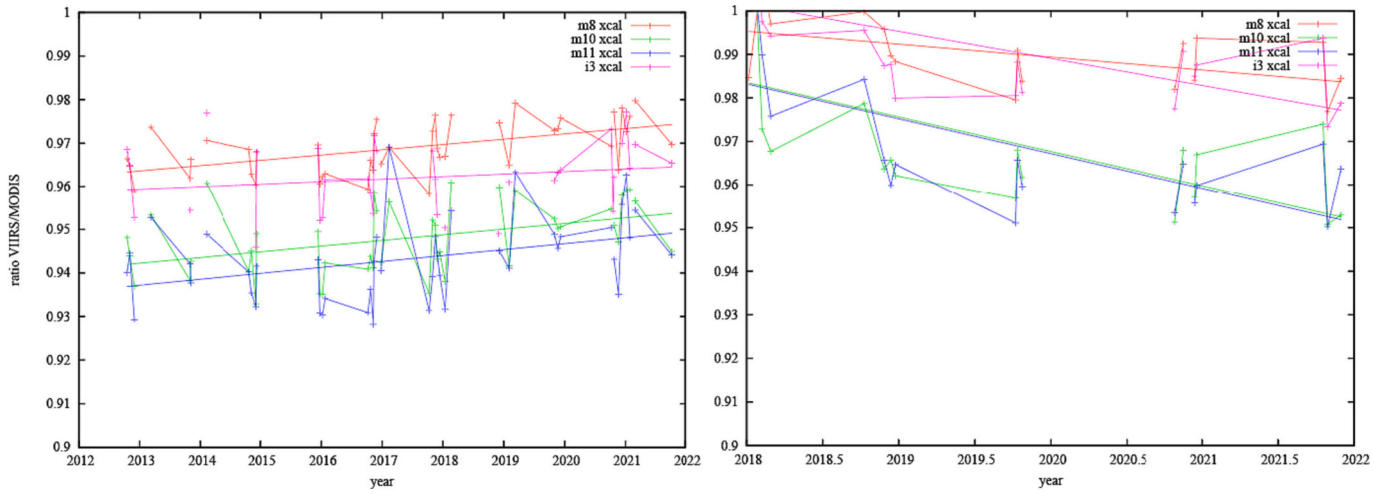

Fig. 6. Intercalibration ratios derived over Sun Glint for the VIIRS SWIR bands, SNPP (left), NOAA-20 (right).

(Roy et al., 2002, Masuoka et al., 2011). With the creation of NASA VIIRS products from SNPP and NOAA-20, the LDOPE revised its QA approaches, changing them from an independent assessment of MODIS products alone to a relative assessment of VIIRS product quality in comparison to heritage MODIS products, specifically for MODIS Aqua. The LDOPE has recently extended its QA approach to provide assessments of continuity from current collection versions of MODIS (C61) and VIIRS (C2) products.

3.2. Approach to sensor cross-calibration for MODIS and VIIRS

As discussed under the section for "Cross-Calibration of VIIRS with MODIS", a post-launch vicarious calibration was carried out by using ground sites observed in quick succession by the instruments to ensure the agreement of SNPP and NOAA-20 raw values to within the required margin of 1%, using the MODIS Aqua as the reference instrument. The consistency of this calibration, across the respective mission periods of SNPP and NOAA-20, was confirmed by LDOPE, based on a sampling of cross-calibrated TOA radiance values, spread across the respective mission periods. Two sets of atmospherically corrected land surface reflectance products were generated based on L1B TOA radiance values, one set with and one without the application of cross-calibration. A Ross Thick-Li Sparse based BRDF correction (Strahler et al., 1999) was applied to reflectance values that are within +/− 60° of nadir to minimize differences caused by sensor viewing geometries. Following that, normalized land surface reflectance values were generated for SNPP and NOAA-20, using MODIS Aqua as the reference, and these were aggregated over the benchmark BELMANIP2 sites. Plots of these normalized reflectance values show that the pre-calibration differences of up to 4% between the two VIIRS platforms (Fig. 6) were constrained to within 1% following the application of this vicarious cross-calibration (Fig. 7). Both SNPP and NOAA-20 values were also seen to come in closer alignment with MODIS Aqua, demonstrating a high degree of continuity from MODIS to VIIRS.

3.3. Verification of continuity from C61 MODIS to C2 VIIRS

LDOPE generates and maintains complete records of time series summary statistics derived from all the gridded MODIS and VIIRS Land products at fixed globally distributed locations. Such records provide a synoptic overview of retrieval performances across surface types, sun-surface-sensor geometries, and atmospheric conditions that can change temporally. It also allows for monitoring of any change in instrument characterization and calibration. These globally distributed fixed locations comprise nine MODIS 10 × 10° tiles that are expected to be representative of certain land cover and biome types and are referred

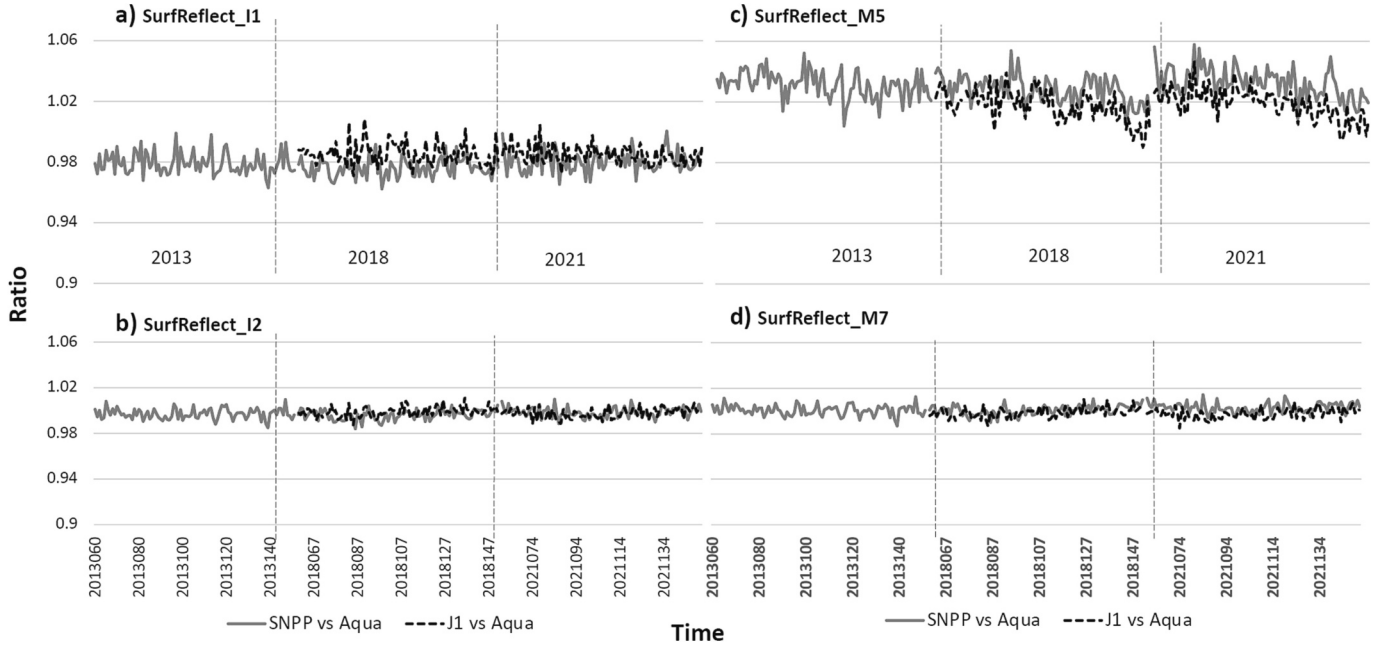

Fig. 7. C2/VIIRS Cross-Calibrated Reflectance comparison to C61/Aqua across all BELMANIP sites representing years 2013, 2018, and 2021 for SurfReflect_I1 (panel a), SurfReflect_I2 (panel b), SurfReflect_M5 (panel c), and SurfReflect_M7 (panel d) channels. (For interpretation of the references to colour in this figure legend, the reader is referred to the web version of this article.)

Table 3
Cross-calibration coefficients table for NOAA-20 and SNPP.

VIIRS Band	NOAA20 (VNP)	SNPP (VJI)
M1	1.0213 + 0.001292×(Year-2018)	0.9562 + 0.000235×(Year-2012)
M2	1.0276 + 0.001683×(Year-2018)	0.9799 + 0.000179×(Year-2012)
M3	1.0260 + 0.001680×(Year-2018)	0.9850 + 0.000579×(Year-2012)
M4	1.0264 + 0.001605×(Year-2018)	0.9827 + 0.000125×(Year-2012)
M5	1.0201 + 0.000917×(Year-2018)	0.9806 + 0.000243×(Year-2012)
M7 (I2)[1]	1.0068 + 0.000814×(Year-2018)	0.9724 + 0.000862×(Year-2012)
M7 (M5)	1.0080 + 0.000834×(Year-2018)	0.9723 + 0.000821×(Year-2012)
M8	0.9953 + 0.002961×(Year-2018)	0.9624 + 0.001218×(Year-2012)
M10	0.9836 + 0.007938×(Year-2018)	0.9409 + 0.001306×(Year-2012)
M11	0.9832 + 0.008016×(Year-2018)	0.9358 + 0.001363×(Year-2012)
I1	1.0333 + 0.001299×(Year-2018)	0.9948 + 0.000433×(Year-2012)
I2	1.0121 + 0.000514×(Year-2018)	0.9731 + 0.000760×(Year-2012)
I3	1.0015 + 0.006207×(Year-2018)	0.9588 + 0.000586×(Year-2012)

[1] It is recommended that the M7 coefficient based on I2 be used, rather than the M7 coefficient based on M5, due to the close similarity of the M7 and I2 spectral bands.

to as the land "Golden" Tiles (GT, Fig. 8).

These GT time series plots (NASA LDOPE, 2023) are routinely monitored by LDOPE personnel to compare and confirm the continuity of observations from MODIS Aqua C61 to C2 VIIRS, employing multiple land products like, land surface reflectance, BRDF, LAI/FPAR, and VI at multiple temporal resolutions. Fig. 9 shows the GT time series plots, comparing C2 SNPP and C61 MODIS Aqua, for two of the land products, BRDF and VI, over one of such GT (h11v08) located over the Northern Amazon. The differences between SNPP and Aqua are <1% in all cases. LDOPE is currently working to integrate the values from C2 NOAA-20 land products for ease of comparison across all three platforms.

4. Continuity of data products

This section provides an introduction of relevant VIIRS products, a description of the algorithm for continuity data products, and evidence of continuity between MODIS and VIIRS products. Quantitative comparisons between products are provided, along with the status and maturity of the product(s) and algorithm(s) as guidance to users. Some sections include the potential impact of the drifting Terra/Aqua MODIS drifting orbits on this product.

To aid the reader in understanding the scope for each section, the relevant MODIS and VIIRS products for the section are named at the start of the section. In the statements of relevant MODIS and VIIRS products, lower-case x is used as a wildcard to indicate that the product name is a generalization of child products. For example, Vxx15A2H indicates the section is relevant to both the VNP15A2H product and the VJ115A2H product. Where product names are followed by a combination of an upper-case C and an accompanying number this indicates that the section is relevant to a particular product version (also known as a collection) of the product or products. For example, C61 refers to Collection 6.1.

4.1. Downward Shortwave Radiation (DSR) and Photosynthetically Active Radiation (PAR)

Primary author: Dongdong Wang. The relevant MODIS products are MCD18xx. The relevant VIIRS products are VNP18xx.

4.1.1. MODIS products for DSR and PAR

Surface downward shortwave radiation (DSR) is a key parameter of the surface radiation equation, largely determining surface radiation and energy balance. As a result, DSR data is needed to study many ecological, hydrological, climatic, and environmental problems. The spatial and temporal variability of DSR is currently receiving increased attention due to its importance for the management and operation of

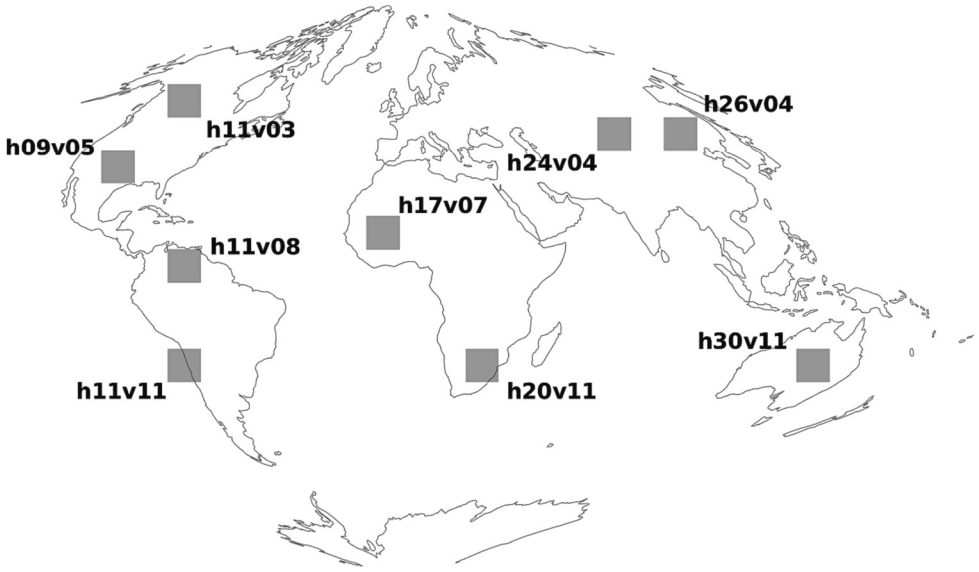

Fig. 8. Location of MODIS Golden Tiles across different biome types (NASA LDOPE).

solar energy systems. Particularly, photosynthetically active radiation (PAR), the visible component of DSR with the spectral range between 400 nm and 700 nm, is the energy used in photosynthesis and of great importance for modeling vegetation productivity and predicting crop yields. The MCD18 product suite is a relatively new member of the NASA MODIS land product family, providing the global diffuse and direct DSR and PAR data over the land surface at a spatial resolution of 1 km from a combination of Terra and Aqua MODIS observations. The MCD18 products are also available at an aggregated 0.05° resolution of the Climate Modeling Grid.

4.1.2. VIIRS products for DSR and PAR

Starting from Collection 2, DSR and PAR will be included as part of the operational NASA VIIRS land product suites. NASA VIIRS DSR and PAR products share a similar data structure as its MODIS counterparts. In addition to the instantaneous and 3 h datasets (which follow the MODIS data structure), VIIRS DSR and PAR products also include daily mean values. The current VIIRS DSR and PAR product uses VIIRS observations from a single spacecraft, such as SNPP or NOAA-20.

4.1.3. Algorithm for data product continuity

NASA VIIRS DSR and PAR products use the same physics-based retrieval algorithm as the MCD18 products. Look-up tables (LUTs) for surface and top of atmosphere (TOA) spectral reflectance were generated from offline simulations of atmospheric radiative transfer. TOA reflectance values are used as the main inputs in the DSR retrieval algorithm to avoid the use of high-level atmospheric parameter products, which are typically available at coarser spatial resolutions and contain numerous missing values. Estimation of DSR then proceeds in two major steps. First, an atmospheric visibility index is estimated based on the interpolation of the TOA LUT. Second, the DSR and PAR is calculated from the surface LUT using the atmospheric information retrieved from the first step.

4.1.4. Evidence of continuity between MODIS and VIIRS DSR and PAR

Since the MODIS and VIIRS DSR/PAR products follow the same physical retrieval strategy, the consistent calibration between the two sensors also provides the foundation to produce a uniform, long-term data record across MODIS and VIIRS sensors. A comparison of the MODIS and VIIRS DSR/PAR products for a single day (Jan. 1, 2021) showed little systematic bias between the two datasets, with a bias of only 1 W/m^2 (Fig. 10). However, a root mean square error (RMSE) of 18.9 W/m^2 was observed, mainly because the number and timing of the observations from the two sensors do not align with each other. In addition, the differences in view geometry at the pixel level between the two sensors also causes different scattering artifacts due to the parallax effect of observing clouds from space.

4.1.5. Validation of quality of continuity product

Validation for DSR is not available, since the VIIRS DSR product is not released yet. The MCD18 product has been extensively evaluated using in-situ data measured at ground stations around the world (the Baseline Surface Radiation Network; Ohmura et al., 1998). The daily DSR has a RMSE of 32.3 W/m^2, and PAR has a RMSE of 13.1 W/m^2 (Wang et al., 2020). The accuracy of DSR and PAR is dependent on the number of observations per day, especially in areas where atmospheric conditions display strong diurnal variability. The incorporation of additional observations, such as those from multiple VIIRS sensors, is expected to further improve the accuracy of estimating DSR and PAR.

4.1.6. Status and maturity of DSR and PAR products and algorithms

The LUT method is a highly mature and reliable inversion approach to estimate DSR from satellite TOA observational data (Wang et al., 2021a). After algorithm refinement, the latest version of MCD18 (C62) demonstrated improved accuracy over the previous version. Continuous efforts have been dedicated to further enhancing the performance of DSR and PAR retrieval algorithms. A transfer-learning based algorithm was recently developed to harness the capabilities of physical modeling in data-driven estimation of DSR (Li et al., 2022a). In another study, deep learning was applied in DSR retrieval, which was able to utilize spatial and temporal information in addition to the spectral domain of satellite observations (Li et al., 2023a).

4.1.7. Potential impacts of Terra/Aqua MODIS drifting orbits on DSR and PAR

The MODIS DSR retrieval algorithm is not dependent on specific observation times, as the algorithm is able to explicitly account for the varying observation time and view geometry. As a result, the orbital drifts of Terra and Aqua satellites should have minimal impacts on the process of DSR retrievals. Nevertheless, changes in the satellite overpass time will alter the pattern of diurnal sampling of atmospheric dynamics, which may lead to differences in retrieval uncertainties due to a sampling shift toward greater solar zenith angles.

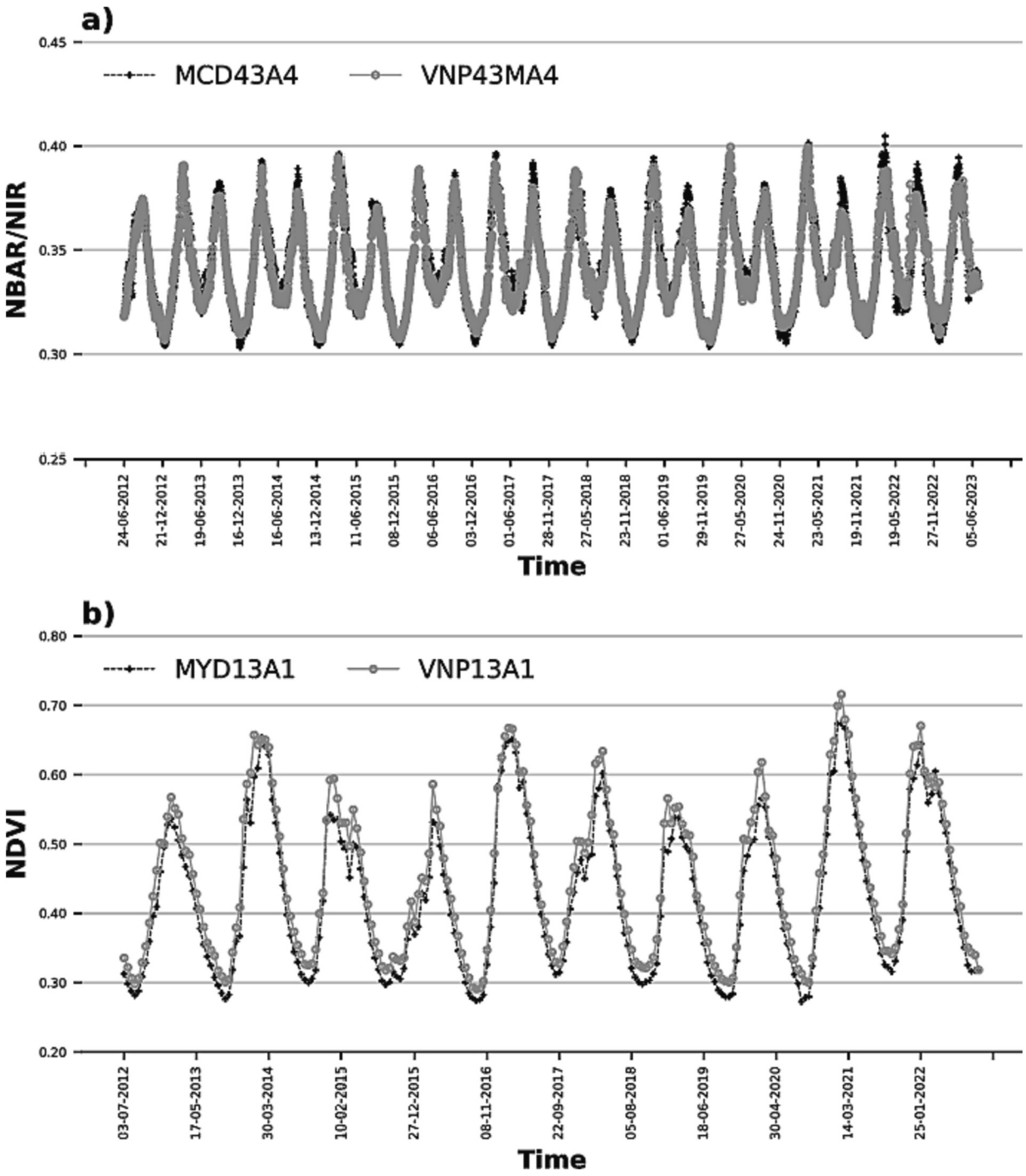

Fig. 9. Golden-Tile time-series plots of MODIS and VIIRS: a) Nadir BRDF-Adjusted Reflectance (NBAR) Near-Infrared channel for biome type "Broadleaf forest" in tile h11v08, and b) Normalized Difference Vegetation Index (NDVI) for biome type "Savannas" in tile h20v11.

4.2. Land Surface Temperature and Emissivity (LST&E)

Primary author: Glynn Hulley. The relevant MODIS products are MxD11 and MxD21. The relevant VIIRS products are Vxx21.

4.2.1. MODIS LST&E products

Land Surface Temperature and Emissivity (LST&E) are two fundamental products derived from the MODIS thermal infrared (TIR) bands. LST&E are defined as an Essential Climate Variable (ECV) by the Global Climate Observing System (GCOS) and are widely used by a broad scientific community for a variety of studies on topics such as drought monitoring, water resource management practices, climate trends, and in urban heat islands. LST&E products from MODIS have been produced operationally by NASA on daily timescales since 2000 for the Terra platform (morning), and since 2002 for the Aqua platform (afternoon) at 1 km spatial resolution at nadir with accuracies at the 1 K level. Currently 2 different LST&E products are produced by MODIS – LST from a split-window algorithm (MxD11) and LST&E from the Temperature Emissivity Separation (TES) algorithm (MxD21).

4.2.2. VIIRS LST&E products

Similar to MODIS, LST&E are produced routinely from the TIR bands

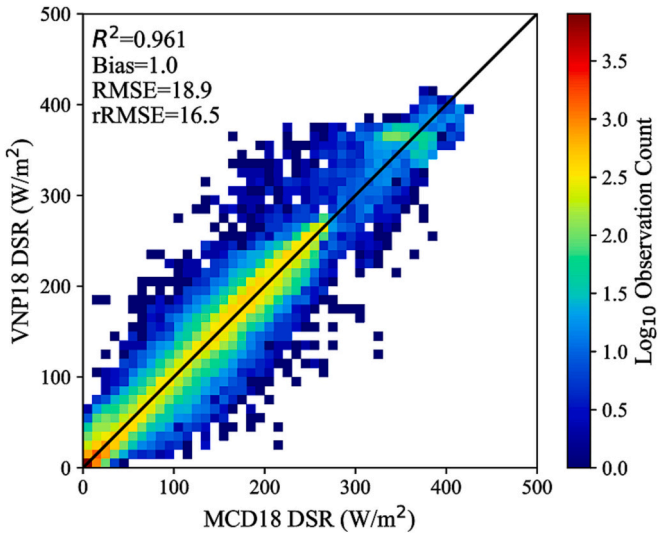

Fig. 10. Comparison of daily mean DSR between MCD18 with VNP18 for Jan. 1, 2021.

(M-bands) of the VIIRS instrument on the Suomi-NPP (SNPP) and the NOAA-20 platforms. The VIIRS LST&E products are produced from afternoon observations (similar to Aqua) at a 750 m spatial resolution using an identical TES algorithm to that of MODIS (MxD21). In addition to the 750 m M-bands used for the standard products, the VIIRS sensor also includes five higher-resolution bands (I-bands). One of these bands (I5) is sensitive to radiation in the longwave TIR spectral region between 10.5 and 12.4 μm, allowing for accurate surface temperature estimation. This VIIRS I5 band is used to produce a 375 m LST product in near-real-time (NRT) with the goal of providing information for NRT monitoring of plant water stress and irrigation decision-making in water-limited regions.

4.2.3. *Algorithm for data product continuity*

The MODIS and VIIRS LST&E continuity products use a physics-based algorithm termed the TES algorithm to retrieve both the LST and spectral emissivity simultaneously from the three MODIS TIR bands (29, 31, 32, and) and three VIIRS TIR bands (M14, M15, and M16) (Hulley et al., 2017; Islam et al., 2017; Malakar and Hulley, 2016). The algorithm was initially developed for the five bands of ASTER (on Terra) (Gillespie et al., 1998). The algorithm uses full radiative transfer simulations for the atmospheric correction and an emissivity model based on the variability in the surface radiance data to dynamically retrieve both LST and spectral emissivity. The TES algorithm is combined with a new Water Vapor Scaling (WVS) atmospheric correction scheme to stabilize the retrieval during very warm and humid conditions (Malakar and Hulley, 2016; Tonooka, 2005). Simulations and validation results have demonstrated consistent accuracies at the 1 K level over all land surface types including vegetation, water, and desert regions (Hulley et al., 2012a, 2012b).

4.2.4. *Evidence of continuity between MODIS and VIIRS LST&E products*

A long, stable record of LST is critical for monitoring climate trends, reducing systematic biases in land surface models, and for filling gaps where few in situ measurements of surface air temperatures exist (e.g., over Africa). Significant efforts have been made to ensure continuity in the LST&E data record between MODIS-Aqua and VIIRS-SNPP (Hulley et al., 2017). The VIIRS LST&E products in Collection 2 are produced using an identical algorithm as the MODIS counterpart products (MxD21) in Collection 6.1 using the TES algorithm (Hulley et al., 2012a). The MxD21/VNP21 LST&E continuity products address discrepancies in accuracy and consistency between the heritage MODIS LST product (MxD11) and the VIIRS LST split-window product developed by NOAA, where average scene biases of 3 K and pixel differences of up to 15 K have been observed under humid and warm conditions, as shown in Fig. 11 (Guillevic et al., 2014; Hulley et al., 2017). These differences were largely attributed to differences in split-window formulation and in treatment of the surface emissivity correction. Continuity between the new MYD21 and VNP21 LST products was demonstrated to within ±0.5 K using Simultaneous Nadir Overpass (SNO) matchups over the USA, and the differences were invariant to environmental conditions and land cover type (Fig. 12). Furthermore, MYD21- and VNP21-retrieved emissivity values matched closely to within 1–2%, showing the ability to detect subtle phenological changes over a grassland in Texas (Fig. 13).

Continuity between the LST&E time-series of MODIS and VIIRS products (MYD21 to VNP21 to VJ121) will result in a consistent LST&E data record from NASA's EOS satellites to SNPP and the follow-on VIIRS instruments. This continuity will allow for the creation of continuous, long-term, and well-characterized time series of data such as the Earth Systems Data Records (ESDRs) of NASA MEaSUREs (Hulley et al., 2017; Hulley and Ghent, 2019). These types of datasets are critical for our understanding and monitoring of climatic changes in Earth system behavior related to surface temperature (Mildrexler et al., 2016; Schneider and Hook, 2010; Susskind et al., 2019).

4.2.5. *Validation of quality of the LST&E continuity product*

The VIIRS LST&E continuity products are validated following the CEOS Land Surface Temperature Product Validation Best Practices Protocol (Guillevic et al., 2018). Initial product accuracy was assessed by validating to Stage-1 status (VIIRS Land, 2022a) using a combination of Temperature-based and Radiance-based LST validation methods over select sites in the USA, including two JPL automated water sites (Lake Tahoe, Salton Sea), six land sites (Algodones Dunes, Kelso, Great Sands, Killpecker, Little Sahara, White Sands), and two vegetated sites (Redwood forest, Grassland). These Stage-1 sites, although regional in scope, are largely representative of major global land cover types and validation was performed both day and night and for all seasons. Stage-2 validation is ongoing over a global set of sites and over a longer time period of data acquisitions.

Results for the Stage-1 validation of VNP21 LST data over the Southwest USA sites in Fig. 14 showed stable and accurate LST retrievals to <1.5 K Root Mean Square Error (RMSE) and accuracies of <1 K. The RMSE at all ten sites was 1.08 K. Average emissivity differences between retrieved VNP21 emissivity spectra and the lab measured spectra at Algodones Dunes, CA in Fig. 12 were within 0.015 (1.5%) for all bands (Fig. 15). In general, emissivity errors <1.5% are required to achieve LST accuracies of ~1 K.

4.2.6. *Status and maturity of LST&E products and algorithms*

The TES algorithm is mature with a strong heritage dating back to ASTER, and is also currently being used for LST&E estimation from other sensors such as ECOSTRESS (Hulley et al., 2021), and is slated for us in the future Surface Biology and Geology (SBG) Thermal Infrared (TIR) instrument. The algorithm has well-defined uncertainty metrics, and this information is included on a per-pixel basis in the products. Both MODIS and VIIRS LST&E products meet the GCOS requirements for a climate quality LST record, with both accuracy and precision of ≤1 K and a stability of <0.3 K per decade. The split-window MODIS product (MxD11); will not be continued for VIIRS, and users are encouraged to use the TES products for future science studies due to their continuity from MODIS to VIIRS, stable accuracies over all land-cover types, and because they include emissivity retrieved for each of the TIR bands enabling a wider range of studies.

4.2.7. *Potential impacts of Terra/Aqua MODIS drifting orbits on LST&E*

The change in orbits will not directly affect the quality of the MODIS LST&E products since thermal infrared data are dependent on surface emission and are unaffected by changes in solar irradiance and/or sun view-angle. In fact, the MxD21 products will have a unique opportunity

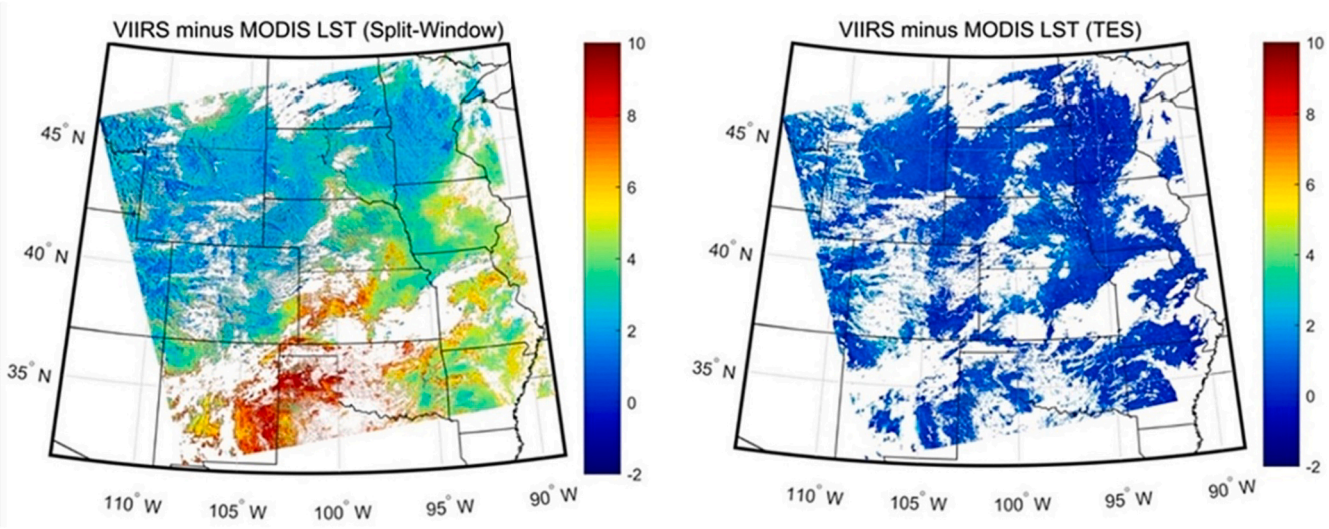

Fig. 11. LST Differences between the VIIRS and MODIS-Aqua 1:30 PM LST products using split-window algorithm formulations (left) and the TES algorithm (right) for a granule overpass at 20:40 UTC on August 11, 2012. The MODIS and VIIRS TES-derived products (MYD21, VNP21) have differences at the <0.5 K level (right) while the split-window products have differences of up to 15 K (2 K mean error; left). (For interpretation of the references to colour in this figure legend, the reader is referred to the web version of this article.)

to provide surface temperatures at a unique set of earlier morning or later afternoon hours not currently possible from other instruments. For example, the current Aqua overpass underestimates and overestimates the maximum and minimum LST, respectively. Consequently, the true maximum temperature (LSTmax) distributions at neighborhood scales are often missed, particularly in low-income communities with less green space, where temperature maximums occur later in the afternoon hours. A later Aqua observing time would result in more accurate estimates of the diurnal temperature range for urban climate studies, improve our understanding of the true distributions of LSTmax in lower-income communities, and provide better estimates of maximum air temperatures for estimating societal heat vulnerability at neighborhood scales.

4.3. Bidirectional Reflectance Distribution Function (BRDF), Nadir BRDF-Adjusted Reflectance (NBAR), and Albedo

Primary authors: Crystal Schaaf, Zhuosen Wang, Angela Erb, and Shuai Zhang. The relevant MODIS product is MCD43. The relevant VIIRS product is Vxx43.

4.3.1. Introduction

The global daily Terra and Aqua MODIS Bidirectional Reflectance Distribution Function (BRDF), Nadir BRDF-Adjusted Reflectance (NBAR), and Albedo Products (MCD43) have been produced since the start of the MODIS record in 2000. The quality and consistency of these long-term multi-decadal MODIS albedo records have encouraged their extensive use in evaluating and adjusting climate, weather, biogeochemical, and hydrological models and in monitoring land cover change and vegetation phenological cycles.

BRDF describes how a surface reflects incident radiation. The distribution of reflected radiation described by a BRDF model can be idealized either as isotropic, scattering light uniformly in all directions, or anisotropic, with scattered light varying in intensity depending on the angle/direction of reflection. A BRDF model of surface anisotropy cannot be retrieved with only a single remotely-sensed, nadir reflectance observation. However, a BRDF model of the surface anisotropy can be retrieved using high-quality, cloud-free, atmospherically-corrected, multi-angle surface reflectance observations. The surface properties described by BRDF can be used to establish vegetation clumping indices, derive measures of surface structure, and derive both Albedo and NBAR values.

Albedo is a measure of the proportion of radiative flux reflected by a surface relative to the flux of incident solar radiation upon the surface. Albedo is calculated by integrating incident and reflected energy fluxes across a set of wavelengths of light and over all angles of incidence and reflection, effectively describing the entire “hemisphere” of radiative flux for a given surface. Integrating over all possible view and illumination angles provides a fully diffuse “white-sky” albedo. Integrating over all possible view angles for a particular solar illumination angle provides a direct “black-sky” albedo of a directional hemisphere. Combining the intrinsic white-sky and black-sky albedo measures with atmospheric optical depth generates a “blue-sky” albedo, such as would be measured at the surface at a given time and for given atmospheric conditions, for use in the instantaneous modeling of land surface energy.

NBAR utilizes BRDF models to correct for view angle effects, resulting in surface reflectance values that are commonly utilized to monitor vegetation phenology, agricultural and forest productivity, snow-melt regimes, surface disturbances, and the extent and change of land cover types.

4.3.2. MODIS BRDF, NBAR, and Albedo products (C61)

The BRDFs, NBARS, and Albedos are generated for individual spectral bands (Strahler et al., 1999), including daily global MODIS 500 m gridded BRDF models, NBARs, and white-sky and black-sky Albedos (provided at a sinusoidal projection on 10 degree tiles (MCD43A*). In addition, broadband albedo values are generated using narrow-to-broadband coefficients. 30 arc-second products (MCD43D*) are provided on a global lat/long projection and are also averaged to 0.05 degree products (MCD43C*) for use by climate modelers.

Gap-filled, snow-free, 30 arc-second resolution versions of the products (MCD43GF; Sun et al., 2017) are also created from temporal fits of the BRDF parameters over 15 months and then delivered to the LPDAAC. These products are in high demand as they are used as initiation fields for various climate models (e.g., ECMWF models). Therefore, a great deal of emphasis is being placed on providing comparable and consistent versions of these products from the VIIRS Collection 2 (C2) processing in order to continue to extend the long-term record.

4.3.3. VIIRS BRDF, NBAR, and Albedo products

The VIIRS products, derived from sensors on-board the Suomi NPP (VNP43*), NOAA-20 (VJ143*), and NOAA-21 (VJ243*) platforms, will

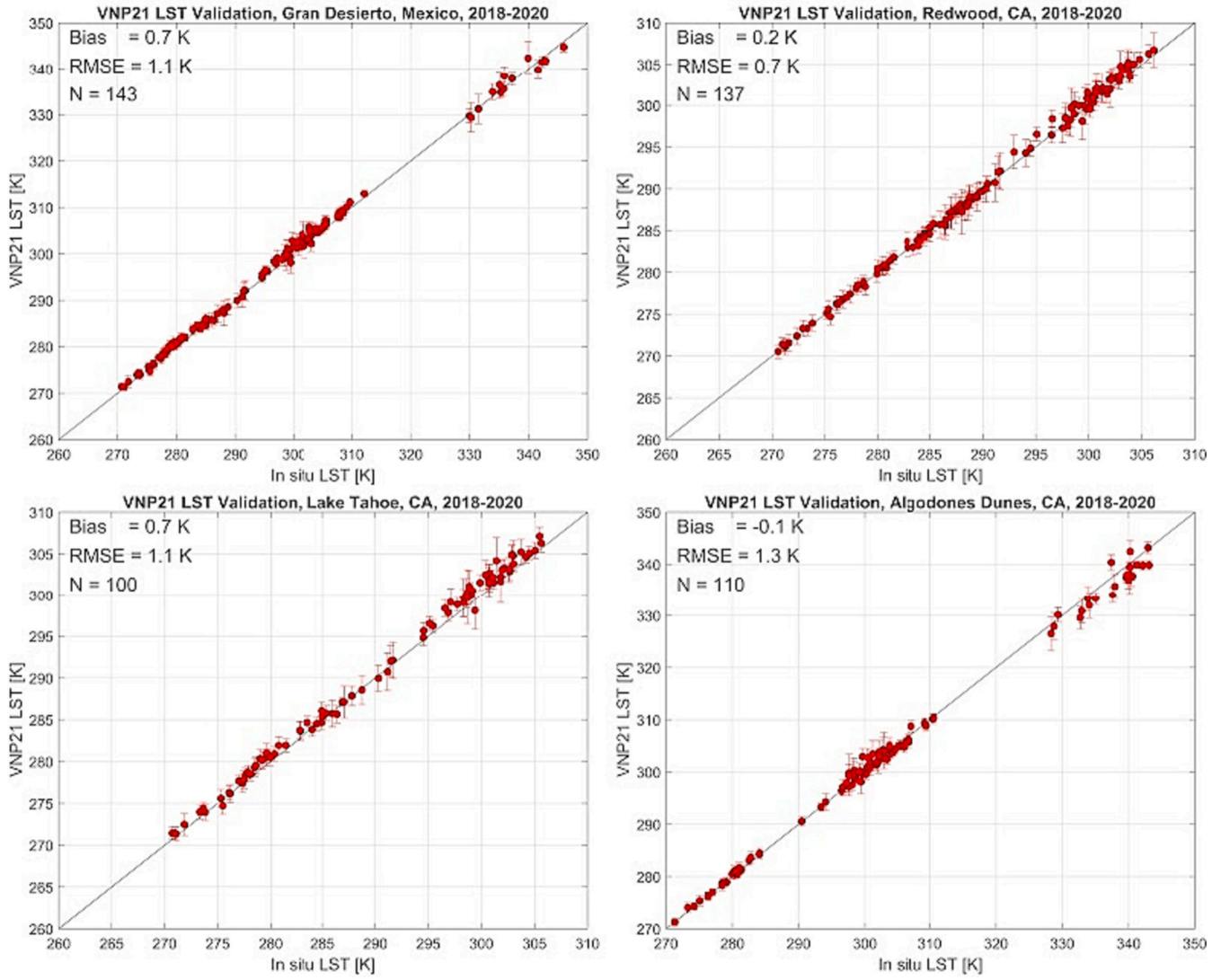

Fig. 12. Boxplots of VIIRS minus MODIS LST for the TES algorithm products (MYD21, VNP21) show differences that are invariant with land cover type. LST differences were grouped according to standard International Geosphere-Biosphere Programme (IGBP) classification data from MCD12 product.

provide continuity for the MODIS BRDF, NBAR, and Albedo products. The VIIRS C2 products (VNP43* and VJ143*) provide 500 m spectral products for the VIIRS Imagery bands (bands I1–3) and 1 km spectral and broadband values for the VIIRS Medium bands (bands M1–5, M7–8, and M10–11).

4.3.4. *Evidence of continuity between MODIS and VIIRS BRDF, NBAR, and Albedo products*

For tiles of data from three distinct environments, the Southwest US, Amazonia, and the Northeast US, differences between VIIRS and MODIS shortwave, white-sky albedo products were between 0.01 and 0.02 (RMSE) on average (Fig. 16). Mean bias within these tiles ranged from 0.002 to 0.02, a comparable range to those observed in heritage MODIS products (Liu et al., 2017a). In addition, within these two tiles (Fig. 16), the RMSE values from MODIS-VIIRS comparisons (MCD43A3 vs. VNP43MA3 and VJI43MA3) were of similar magnitude to RMSE estimates between VIIRS instruments (VNP43MA3 vs. VJI43MA3). These similarities are indicative of the high quality and stability of VIIRS products for ensuring continuity of the MODIS Albedo products.

A time-series of blue-sky albedo values from MODIS, VIIRS, and tower albedometer data demonstrated the high agreement between MODIS and VIIRS data products over the course of a year at a temperate mixed forest site in the Northeastern US (Fig. 17). However, discrepancies can be observed between data products, especially during winter months when there is a high probability of snow cover. This site is considered homogeneous during the peak growing season and heterogeneous during the winter and shoulder seasons.

The small offsets between the MODIS, VIIRS, and tower time-series data (Fig. 17) can also be attributed to differences in the spatial resolutions and field of views of the instruments. Certain VIIRS products have a much larger effective field of view of the surface than do the MODIS products and the tower instruments (see 2.12.3). Therefore, the coarser spatial resolutions of the VIIRS products do result in a small discrepancy in the modeled surface values of MODIS and VIIRS albedo products for several equivalent bands (see Table 2). However, this discrepancy is not expected to pose significant issues for data continuity.

4.3.5. *Status and maturity of BRDF, NBAR, and albedo products and algorithms*

The current MODIS (C61) and VIIRS (C2) products are generated by the Level-1 and Atmosphere Archive & Distribution System (LAADS) Distributed Active Archive Center (DAAC) at the Goddard Space Flight Center. These data are distributed to the public through the Land Products Distribution System Distributed Active Archive Center

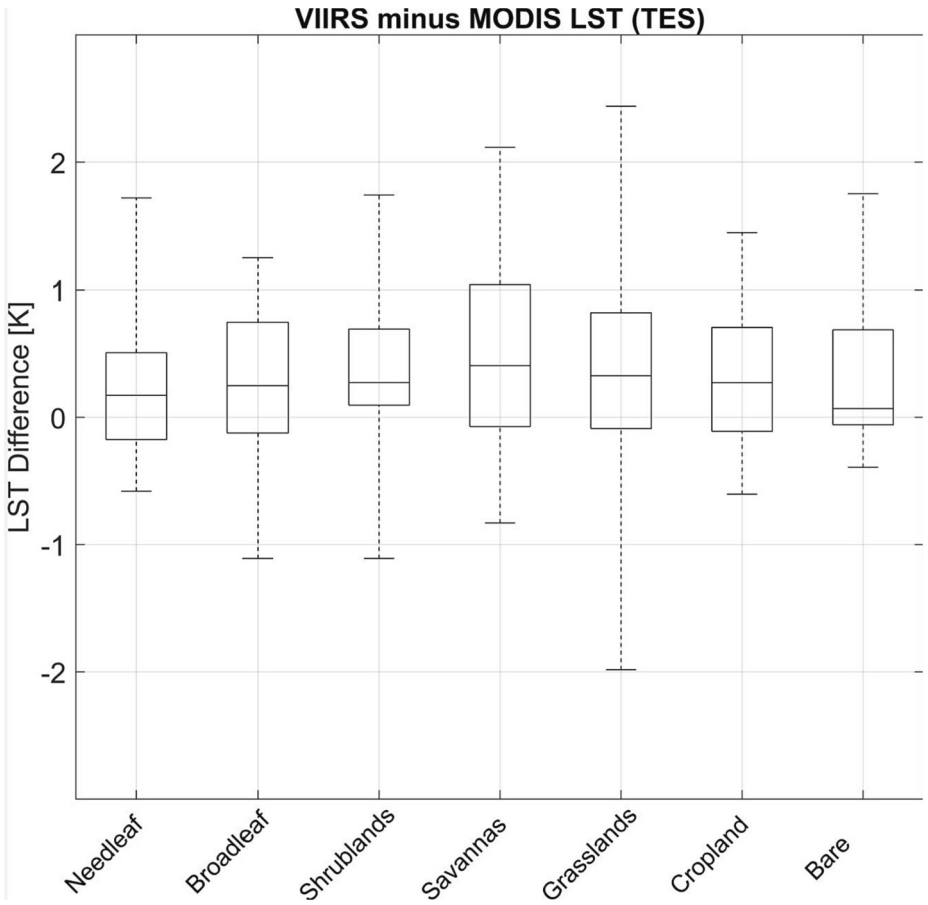

Fig. 13. Emissivity time series for MODIS band 29 and VIIRS band M15 emissivity (8.55 μm) show close agreement in magnitude and temporal variation for detecting fine scale phenological change between 2013 and 2015 over a grassland in Texas.

(LPDAAC) at the USGS Eros Data Center (EDC), Sioux Falls, South Dakota. Extensive quality information is provided with each of the products.

Near-real-time versions of these products have also been developed (primarily for agricultural and rangeland monitoring) and disseminated through the LANCE (Land, Atmosphere, Near real-time Capability for EOS) system. The MODIS Albedo product suite has been validated to CEOS Stage 4 (NASA CEOS, 2023). The VIIRS Albedo product suite has been validated to CEOS Stage 2.

4.3.6. Potential impacts of Terra/Aqua MODIS drifting orbits on BRDF, NBAR, and albedo

Because BRDF, NBAR, and Albedo focus on the angle-dependent properties of surfaces, rather than scale-dependent properties, the drifting orbits of Terra and Aqua are not expected to impact the viability or applications of the products.

4.4. Multi-Angle Implementation of Atmospheric Correction (MAIAC)

Primary author: Alexei Lyapustin. The relevant MODIS product is MCD19A1. The relevant VIIRS product is VCD19A1.

4.4.1. MODIS MAIAC products

The Multi-Angle Implementation of Atmospheric Correction (MAIAC) is an interdisciplinary algorithm performing joint MODIS Terra and Aqua processing and providing cloud/cloud shadow (Lyapustin et al., 2012) and snow detection, aerosol optical depth (AOD), smoke plume injection height (Lyapustin et al., 2019), and column water vapor (CWV) (Lyapustin et al., 2014a) retrieval at high 1 km resolution along with land spectral surface reflectance in bands 1–12 and BRDF in bands 1–8 (Lyapustin et al., 2018; Lyapustin et al., 2021a). Over coastal ocean and inland waters, MAIAC retrieves AOD, fine mode fraction, and water leaving reflectance. A 1 km resolution snow fraction and snow grain size (SF/SGS) are reported when snow is detected. Due to its high accuracy and resolution, MAIAC AOD and CWV are widely used for the global monitoring and prediction of the particulate matter, a component of the Air Quality assessment (e.g., Kloog et al., 2014; Hammer et al., 2020, 2021; Van Donkelaar et al., 2021; Wei et al., 2021). Both MAIAC AOD and BRDF have been used in analysis of climate and aerosol forecast models (Makkaroon et al., 2023).

MAIAC MODIS Collection 6 record was released in 2018. The new MAIAC Collection 6.1 (C61) dataset became available in June of 2023. It contains three daily files with surface reflectance (water-leaving reflectance over ocean) at 500 m and 1 km (MCD19A1), atmospheric AOD, CWV, fine mode fraction (over ocean), and plume height at 1 km (MCD19A2), as well as BRDF, NDVI and snow properties at 1 km (MCD19A3). In C61, BRDF, NDVI, and SF/SGS are reported as naturally gap-filled at 1 km resolution on a global Sinusoidal grid. MAIAC C61 also expanded atmospheric correction by including the gap-filled 250 m NBAR in addition to the 500 m and 1 km surface reflectance (SR) products available in MAIAC C6.

4.4.2. VIIRS MAIAC products

The MAIAC C61 algorithm has been adapted for use with VIIRS. Except column water vapor, it produces the same suite of products as for MODIS but at higher spatial resolution: 750 m for the atmospheric and gap-filled land products and 750 m and 375 m for SR products from the radiometric and imaging bands, respectively. As a further improvement, MAIAC VIIRS features a zonal sinusoidal projection (ZSP), which is a standard SP rotated 4 times by 90°. ZSP was introduced to represent the

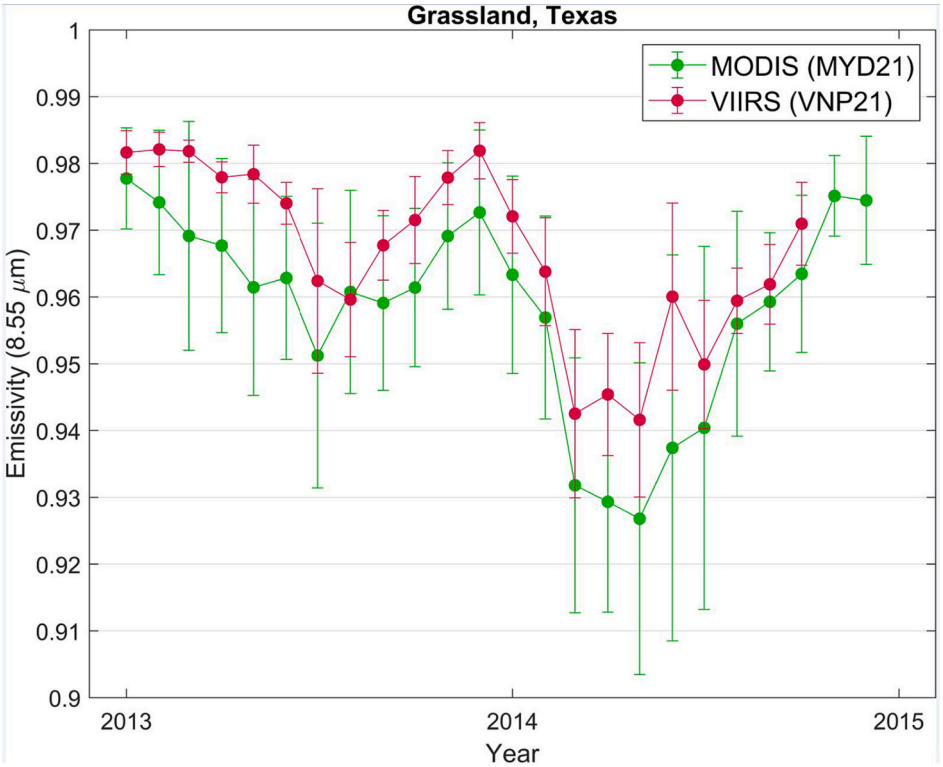

Fig. 14. LST validation scatterplots of the VNP21 LST product using a combination of Temperature-based (Lake Tahoe, CA), and Radiance-based (Algodones Dunes, Redwood, Gran Desierto) validation methods. The average LST RMSE at all ten sites was 1.08 K for two years of data (2018, 2019).

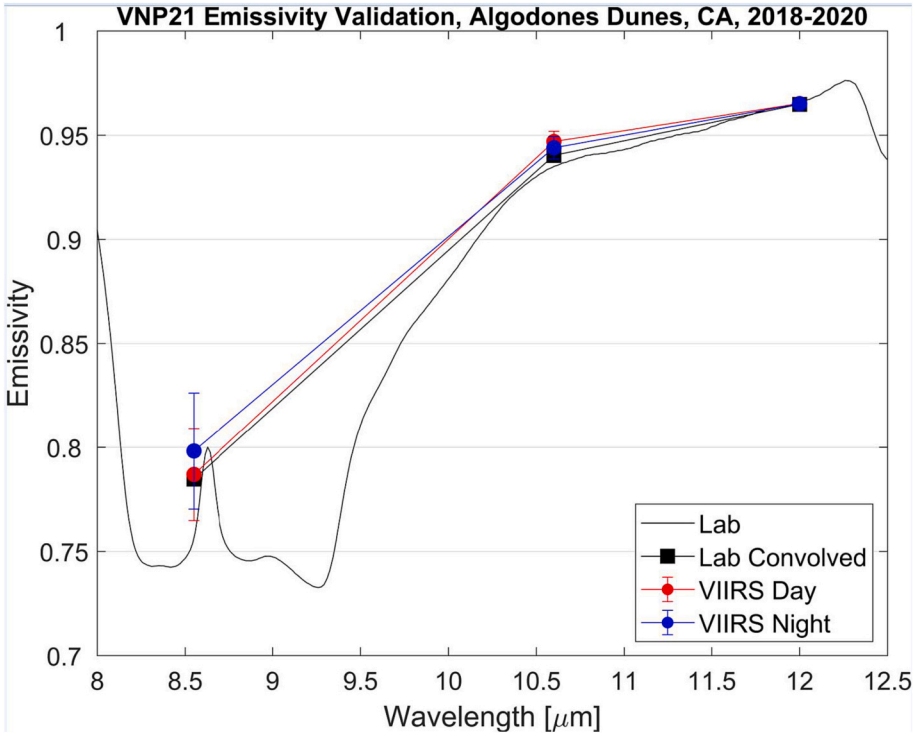

Fig. 15. Emissivity validation of the VNP21 product at Algodones Dunes, CA, and comparisons with the standard ASTER product at 4 sand dune sites in the Southwest USA. VNP21 retrieved emissivity matched closely (within 1.5%) with lab measured samples at Algodones Dunes, while matches with ASTER were within 1% for all bands. (For interpretation of the references to colour in this figure legend, the reader is referred to the web version of this article.)

globe with minimum spatial distortions (see Lyapustin et al., 2021b). Similar to MODIS, MAIAC processes VIIRS SNPP alone for the 2012–2018 time period. For the overlap periods, VIIRS SNPP and NOAA-20 (NOAA-21) are processed jointly to increase temporal coverage and retrieval accuracy. MAIAC VIIRS is available in Collection 2, for which reprocessing began in summer 2023.

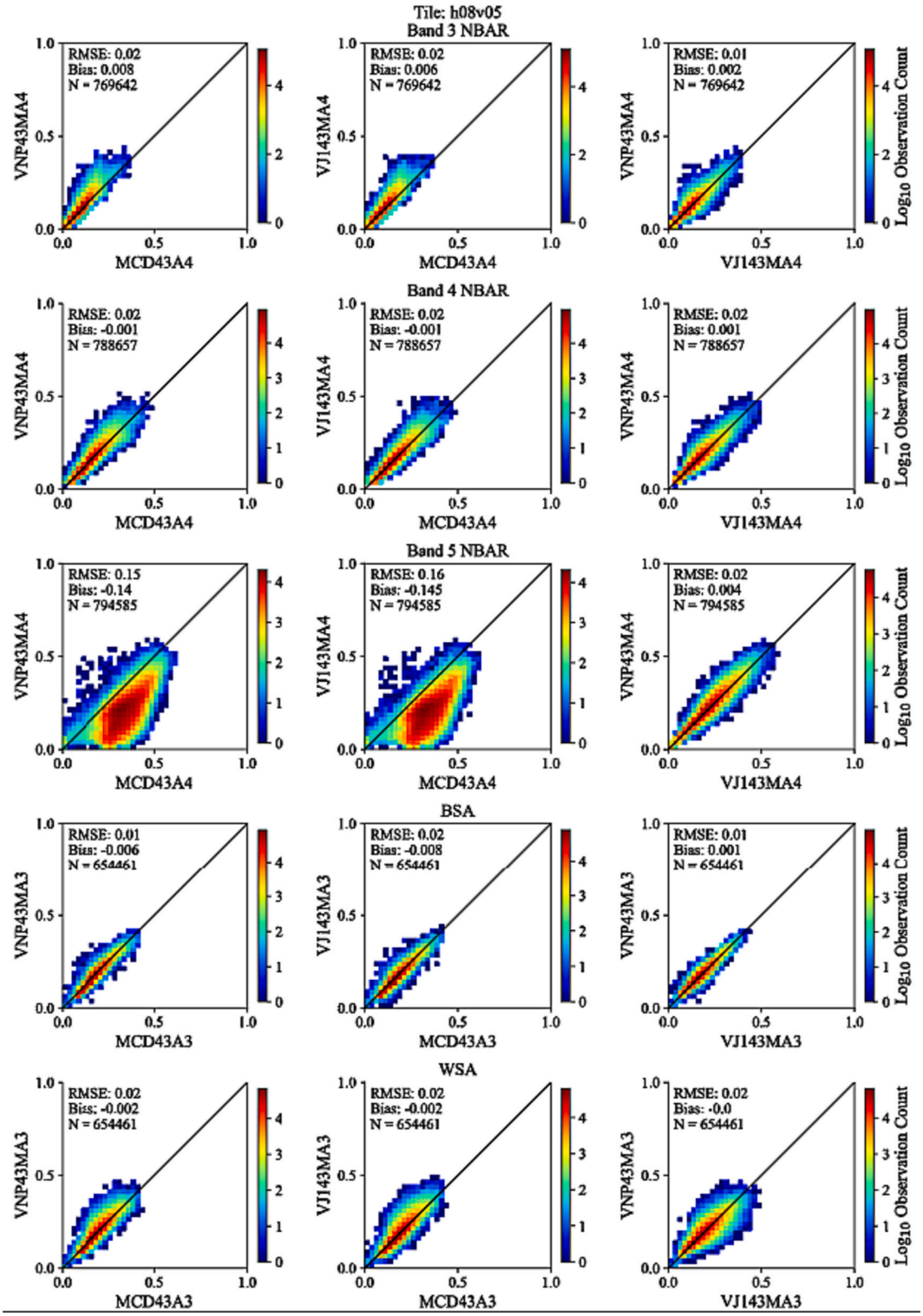

Fig. 16. Comparisons between the MODIS MCD43 (V6.1) and VIIRS VNP43 (C2) White-Sky Albedos, between the MCD43 and VJ143 values, and between the VJ143 and VNP43 values. Top: Southwestern US tile h08v05 for 2019, Bottom: Amazonia tile h11v09.

4.4.3. Algorithm for data product continuity

We conducted a calibration analysis of the SNPP and NOAA-20 VIIRS instruments over the Libya-4 CEOS desert calibration site (Lyapustin et al., 2023). The analysis included removal of the long-term calibration trends and cross-calibration of both SNPP and J1 VIIRS to MODIS Aqua, which is considered to be a calibration standard for the EOS-initiated climate data records. The MAIAC-based calibration method, originally developed to remove trends and cross-calibrate MODIS Terra to Aqua (Lyapustin et al., 2014b), has been an integral part of the MODIS land discipline C6 and C61 processing. To account for differences between

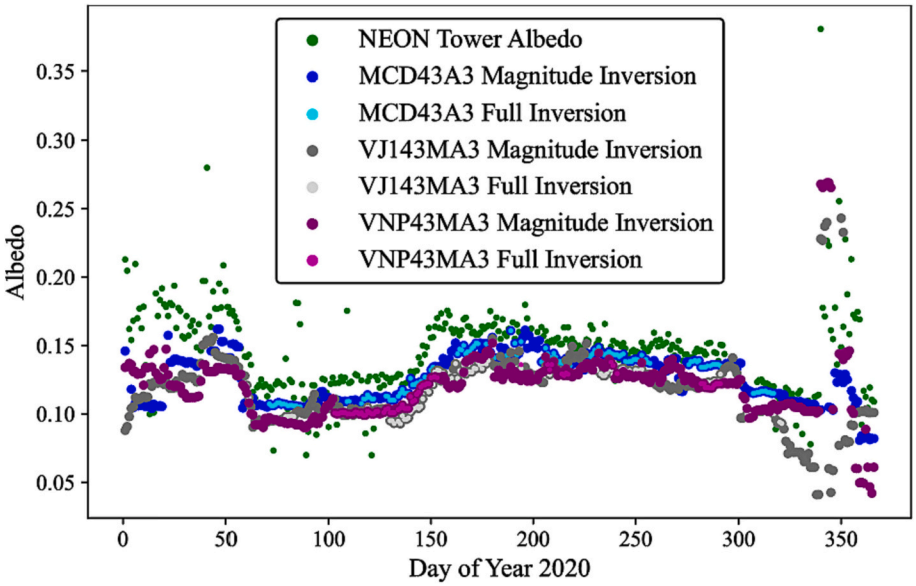

Fig. 17. Comparison between blue-sky albedo products at the location of the National Ecological Observatory Network (NEON) Harvard Forest Tower, set in a temperate forest in the Northeastern US. "Full Inversion" refers to higher-quality data, calculated using the full inversion algorithm and 7 or more retrievals within a 16-day window around the date of interest. In contrast, "Magnitude Inversion" refers to lower-quality data that are derived using extrapolated values from recent high-quality retrievals (Liu et al., 2017a, 2017b). (For interpretation of the references to colour in this figure legend, the reader is referred to the web version of this article.)

MODIS and VIIRS relative spectral response (RSR), we further updated the MAIAC calibration method by including the hyperspectral surface reflectance from DLR Earth Sensing Imaging Spectrometer (DESIS) (Alonso et al., 2019), which has been collecting Libya-4 spectra from the international space station since 2018.

4.4.4. *Evidence of continuity between MODIS and VIIRS MAIAC products*

In the latest VIIRS SNPP and J1 calibration, the two sensors differed within approximately −5% to +3.7% from MODIS Aqua. Overall, the SNPP sensor is calibrated 2% to 6.5% higher than the J1 sensor (Lyapustin et al., 2023). Table 4 gives the cross-calibration coefficients for MODIS Aqua to VIIRS SNPP and MODIS Aqua to J1 for matching bands, as well SNPP to J1 for all VIIRS bands. The slope and offset coefficients for the long-term trends can be found in Lyapustin et al. (2023).

MAIAC-based results were found to be within ~1%, which was in general agreement with dedicated analyses from the MODIS/VIIRS Characterization Support Team at NASA GSFC and the CERES-IGCG (Imager and Geostationary Calibration Group) at NASA Langley Research Center. These results ensure the reliability of the VIIRS calibration for science processing. Fig. 18 shows a close agreement of MAIAC AOD between MODIS Aqua and the two VIIRS sensors, within 0.01 and with a root mean square difference (RMSD) of ~0.04 after applying calibration. These data represent all observations for MODIS tiles H11V05 and H16V05 over western and eastern USA during the 2018–2021 period. MODIS and VIIRS data were matched spatially and temporally by aggregating data to 4 × 4 km^2 pixels with 100% coverage and comparing observations within 30 min of each other.

A comparison of MAIAC surface reflectance from VIIRS NOAA-20 to that from MODIS Aqua is shown in Fig. 19. As VIIRS SNPP and MODIS Aqua values were very similar, the comparison results are not shown here. To remove effects of variable sun-view geometry, the data were normalized to nadir view and local SZA at 1:30 pm using the MAIAC BRDF. The resulting spectral nadir BRDF-adjusted reflectance (NBAR) values agree within an RMSD of 0.003–0.005 in the visible and 0.01–0.012 at longer wavelengths. The residual differences in the magnitude of SR are well explained by the RSR differences between VIIRS and MODIS (Lyapustin et al., 2023). Finally, the differences in NDVI were also characterized, which showed a RMSD of ~0.02 and mean differences (MD) of <0.003 for $NDVI_I$ based on VIIRS imagery (I) bands and 0.01 for $NDVI_M$ based on VIIRS radiometric (M) bands (Fig. 20).

Table 4
Pair-wise cross-calibration coefficients among VIIRS on SNPP and NOAA-20, and MODIS Aqua. A reference MODIS band is indicated as B, and radiometric and imagery VIIRS bands are given by M and I, respectively.

	Cross-calibration Coefficients		
Band	Aqua/SNPP	Aqua/N20	SNPP/N20
B8/M1	0.9738 ± 0.033	1.0277 ± 0.034	1.0554 ± 0.028
B3/M2	0.9516 ± 0.031	1.0137 ± 0.026	1.0653 ± 0.034
B3/M3	0.9818 ± 0.023	1.0290 ± 0.021	1.0481 ± 0.021
B4/M4	0.9827 ± 0.018	1.0367 ± 0.018	1.0550 ± 0.018
B1/M5	0.9780 ± 0.017	1.0212 ± 0.017	1.0442 ± 0.016
B2/M7	0.9707 ± 0.017	1.0083 ± 0.017	1.0387 ± 0.017
M8	–	–	1.0264 ± 0.017
M10	–	–	1.0215 ± 0.016
M11	–	–	1.0198 ± 0.040
B1/I1	0.9917 ± 0.023	1.0316 ± 0.021	1.0402 ± 0.026
B2/I2	0.9726 ± 0.018	1.0131 ± 0.018	1.0416 ± 0.019
I3	–	–	1.0540 ± 0.018

4.4.5. *Validation of quality of MAIAC continuity products*

MAIAC MODIS AOD and CWV products have been extensively validated against AERONET (Holben et al., 1998) at local, regional, and global scales by both the MAIAC team and the broad international community (e.g., Lyapustin et al., 2018; Martins et al., 2019; Schutgens et al., 2020; Su et al., 2023). Thus, these products have achieved a stage 4 validation status. The consensus assessment of expected error (EE) is 10% for MAIAC AOD (where EE = ±0.05 ± 0.1AOD) and 12–15% for the CWV.

The snow detection has been validated over North America at stage 3 (Cooper et al., 2018) using the Global Historical Climatology Network Daily (GHCN-D) database (Menne et al., 2012). Cooper et al. (2018) showed that the MAIAC F-score, which combines errors of omission and commission, was significantly higher (F = 0.86; out of 1) in comparison to that of the standard MODIS snow product (F = 0.52).

A recent study of Lyapustin et al. (2021a, 2021b) compared MAIAC

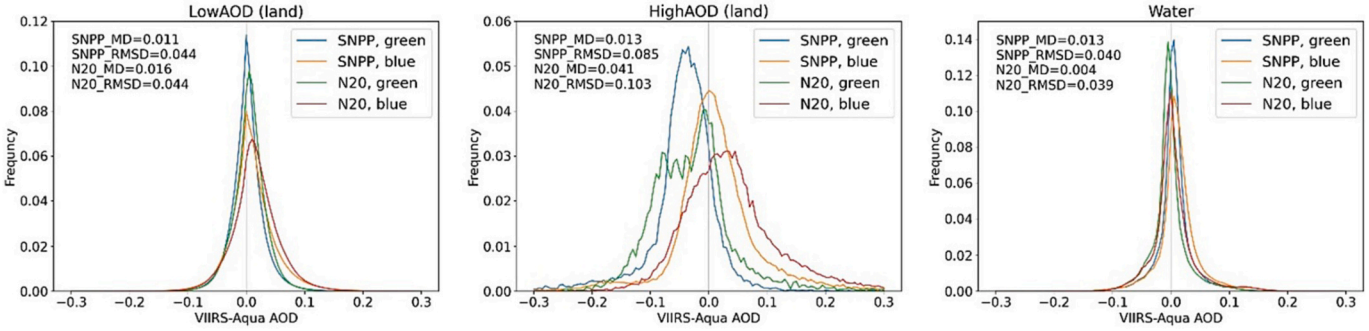

Fig. 18. AOD difference histogram (2018–2021) between VIIRS and MODIS-A over land and water. The land comparison separates cases of low $AOD_{0.55} < 0.6$ (left) and high $AOD_{0.55} > 0.6$ (center). The water case includes all AODs over the in-land water and ocean. The comparison is given for the common green (0.55 mm) and the blue band (B3 for MODIS and M2 for VIIRS). The mean difference (MD) and RMSD are provided for the Blue band (M2 for VIIRS and B3 for MODIS). Reproduced from Lyapustin et al. (2023). (For interpretation of the references to colour in this figure legend, the reader is referred to the web version of this article.)

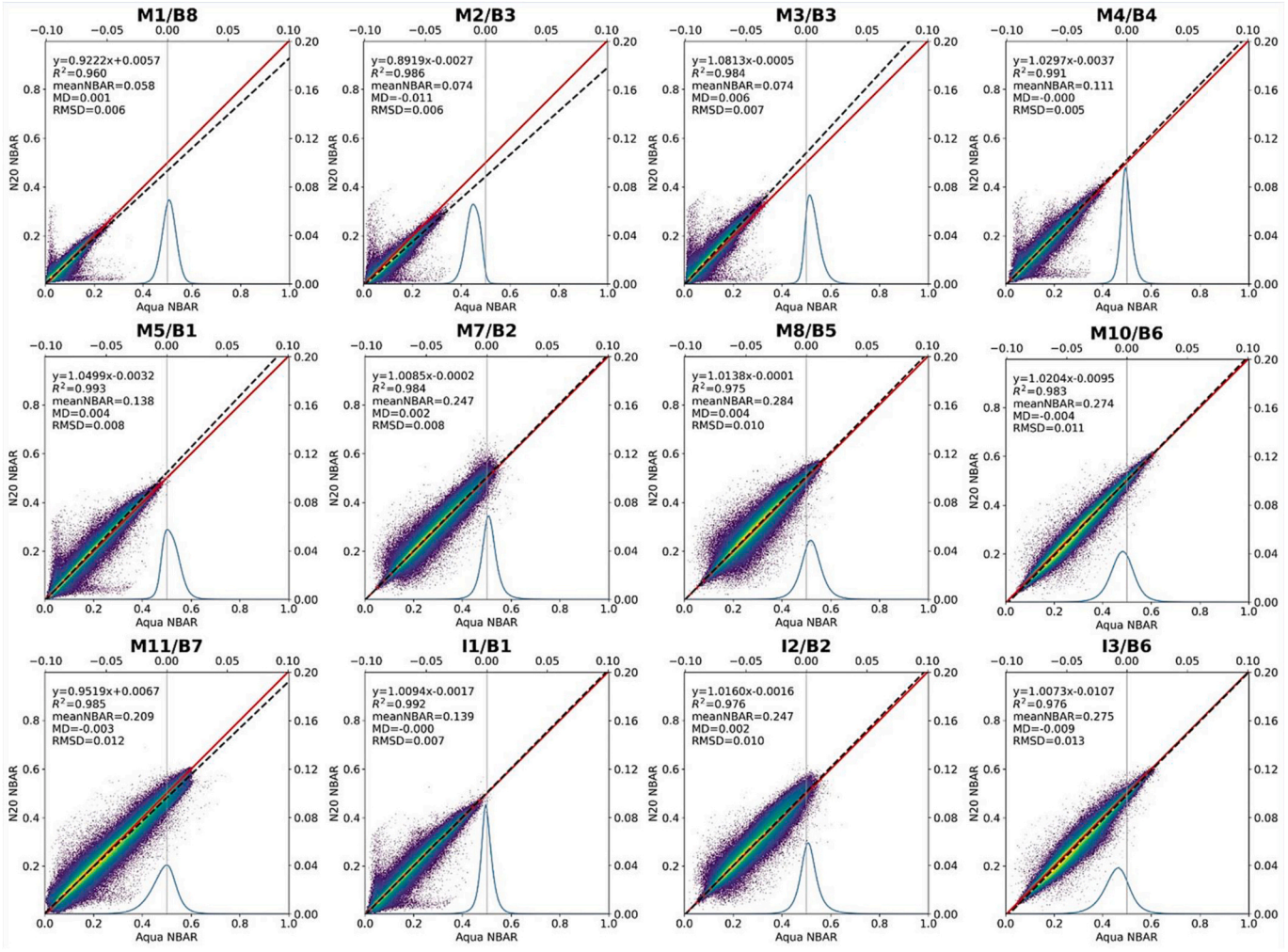

Fig. 19. A comparison of spectral NBARs between NOAA-20 VIIRS and MODIS Aqua. Reproduced from Lyapustin et al. (2023). (For interpretation of the references to colour in this figure legend, the reader is referred to the web version of this article.)

MCD19A1 and MOD09 surface reflectance. The study was based on four 1200 × 1200 km^2 tiles located in the mid-Atlantic United States (H11V05), Canada (H12V03), the central Amazon (H11V09), and North-Eastern China (H27V05). The analysis used over 5000 MODIS granules in 2018, which were representative of 15 of 17 IGBP land cover types (with the exception of semi-arid and desert regions), and thus it achieved Stage 3 validation status. Compared to MOD09, MAIAC SR showed 4% to 25% more high quality retrievals due to improved cloud detection, as well as reduced aerosol impacts due to high quality aerosol retrievals. The difference between MAIAC and MOD09 SR products is especially apparent at shortwave green-blue wavelengths, due to MOD09 relying on Lambertian surface models for correction, while MAIAC uses rigorous BRDF-based atmospheric correction. Additional comparisons of MAIAC MODIS-VIIRS SR over representative regions is

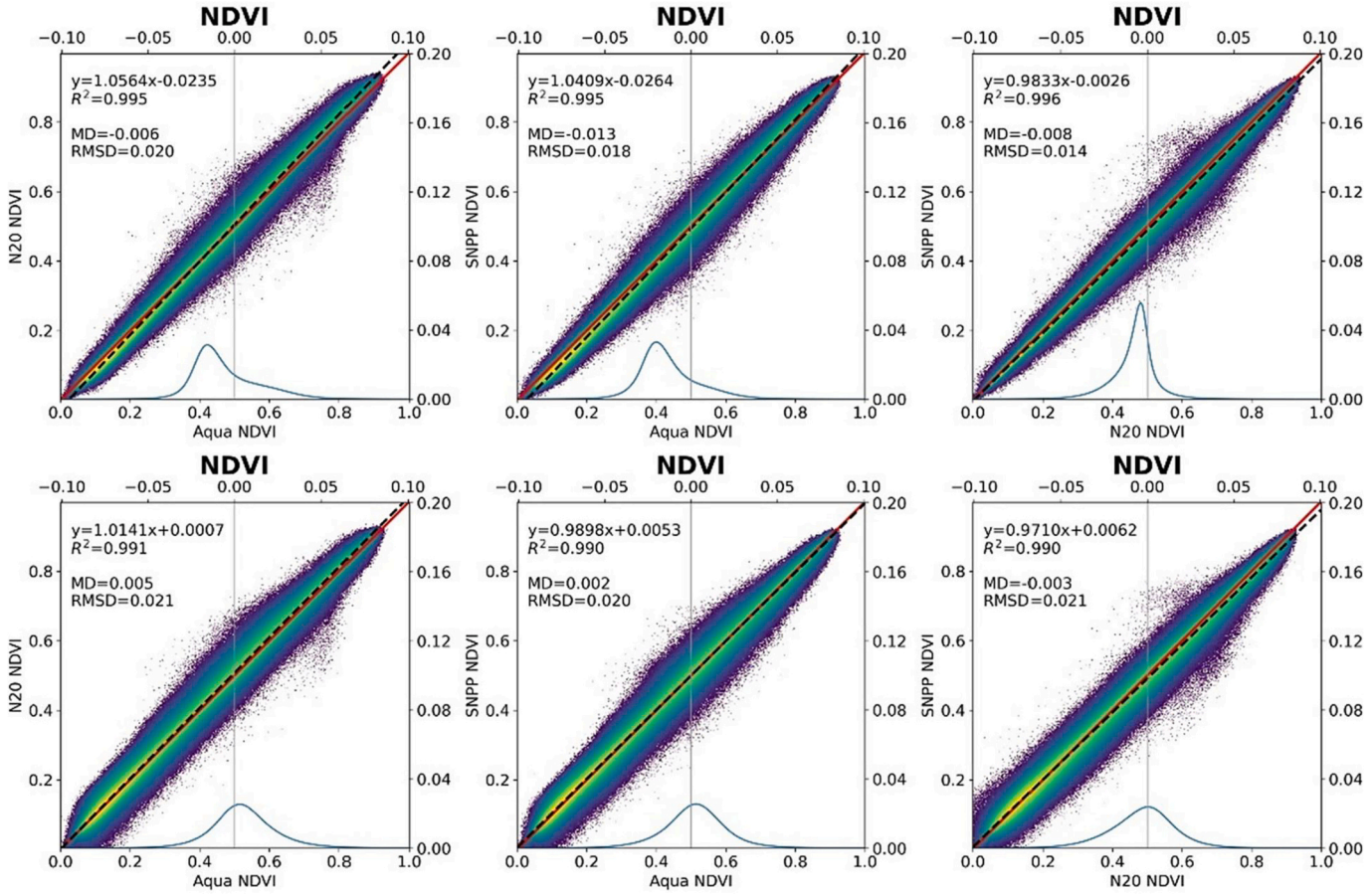

Fig. 20. A comparison of NDVI among VIIRS SNPP, VIIRS NOAA-20 and MODIS Aqua based on radiometric VIIRS bands M5/M7 (top) and imagery bands I1/I2 (bottom). The histograms show distributions of NDVI differences ($NDVI_{Y\text{-}axis}$ – $NDVI_{X\text{-}axis}$) with the scales of the axes shown at the top and right of each plot. Reproduced from Lyapustin et al. (2023). (For interpretation of the references to colour in this figure legend, the reader is referred to the web version of this article.)

planned.

4.4.6. Status and maturity of MAIAC products and algorithms

With a developed calibration procedure, we achieve full consistency of MAIAC MODIS-VIIRS aerosol and snow products. The surface reflectance and BRDF agree within characterized uncertainties for the matching bands. At the other bands, surface reflectance values and vegetation indices are not fully compatible due to RSR differences. However, MAIAC MODIS-VIIRS SR agree in the sense of hyperspectral representation of the land/ocean spectra. Due to the development of shallow cumulus clouds by early afternoon, a lack of morning observations from VIIRS results in some reduction of coverage over tropics, for instance by 20% over Amazon basin based on MAIAC data analysis (e.g., Hilker et al., 2012; Lyapustin et al., 2021a, 2021b).

4.4.7. Potential impacts of Terra/Aqua MODIS drifting orbits on MAIAC products

The MAIAC MODIS MCD19A3 BRDF product benefits from the increased range of solar zenith angles brought about by orbital drift. Similarly, the drift of MODIS Terra toward earlier morning overpasses increases the cloud-free coverage of the tropical regions, resulting in improved accuracy. In other regards, performance is not expected to change, provided that the accuracy of MODIS geolocation does not deteriorate because MAIAC works with gridded MODIS/VIIRS L1B data.

4.5. Global Land Surface Phenology (LSP)

Primary authors: Xiaoyang Zhang, Yongchang Ye, Yu Shen, Khuong H. Tran, Josh M. Gray, and Mark Friedl. The relevant MODIS product is MCD12Q2 C61. The relevant VIIRS product is VNP22Q2 C2.

4.5.1. Introduction

Land surface phenology (LSP) characterizes the timing and magnitude of seasonal greenness dynamics in vegetation communities over vegetated land surfaces. LSP has been widely recognized as an important parameter in regional and global modeling, ecological monitoring, and climate change studies (Cleland et al., 2012; Ma et al., 2019; Morisette et al., 2009; Richardson et al., 2018; Zhang et al., 2018). The global LSP product has been operationally produced from time series of MODIS and VIIRS EVI2 (2-band enhanced vegetation index) to provide a long-term LSP data record. The product quantifies six timing metrics (phenological transition dates) that are: (1) greenup onset: the date of onset of EVI2 increase; (2) maturity onset: the date of onset of EVI2 maximum; (3) senescence onset: the date of onset of EVI2 decrease; (4) dormancy onset: the date of onset of EVI2 minimum; (5) date at mid greenup phase; and (6) date at mid senescent phase. Also, the product includes five greenness metrics that include: (1) the EVI2 at onset of greenness increases; (2) the EVI2 at the onset of maximum greenness; (3) the summation of growing season EVI2 at a given time; (4) the rate of change of greenness increases; and (5) the rate of change of greenness decreases.

4.5.2. MODIS LSP product (MCD12Q2)

The MCD12Q2 C6/C61 product is generated by utilizing the algorithm described in the User Guide (Gray et al., 2019). Briefly, the algorithm first computes the background MODIS NBAR EVI2 value to

accommodate possible land cover changes and snow-contaminated observations. The EVI2 time-series is then fit using a penalized cubic smoothing spline with weights proportional to the MCD43A2 QA/QC flags. Finally, the phenological transition dates are identified using a set of relative EVI2 thresholds. The onsets of greenup, greenup midpoint, and maturity are respectively retrieved as the dates when the EVI2 reaches 15%, 50%, and 90% of the greenup segment EVI2 amplitude. Similarly, the onsets of senescence, senescence midpoint, and dormancy are respectively retrieved as the dates when the EVI2 reaches 90%, 50%, and 15% of the greendown segment EVI2 amplitude. As a result, this product has been produced for a 500 m pixel from 2001.

4.5.3. VIIRS LSP product (VNP22Q2)

The VIIRS global LSP product (VNP22Q2 C2) has been produced from daily VIIRS NBAR product (VNP43I) using a Hybrid Piecewise Logistic Model (HPLM) within the Land Surface Phenology Detection (LSPD) algorithm. First, the HPLM-LSPD algorithm preprocesses the raw VIIRS EVI2 time series, following several steps: (1) gap-filling by fusing data with the temporal shape of climatology EVI2, which is calculated from 2013 to 2019 MODIS NBAR data using the Spatiotemporal Shape-Matching Model (SSMM) (Zhang et al., 2021; Zhang et al., 2020a, 2020b); (2) removing snow contamination using the background values that are the combination of bare soil, green leaf (evergreen plants), and non-photosynthetic vegetation during a dormant period (Zhang, 2015); and (3) smoothing of the time series using moving average, moving median, and Savitzky-Golay filters. Second, the HPLM-LSPD reconstructs the temporal EVI2 trajectory using the HPLM that describes the biophysical progress of vegetation growth (Zhang, 2015). Third, the algorithm calculates the curvature-change rate along the reconstructed EVI2 temporal trajectory and identifies a set of extreme values in the curvature-change rate (Zhang et al., 2003). Finally, the phenological transition dates are defined by the timing of extreme value occurrences. The global VIIRS LSP products have been separately provided at a spatial resolution of 500 m and 0.05° from SNPP VIIRS since 2013 and from NOAA-20 VIIRS since 2018. They will also be processed from NOAA-21 VIIRS observations when these become available.

4.5.4. Algorithm for data product continuity

In order to utilize VIIRS LSP detections as a continuation of the MCD12Q2 MODIS product, the challenge of integrating EVI2 time series from different sensors that vary in quality due to different frequencies of low-quality observations during a vegetation growth season must be overcome. The quality of a time series is determined by various factors, including instrument uncertainties, missing observations, atmospheric conditions, and cloud cover (Zhang et al., 2017a), which leads to large gaps in the EVI2 time series. The length of these data gaps has been shown to be the most important determinant of LSP uncertainty (Zhang, 2015). To mitigate this impact, the temporal shape of climatology EVI2 times is utilized to fill the gaps in the VIIRS time series, which is performed using the SSMM algorithm. As a result, the quality of EVI2 time series from SNPP VIIRS and NOAA-20 VIIRS becomes comparable, which greatly improves the continuity of LSP detections.

4.5.5. Evidence of continuity between MODIS and VIIRS LSP

The continuity between VIIRS VNP22Q2 C1 and MODIS MCD12Q2 C6 was investigated via a comparison of 2013 phenological timing in three tiles from the USA (H12V04, H11V04, and H08V05; Moon et al., 2019). Results indicated that the systematic differences between phenological dates from the two products were generally less than one week, and the root mean square differences were less than two weeks for most phenological dates across different land cover classes.

To further investigate the continuity of LSP products detected from MODIS and VIIRS, a comparison of phenometrics was conducted for the products: (1) MCD12Q2 C61; (2) VNP22Q2 C2 from SNPP VIIRS (SNPP-LSP); (3) VNP22Q2 C2 from NOAA-20 VIIRS (NOAA-20-LSP); and (4) MODIS LSP detected from the VIIRS VNP22Q2 C2 algorithm (MODIS-LSP). This comparison focused on the 2019 phenological dates over the selected 9 golden tiles (Table 5). The correlation coefficient was larger than 0.95 among the four LSP detections for all the tiles, and their mean absolute difference (MAD) in 6 out of 9 tiles was <10 days, indicating a very good agreement (Table 5 and Fig. 21). Relatively large discrepancies occurred in arid Australia (H30V11) and the western US (H09V05), as well as in tropical forests (H11V08). The number of pixels with LSP detections was generally similar in mid-high latitudes. However, MCD12Q2 C61 provides far fewer detections in arid and semiarid ecosystems relative to the detections from the VIIRS LSP algorithm (Fig. 22).

4.5.6. Validation of quality of continuity product

The VIIRS LSP product has been validated using various datasets. The six phenological transition dates in VNP22Q2 C1 from the SNPP time series were compared with PhenoCam observations across the USA in 2013 (82 sites) and 2014 (82 sites; Zhang et al., 2018). The results indicated that: (1) the mean absolute difference (MAD) is mostly <10 days for spring events and less than two weeks for autumn events; and (2) the accuracy of phenology detection is relatively higher in forests, followed by grasslands, croplands, and savannas (Fig. 23). Because VIIRS pixel footprints do not match well with PhenoCam imagery spatially, VIIRS phenology detections should be expected to be more comparable to PhenoCam estimates in homogenous sites than in heterogeneous sites. The heterogeneity in arid and semiarid savannas is particularly evident. Grasses and tree crowns are mixed in savanna environments, and phenological dates from PhenoCam imagery during the autumn senescence period can differ by >3 months between the grassland and the tree canopy (Liu et al., 2017c). In addition, the mixture of different tree and grass proportions leads to large variations in the phenological dates of savannas. Thus, VIIRS detections were not as consistent with PhenoCam estimates in savannas, and their dissimilarity increased with the level of heterogeneity or mismatch in the scene (Zhang et al., 2018).

Further, the VNP22Q2 C1 from the SNPP time series was evaluated using in-situ observations from national phenology networks (Ye et al., 2022). The in-situ observations were collected from the Pan European Phenological database (PEP725, 9664 site-years) and the USA National Phenology Network (USA-NPN, 3144 site-years) spanning 2013–2020,

Table 5
Mean absolute difference (days) between four phenology detections.

Tile	H11V03			H09V05		
	MCD12Q2	SNPP	NOAA-20	MCD12Q2	SNPP	NOAA-20
SNPP	9.7			12.8		
NOAA-20	9.7	9		12.4	12.91	
MODIS	8.1	8.3	8.1	9.8	11.7	11.3
	H12V04			**H26V04**		
SNPP	9.6			6.1		
NOAA-20	9.4	8.6		6	5.6	
MODIS	7.7	7.8	7.5	5	5	4.9
	H11V08			**H11V11**		
SNPP	16.7			9.7		
NOAA-20	16.8	17.2		10.2	10.4	
MODIS	11.8	16.1	16	9.1	10.5	11.4
	H20V11			**H30V11**		
SNPP	9.6			13.2		
NOAA-20	9.3	8.2		13.3	9.5	
MODIS	7.3	7.5	7.2	11.8	8.6	9
	H17V07					
SNPP	9.5					
NOAA-20	9.7	8.9				
MODIS	9.5	8.2	8.2			

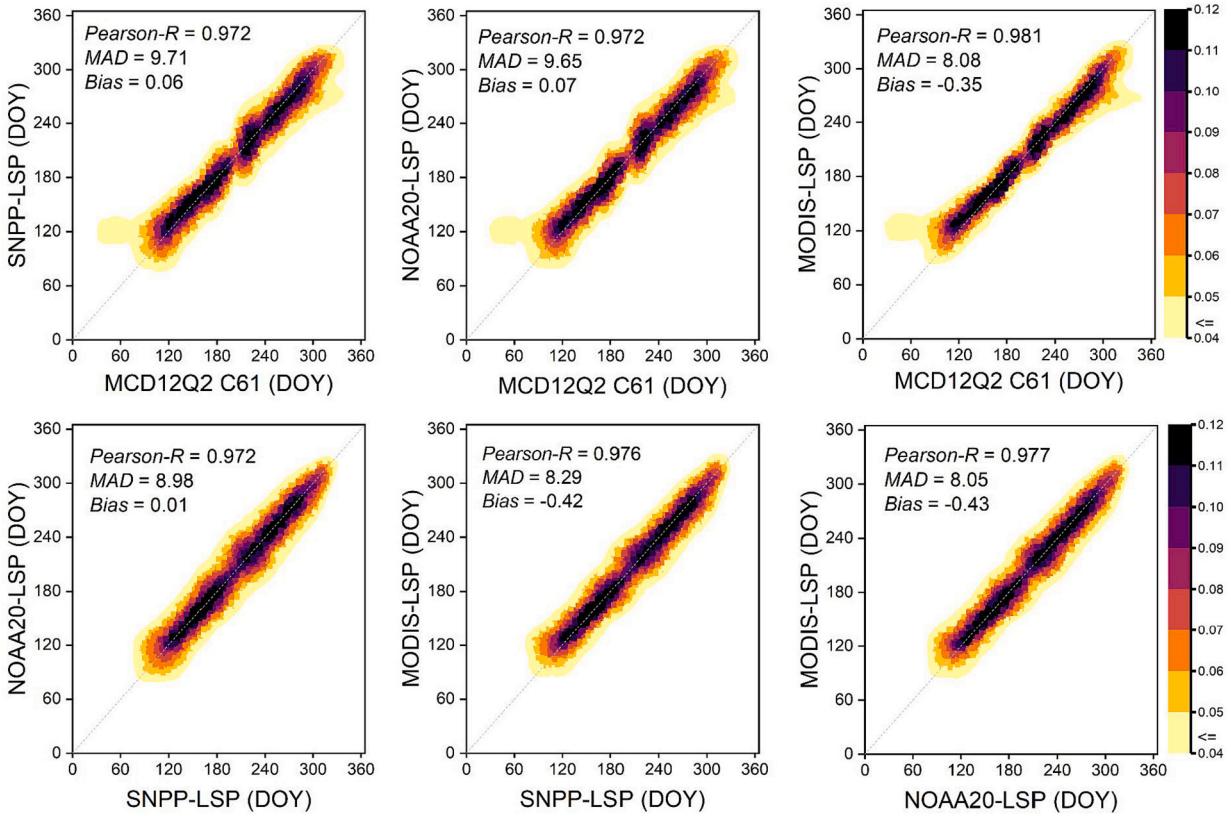

Fig. 21. A comparison of detected LSP dates in the Northwestern Canada golden tile h11v03 from four different products: MCD12Q2 C61, VNP22Q2 C2 from SNPP VIIRS (SNPP-LSP), VNP22Q2 C2 from NOAA-20 VIIRS (NOAA-20-LSP), and MODIS-LSP, which is generated using the VIIRS VNP22Q2 C2 algorithm. The colour shows the relative density of pixels.

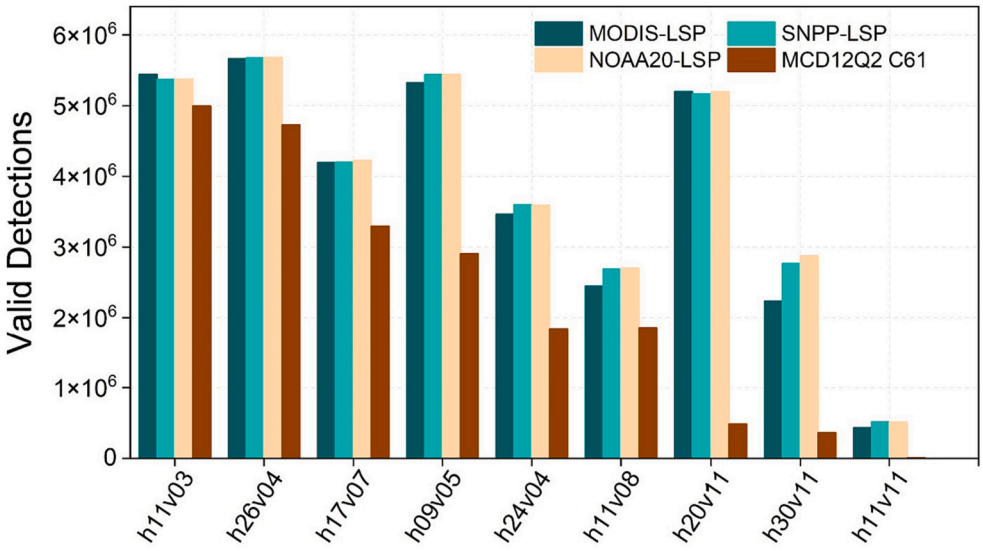

Fig. 22. Number of pixels with valid phenology detections in the 9 golden tiles from four different products: MCD12Q2 C61, VNP22Q2 C2 from SNPP VIIRS (SNPP-LSP), VNP22Q2 C2 from NOAA-20 VIIRS (NOAA-20-LSP), and MODIS-LSP, which was generated using the VIIRS VNP22Q2 C2 algorithm.

where a site-year is a year of data from a single site. The direct comparison indicated that VIIRS greenup onset had a MAD of 13.9 ± 9.8 days with PEP725 in-situ observations and 12.3 ± 10.9 days with USA-NPN observations in certain deciduous forest sites. The interannual comparison revealed that the VNP22Q2 greenup onset exhibits the same directions of multi-year anomalies and long-term trends as those of both PEP725 and USA-NPN observations in over 70% of sample sites.

Although the validation of VNP22Q2 C1 with the PhenoCam network and national phenology networks has shown promise, one critical caveat is that there is a mismatch between the spatial footprint of the PhenoCam and remote sensing measurements. USA-NPN and PEP725 records typically consist of only one or a few organism-scale observations within a VIIRS pixel. Thus, there is a chance that these ground measurements are not representative of the phenological timing

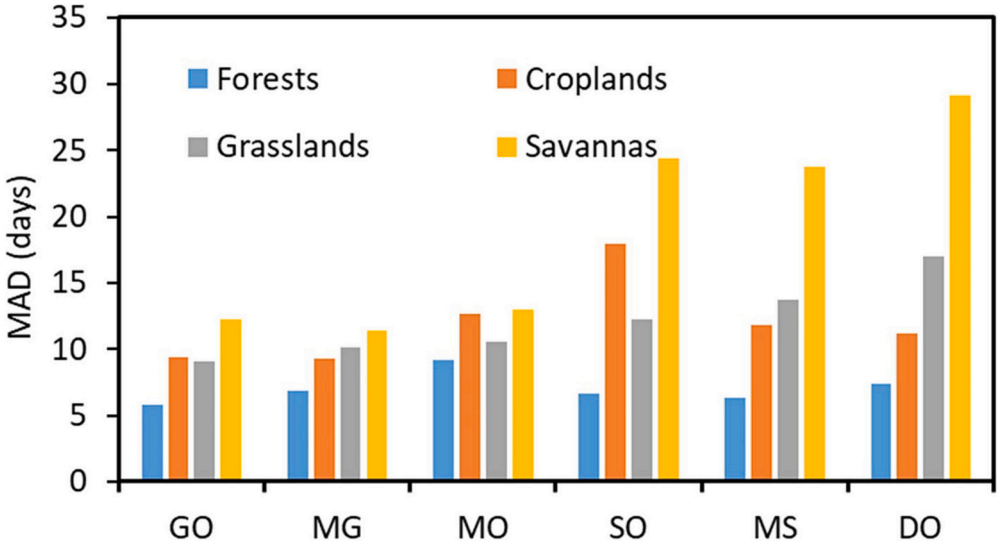

Fig. 23. Validation of Phenometrics using the mean absolute difference (MAD) between VNP22Q2 C1 and PhenoCam observations. Phenometric terms are shorted to GO (greenup onset), MG (middle date in the greenup phase), MO (maturity onset), SO (senescence onset), MS (middle date in senescence phase), and DO (dormancy onset). Figure modified from Zhang et al., 2018.

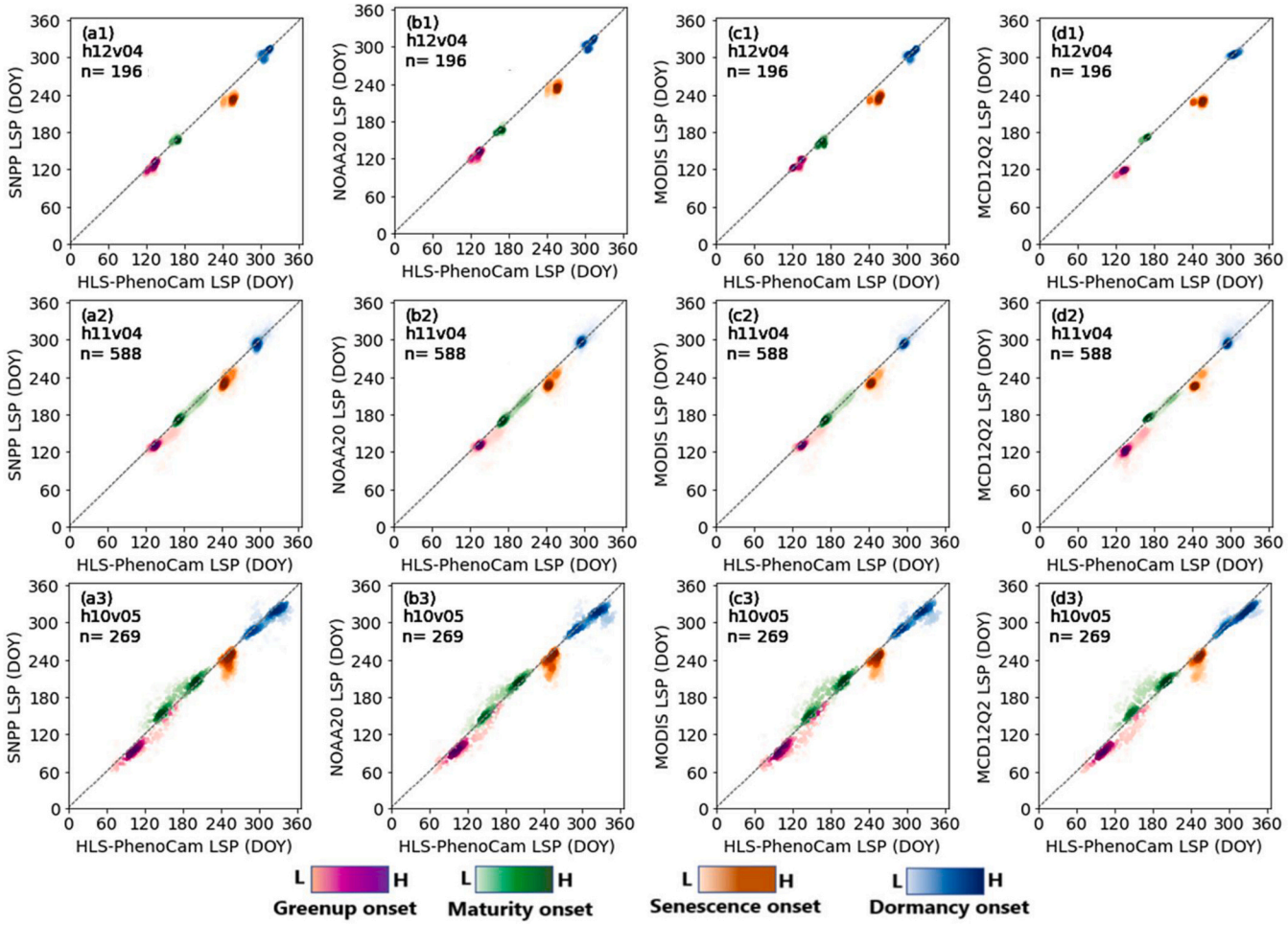

Fig. 24. Scatterplots comparing HLS-PhenoCam phenometrics in 2019 with MCD12Q2 C61 (MCD12Q2 LSP), VNP22Q2 C2 from SNPP VIIRS (SNPP-LSP), VNP22Q2 C2 from NOAA-20 VIIRS (NOAA-20-LSP), and MODIS LSP detected from VIIRS VNP22Q2 C2 algorithm (MODIS-LSP) for the tiles of H12V04, H11V04, and H10V05. Colour density represents sample number from low (L) to high (H), and n indicates the number of samples.

in the entire 500 m LSP product footprint (Zhang et al., 2017b). Similarly, there is a well-known mismatch in view-geometry and spatial coverage between VIIRS pixels and PhenoCam images which could induce large uncertainties in their comparison, particularly in heterogeneous regions. Also, the spatial coverage of PhenoCam imagery differs largely among the sites due to differences in camera height, view angle, and the surrounding topography.

The reference datasets of phenology have been significantly improved for validating VIIRS VNP22Q2 C2. Specifically, the SSMM algorithm is applied to fuse HLS (Harmonized Landsat and Sentinel-2) EVI2 time series with the optimal temporal shape of PhenoCam GCC (Green Chromatic Coordinate) observations selected from a collection of grid-based GCC time series (Tran et al., 2022). This fusion allows for the generation of the synthetic, gap-free HLS-PhenoCam EVI2 time series during a year, which bridges near-surface PhenoCam observations with satellite observation data at various scales. The gap-free HLS-PhenoCam time series produces high-quality phenology datasets across local and regional scales, which can scale to spatially match VIIRS pixels for validation purposes (Tran et al., 2022). As a result, the HLS-PhenoCam phenometrics are detected around PhenoCam sites for the VIIRS tiles of H12V04, H11V04, and H10V05 in the USA.

Fig. 24 and Table 6 present the validation of four different LSP detections (MCD12Q2, SNPP-LSP, NOAA-20-LSP, and MODIS-LSP) using HLS-PhenoCam phenometrics. The result indicates that: (1) phenological dates are very well detected, with an MAD <10 days except in senescence onset; (2) senescence onset from all the MODIS and VIIRS detections is consistently earlier than that from reference; (3) the accuracy in MODIS and VIIRS detections varies by ecosystem, as accuracy is higher in temperate forests (H12V04) and croplands (H11V04) than in shrublands (H10V05); and (4) MCD12Q2 presents relatively larger uncertainties in greenup onset than the other three detection products. Overall, the LSP validation has completed Stage 3.

4.5.7. Status and maturity of the LSP product and algorithm

Based on the selected tiles, the phenometrics from MODIS and VIIRS detections generally agreed well and had little systematic bias. These results suggest that VNP22Q2 C2 could provide global LSP products that continue the MCD12Q2 C61 record. Currently, MCD12Q2 and VNP22Q2 are the only global phenology products that are publicly available. The accuracy of LSP detections is a function of the high quality of temporal observations, where low-quality temporal gaps could result in large uncertainties in LSP. The MODIS phenology product is produced using the time series observed by MODIS Terra and Aqua MODIS, which provides more opportunities to capture cloud-free observations during a vegetation growing season. Because cloud frequency is lower in the morning than in the afternoon, the temporal quality of VIIRS (AM and PM) time series will be significantly improved, which in turn could greatly enhance LSP detections.

However, MCD12Q2 C61 and VNP22Q2 C2 are produced using different algorithms, so some systematic differences are expected. Compared with HLS-PhenoCam phenology, MCD12Q2 shows larger biases than other LSP detections, particularly for the green-up onset (Table 6). Moreover, MCD12Q2 produces far fewer LSP detections in arid and semiarid ecosystems than VNP22Q2, which could limit their use for rangeland research and management (Fig. 22). Finally, MCD12Q2 is likely to produce biases toward earlier dates in some of high-latitude regions, which is likely associated with the impact of residual snow cover (Fig. 21). Therefore, we suggest that MODIS LSP detections should be reprocessed using the VIIRS LSP algorithm, an action which is expected to significantly improve the continuity of the long-term LSP data record. Moreover, we suggest that efforts be made to harmonize the SNPP and NOAA-20 (even NOAA-21) VIIRS products in order to generate a higher quality time series. These efforts should help produce a single VIIRS LSP product with better quality.

4.5.8. Potential impacts of Terra/Aqua MODIS drifting orbits on LSP product

The LSP product takes MODIS NBAR product as the primary input. High-quality phenometrics could be produced from MODIS observations once the MODIS BRDF model accommodates geometrical changes associated with MODIS drifting orbits. This means that the LSP product could experience limited impacts from MODIS drifting orbits.

4.6. Leaf area index (LAI) and the Fraction of Photosynthetically Active Radiation (FPAR)

Primary authors: Jiabin Pu, Yuri Knyazikhin, and Ranga B. Myneni. The relevant MODIS products are Mxx15A2H V6.1. The relevant VIIRS products are Vxx15A2H V2.

4.6.1. Introduction

The MODIS and VIIRS products described in this section cover two parameters directly related to the photosynthesis process: the Leaf Area Index (LAI) and the Fraction of incident Photosynthetically Active Radiation (FPAR). Both LAI and FPAR are widely used in the fields of plant productivity, carbon and water exchange, climate change, and agricultural and forestry management (Chen and Black, 1992; Chen et al., 2019; Zhu et al., 2016; Knyazikhin et al., 1998). LAI quantifies the structural and functional characteristics of vegetation and is defined as the one-sided green leaf area (half of the total area) per unit of ground area. FPAR is derived across the 400–700 nm range of chlorophyll absorption and characterizes the absorption capacity of vegetated land. In general, FPAR values vary by illumination condition. To standardize FPAR across illumination conditions, the MODIS data product provides FPAR under direct solar illumination for the solar zenith angle at a given time of observation.

4.6.2. MODIS products for LAI and FPAR

The Collection 6.1 (C61) MODIS LAI/FPAR product (MYD15A2H), derived from the MODIS sensor on the Aqua platform, provides global coverage at a spatial resolution of 500 m and at a temporal frequency of 8 days since July 4th, 2002. FPAR is estimated at 1:30 pm Local Solar

Table 6
Comparison of HLS-PhenoCam phenometrics in 2019 with MCD12Q2 C61, VNP22Q2 C2 from SNPP VIIRS (SNPP-LSP), VNP22Q2 C2 from NOAA-20 VIIRS (NOAA-20-LSP), and MODIS LSP detected from VIIRS VNP22Q2 C2 algorithm (MODIS-LSP). The greenup onset (GO), maturity onset (MO), senescence onset (SO), and dormancy onset (DO) values are compared. Values represent the number of days.

		H12V04				H11V04				H10V05			
		GO	MO	SO	DO	GO	MO	SO	DO	GO	MO	SO	DO
SNPP-LSP	MAD	6.5	3.9	20.4	4.8	9.0	3.8	13.7	5.9	10.9	10.7	15.3	11.3
	Bias	−6.2	0.2	−20.4	−1.4	−8.7	−1.6	−13.4	−0.9	−9.8	9.1	−14.9	−8.0
NOAA-20-LSP	MAD	6.0	3.5	18.8	5.0	9.2	3.9	15.1	5.4	10.4	8.3	16.2	12.3
	Bias	−5.4	−1.4	−18.7	−2.6	−8.7	−2.4	−15.1	2.0	−9.4	6.5	−16.1	−8.5
MODIS-LSP	MAD	4.4	4.7	18.3	4.7	8.2	3.7	14.4	5.1	10.8	11.1	14.7	10.3
	Bias	−2.5	−3.9	−18.3	−1.9	−7.8	−1.5	−14.2	1.0	−9.3	9.3	−14.6	−6.5
MCD12Q2	MAD	15.4	3.6	23.9	3.7	16.9	3.7	16.0	6.8	13.0	13.4	15.9	8.3
	Bias	−15.4	3.1	−23.9	−1.0	−16.9	−0.5	−16.0	3.1	−12.7	12.6	−15.8	−4.8

Time (LCT). The LAI/FPAR products use the sinusoidal grid tiling system (Myneni and Park, 2015; Yan et al., 2016), and are distributed in hierarchical data format (HDF) files. Each file contains six Science Data Sets (SDS): FPAR, LAI, standard deviations of FPAR and LAI, and two Quality Assessment (QA) variables. Details on the file structure and contents are available in Myneni et al. (2015).

4.6.3. VIIRS products for LAI and FPAR

NASA VIIRS LAI/FPAR products were developed to extend the MODIS long-term LAI/FPAR time series at the same spatial and temporal resolution as MODIS. The data set is being generated by the MODIS LAI/FPAR algorithm (Yan et al., 2018; Park et al., 2017; Knyazikhin and Myneni, 2018). An adjustment technique for the algorithm was developed to ensure consistency in retrievals generated from sensors of different resolutions and spectral band compositions (Ganguly et al., 2008a, 2008b; Chen et al., 2017). The SNPP-VIIRS and NOAA-20-VIIRS Collection 2 (C2) LAI/FPAR products (VNP15A2H/VJ115A2H) were designed to provide a critical bridge between MODIS and VIIRS. Similar to the MODIS product, each file includes six Science Data Sets (SDSs) (FPAR, LAI, standard deviations of FPAR and LAI, and two QA variables), which are distributed as the HDF − EOS5 (H5) files. However, in contrast to the MODIS LAI/FPAR products that are produced from both morning (Terra, MOD15A2H) and afternoon (Aqua, MYD15A2H) observations, the C2 VIIRS LAI/FPAR products are only produced from afternoon observations.

4.6.4. Algorithm for data product continuity

The MODIS/VIIRS LAI/FPAR retrieval algorithm consists of a main algorithm that relies on a Look-up-Table (LUT) and a back-up algorithm that uses empirical relationships between NDVI and LAI/FPAR (Knyazikhin, 1999; Knyazikhin et al., 1998; Park et al., 2017). The LUT used in the main algorithm contains solutions of the radiative transfer equation corresponding to various combinations of sun-sensor geometries, biome types, LAI, and soil brightness. It inputs Bidirectional Reflectance Factors (BRFs) at red and NIR spectral bands, model and observation uncertainties, sun-sensor geometry, and biome type (Myneni and Park, 2015; Knyazikhin and Myneni, 2018). The main algorithm compares observed and modeled spectral BRFs for a suite of canopy structures and soil patterns that represent an expected range of typical conditions for a given biome type. All canopy and soil patterns and corresponding FPAR values for which modeled and observed BRFs differ within a specified uncertainty level are considered to be acceptable solutions. The mean values of LAI and FPAR, their dispersions, and their standard deviations are reported as retrievals, along with their uncertainties (Knyazikhin et al., 1998).

When sampling dense vegetation canopies, the measured reflectance values can saturate and become insensitive to variation in canopy properties. Since the dispersion of the solution distribution is large, data retrieved under the conditions of saturation are less reliable, and therefore these retrievals paths are flagged in QA layers.

If the main algorithm fails to find a solution, the back-up algorithm is utilized. The back-up algorithm first accumulates retrievals over 8-day intervals, and then it selects one that corresponds to maximum FPAR value (Yan et al., 2016; Yan et al., 2018). Analyses of the MODIS LAI/FPAR algorithm performance indicate that the best-quality, high-precision retrievals are obtained from the main algorithm (Chen and Black, 1992; Chen et al., 2019; Zhu et al., 2016; Chen et al., 2017). The retrieval index (RI), defined as the percentage of pixels for which the main algorithm produces a retrieval, is an important characteristic of the algorithm performance, characterizing the spatial coverage of the best-quality, high-precision retrievals and not their accuracies.

4.6.5. Evidence of continuity between MODIS and VIIRS LAI and FPAR

As SNPP-VIIRS and NOAA-20-VIIRS are expected to continue the long-term MODIS LAI/FPAR time series from Terra and Aqua missions, it is crucial to ensure consistency between MODIS and VIIRS LAI/FPAR products on a global scale (Xu et al., 2018; Yan et al., 2018; Yan et al., 2021). Here, we compared annual average values of LAI, FPAR, RI, StdLAI, and StdFPAR from Aqua MODIS (MYD15A2H), SNPP VIIRS (VNP15A2H (Fig. 25), and NOAA-20 VIIRS (VJ115A2H Fig. 26) to assess consistency between VIIRS and MODIS.

First, as shown in Figs. 10 and 11, both MODIS and VIIRS LAI/FPAR

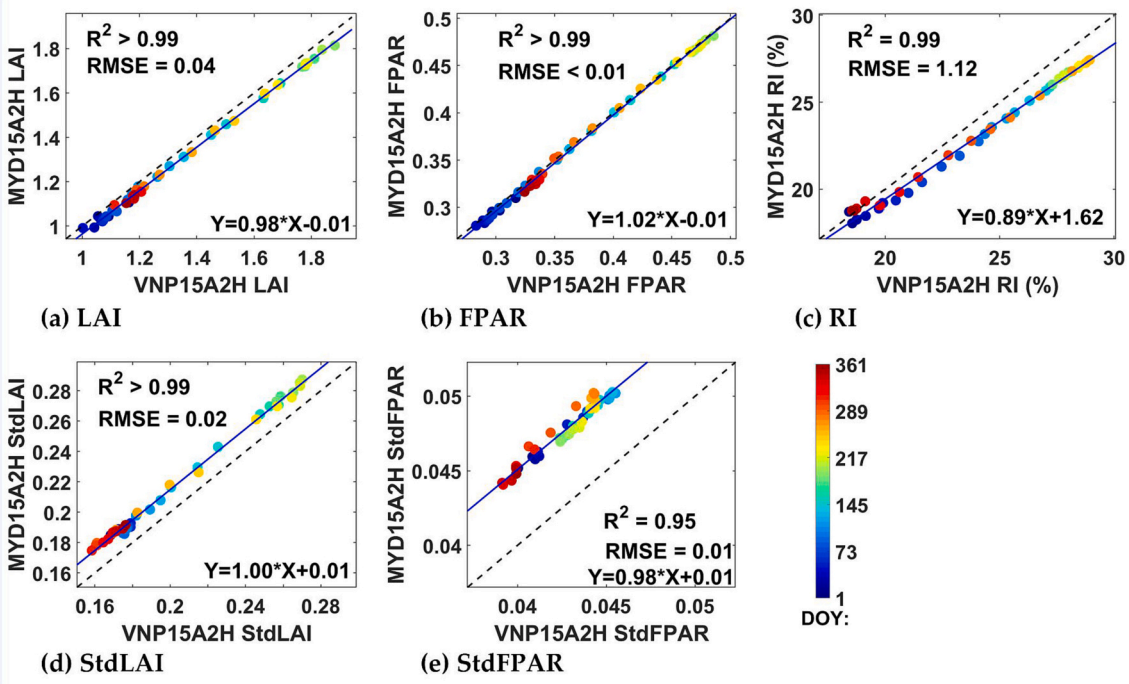

Fig. 25. Comparisons of LAI (a), FPAR (b), RI (c), StdLAI (d), and StdFPAR (e) derived from Aqua MODIS (MYD15A2H C61), and C2 SNPP VIIRS (VNP15A2H C2) for year 2018 globally. The dotted symbols are colour-coded by DOY, and black and blue lines represent the diagonals and linear fit lines, respectively. (For interpretation of the references to colour in this figure legend, the reader is referred to the web version of this article.)

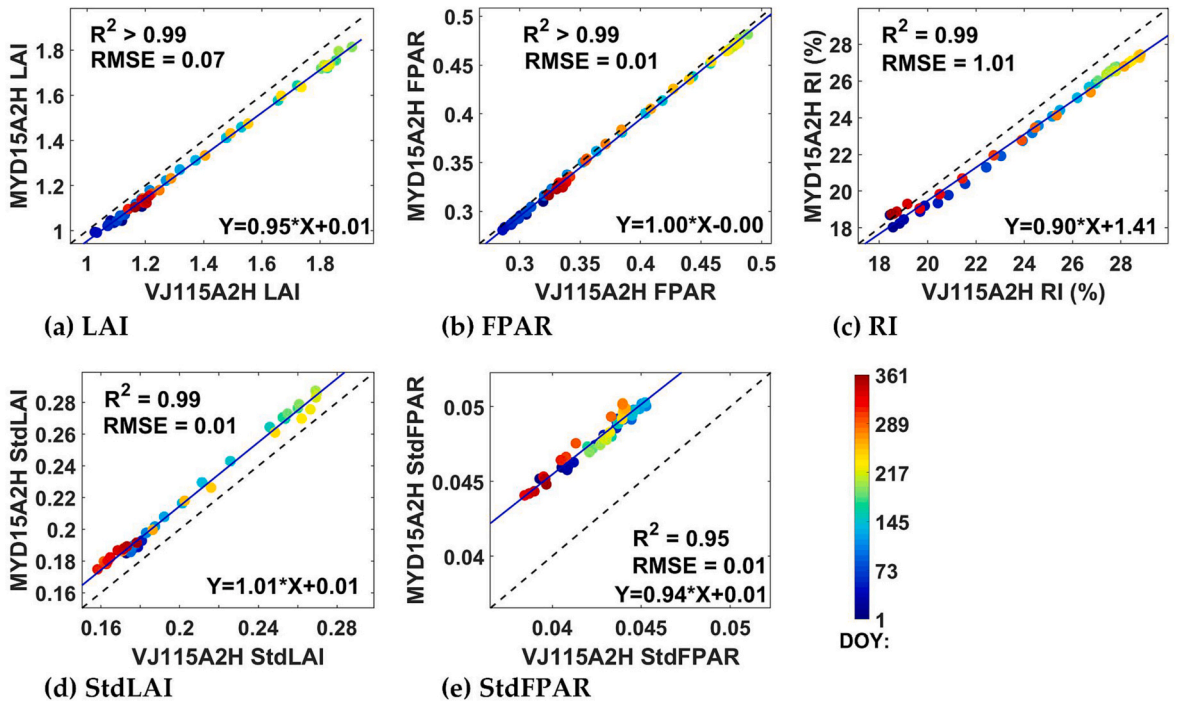

Fig. 26. Comparisons of LAI (a), FPAR (b), RI (c), StdLAI (d), and StdFPAR (e) derived from Aqua MODIS (MYD15A2H C61) and C2 NOAA-20 VIIRS (VJ115A2H C2) for year 2018 globally. The dotted symbols are colour-coded by DOY, and black and blue lines represent the diagonals and linear fit lines, respectively. (For interpretation of the references to colour in this figure legend, the reader is referred to the web version of this article.)

products exhibited a very high consistency with respect to R^2, exceeding 0.95 for all retrievals and quality indexes, suggesting a strong relationship and good prospects for continuity. Secondly, compared to MYD15A2H, both VNP15A2H and VJ115A2H exhibited a slight systematic underestimation for the standard deviation of LAI and FPAR, but still demonstrated a high degree of consistency (RMSE $\leq$ 0.02). Finally,

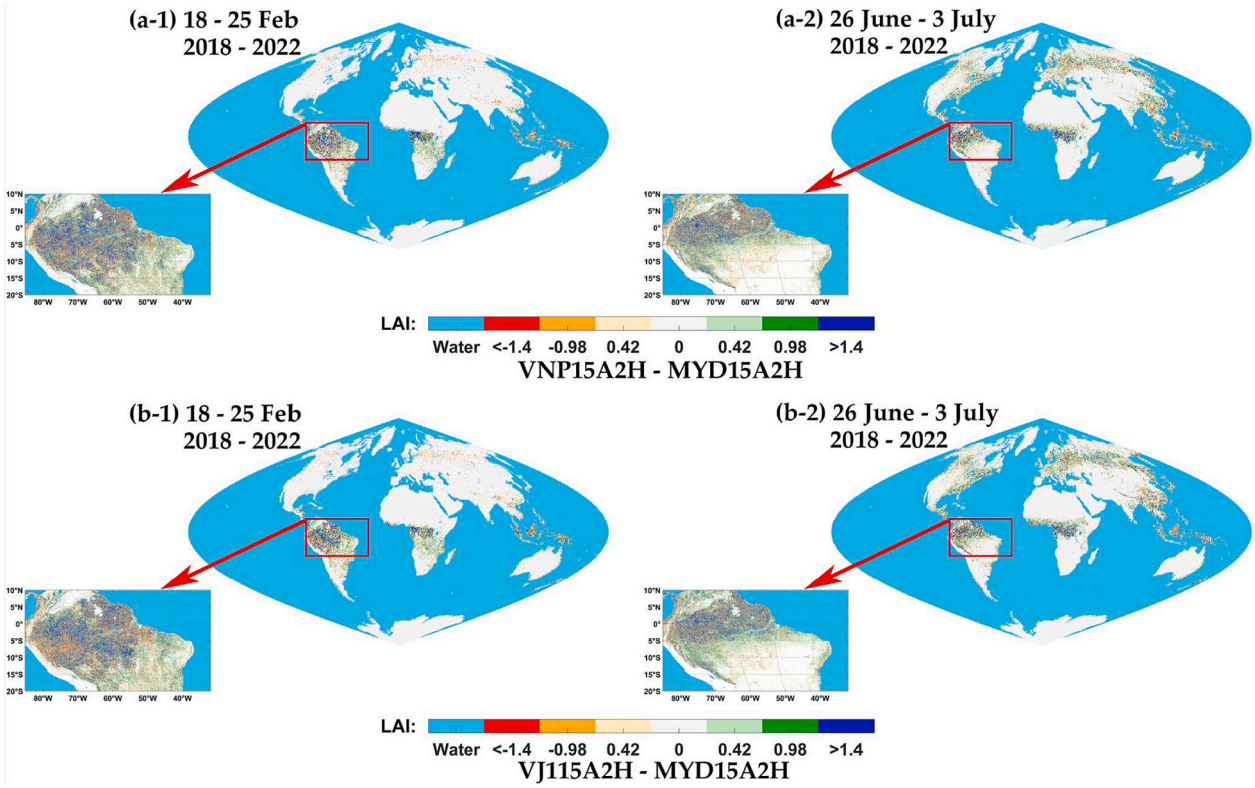

Fig. 27. The global distribution of annual average LAI difference (VIIRS-MODIS) in each 5 $\times$ 5 km grid from 2018 to 2022 for two observation dates (18–25 February and 26 June(a) displays the difference between MYD15A2H C61 and VNP15A2H C2, while panel (b) shows the difference between MYD15A2H C61 and VJ115A2H C2. An equal-area Sinusoidal projection is used here.

we observe seasonality in both retrievals and quality indexes, with values increasing from January to June and decreasing thereafter.

Fig. 27 displays the global spatial patterns of annual average LAI differences between MODIS and two VIIRS products over the five-year period between 2018 and 2022 for two typical observation dates (18–25 February and 26 June–3 July). The corresponding FPAR is shown in Fig. 28.

Statistics of LAI/FPAR differences shown in Table 7 suggested consistent LAI/FPAR distributions with no observed systematic bias between MODIS and VIIRS products in both seasons. In February, the overall differences of LAI and FPAR for both sensors were within ±0.5 for about 86% of retrievals and within ±0.05 for about 72%, with larger differences over dense forests. In higher latitudes of the northern hemisphere, the LAI/FPAR retrievals showed a slightly larger difference in July than in February. The percentage of LAI/FPAR differences within ±0.5 and ± 0.05 decreased to 79.05%/77.17% (VNP15A2H/VJ115A2H) and 65.34%/62.12%, respectively. This can be attributed to the invalid LAI/FPAR retrievals in the northern hemisphere high-latitude region during winter, due to large solar zenith angles and snow cover. In general, MODIS and VIIRS showed a high consistency, which was also demonstrated by the low percentage of pixels that differed greatly. The percentage of LAI differences above ±1.4 are 4.05%/4.04% (VNP15A2H/VJ115A2H) and 3.17%/3.20% for February and July, respectively. The corresponding percentage for FPAR differences over ±0.2 were 4.96%/6.07% and 3.47%/4.27%.

Table 7
The percentage of LAI/FPAR differences between MODIS and VIIRS for February and July.

		Within ±0.5 (LAI) and ± 0.05 (FPAR)	[±0.5, ±1.4] (LAI) and [±0.05, ±0.2] (FPAR)	Over ±1.4 (LAI) and ± 0.2 (FPAR)
LAI	VNP15A2H-MYD15A2H (February)	86.25%	9.70%	4.05%
	VJ115A2H-MYD15A2H (February)	86.08%	9.88%	4.04%
	VNP15A2H-MYD15A2H (July)	79.05%	17.78%	3.17%
	VJ115A2H-MYD15A2H (July)	77.17%	19.63%	3.20%
FAPR	VNP15A2H-MYD15A2H (February)	72.38%	22.66%	4.96%
	VJ115A2H-MYD15A2H (February)	72.89%	21.04%	6.07%
	VNP15A2H-MYD15A2H (July)	65.34%	31.19%	3.47%
	VJ115A2H-MYD15A2H (July)	62.12%	33.61%	4.27%

4.6.6. *Validation of quality of continuity product*

This section presents a comparative analysis of the MODIS and VIIRS LAI/FPAR global products, which shows that the LAI/FPAR values of the VIIRS C2 version are in good agreement with its MODIS C61 counterpart in terms of spatial distribution, time-series variability, and comparisons with ground truth measurements. Fig. 29 presents comparisons of Copernicus ground-based measurements for validation (GBOV) of LAI/FPAR for MODIS C61 and VIIRS C2 LAI/FPAR, respectively (Brown et al., 2020). The comparable values of R^2, RMSE, and bias when compared to ground truth data suggest consistency of uncertainties in VIIRS and MODIS LAI/FPAR retrievals. Notably, both products showed a tendency to overestimate low LAI/FPAR and underestimate high FPAR. Moreover, VIIRS C2 outperformed MODIS C61 in terms of LAI retrieval accuracy, with a decrease in RMSE from 0.94 (MYD15A2H) to 0.87/0.89 (VNP15A2H/VJ115A2H) and an increase in R^2 from 0.67 to 0.72/0.71. Similarly, for FPAR, the R^2 increased from 0.70 to 0.75/0.75.

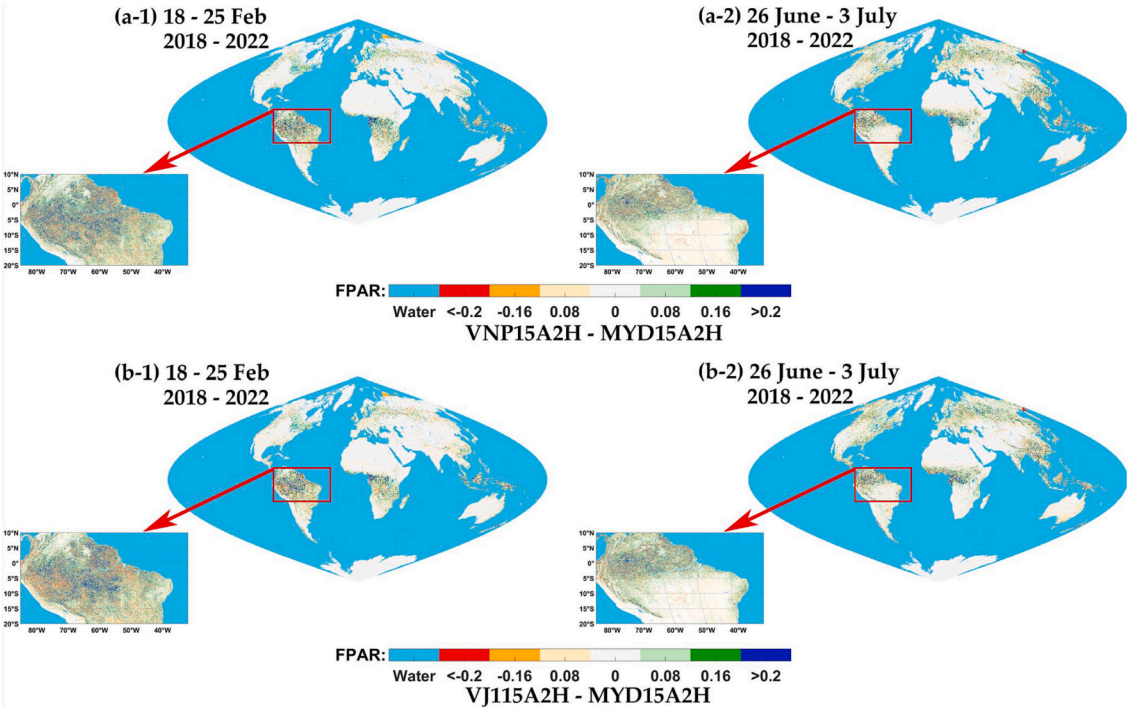

Fig. 28. The global distribution of annual average FPAR difference (VIIRS-MODIS) in each 5 × 5 km grid from 2018 to 2022 for two observation dates (18–25 February and 26 June–3 July). Panel (a) displays the difference between MYD15A2H C61 and VNP15A2H C2, while panel (b) shows the difference between MYD15A2H C61 and VJ115A2H C2. An equal-area Sinusoidal projection is used here.

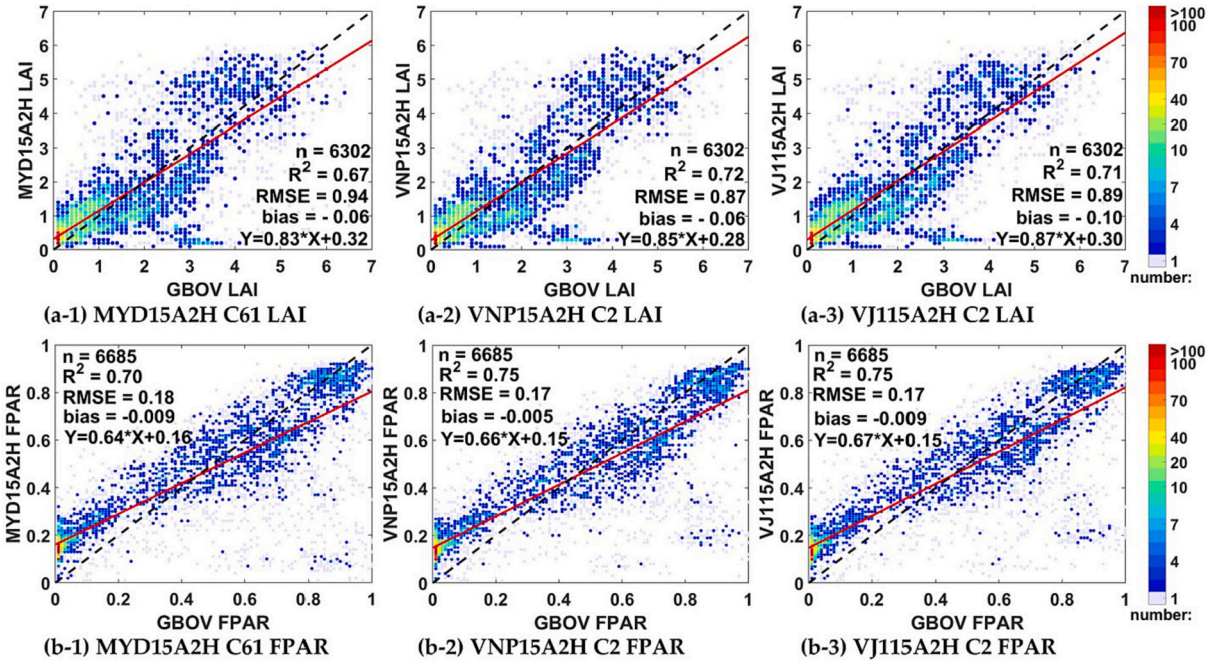

Fig. 29. Comparisons of MYD15A2H/VNP15A2H/VJ115A2H LAI/FPAR with ground GBOV LAI/FPAR measurements.

4.6.7. Status and maturity of LAI and FPAR products and algorithms

The product uncertainty of all three LAI products (MYD15A2H, VNP15A2H, and VJ115A2H) falls within ±0.5, satisfying the global climate observing system (GCOS) uncertainty requirements for land surface products. Specifically, MYD15A2H and VNP15A2H have an uncertainty of −0.06, while VJ115A2H has an uncertainty of −0.10. Similarly, the FPAR values for MYD15A2H, VNP15A2H, and VJ115A2H have an uncertainty requirement of ±0.05 with a bias of −0.009, −0.005, and − 0.009, respectively.

While both morning and afternoon data are available from MODIS, VIIRS only provides afternoon data. However, LAI is independent of illumination conditions during a day. Its satellite-based estimate can vary only within model and observation uncertainties between morning and afternoon observations since the retrieval algorithm accounts for angular effects. However, the FPAR varies with the direction of the incident solar beam. The morning and afternoon FPAR values therefore can differ. The MODIS main algorithm is adjustable for sensor spatial resolution and spectral band composition (Ganguly et al., 2008a, 2008b; Chen et al., 2017) and therefore is able to generate "seamless" LAI/FPAR time series using data from multiple sensors as evidenced from a good consistency of the LAI/FPAR product derived from MODIS and VIIRS sensors on different platforms.

4.6.8. Potential impacts of Terra/Aqua MODIS drifting orbits on LAI and FPAR

The sensitivity of the LAI retrieval algorithm to changes in observation angle due to orbital drift has been fully assessed and found to be negligible (Pu et al., 2020). The algorithm is designed to be robust against such variations, and therefore, changes in observation angle are not expected to affect the accuracy and reliability of the LAI retrievals. However, the FPAR is directly influenced by incident solar radiation. Change in the equator-crossing time from 10:15 AM to 9:00 AM results in a significant shift in SZA. For example, for the Amazon Forest region, SZA will increase from about 27° to 50° in March. Accounting for such changes when using the FPAR product derived during the orbital shift is important.

4.7. Evapotranspiration (ET)

Primary authors: John Kimball, Arthur Endsley, and Maosheng Zhao. The relevant MODIS products are 8-day MxD16A2 and annual MxD163 V6.1. The relevant VIIRS products are 8-day Vxx16A2 and annual Vxx16A3.

4.7.1. The MODIS ET product

Energy from the Sun received by the land surface is partitioned into sensible heat flux, heat transferred to the subsurface, or latent heat used to evaporate water. The latent energy flux can include evaporation from bare soil and wet leaves, and canopy transpiration, which together define the bulk evapotranspiration (ET) flux. ET is a major component of the terrestrial water budget and accounts for the annual atmospheric return of over 60% of the precipitation over land (Mu et al., 2011). ET (and latent energy) also represents the primary link between the terrestrial water and energy cycles, and ET is included as an Essential Climate Variable by the Global Climate Observing System (GCOS). MOD16 ET is modeled as the sum of the instantaneous rates of wet canopy evaporation, soil evaporation, and canopy transpiration. MOD16 8-day ET is an estimate of the average latent heat flux given the composite vegetation cover (fPAR) and leaf area index (LAI) from the corresponding MODIS MOD15 product and prevailing climate drivers, particularly the net radiation received by the land surface. The operational MOD16A2H 8-day ET product is estimated at 500 m spatial resolution for the global land domain, providing a continuous record of ET environmental trends over the EOS MODIS era.

4.7.2. VIIRS ET product

As the NASA EOS MODIS era approaches end of mission, the continuity of similar spectral measurements from NOAA SNPP and NOAA-20 VIIRS provides the means for extending the global ET environmental data record (EDR) using the established MOD16 framework. Canopy fPAR and LAI from the VIIRS VNP15 products are largely consistent with the same product retrievals from MODIS (MOD15), providing critical inputs for MOD16 ET processing. Thus, the equivalent VNP15 products provide an effective alternative to MODIS MOD15 data in the production of a new VIIRS VNP16A2H product. Given the strong consistency between MOD15 and VNP15 canopy retrievals, no significant structural

changes to the established MOD16 framework are necessary for continuity under VIIRS. Minor re-calibration of model parameters and harmonization of VNP15 and MOD15 inputs is expected to produce a similarly high level of accuracy and consistency between MOD16 and VNP16 ET. The same calibration and validation (Cal-Val) procedure used for MOD16 will also apply to the new VIIRS VNP16 record to ensure optimal ET performance. A consistent model calibration will be applied to the entire ET record by dynamically adjusting critical model parameters to minimize the root mean square difference (RMSD) between model ET (or latent energy) predictions and daily ET observations from a global network of eddy covariance (EC) flux towers.

4.7.3. Algorithm for data product continuity

Both MOD16 and VNP16 estimate ET using an established Penman-Monteith (PM) model (Mu et al., 2011; Zhang et al., 2016). The PM model uses electrical analog theory to estimate latent energy from the net solar energy available for evaporation at the land surface. The PM Model accounts for the balance between the atmospheric moisture demand and the surface resistance to moisture loss from aerodynamic roughness, soil, and plant canopy stomatal restrictions. A key PM innovation is the central role of vegetation canopy conductance and transpiration in regulating the land-atmosphere exchange of heat and water vapor. The PM approach is also highly amenable to the use of satellite remote sensing observations of vegetation cover and spatial energy partitioning as key model drivers.

4.7.4. Evidence of continuity between MODIS and VIIRS ET products

We compared estimates of latent heat from MOD16 using canopy fPAR and LAI data from different satellite sources for the same MOD16 Collection 6.1 model parameters. When we compared latent heat estimates at 279 EC flux towers from Aqua MODIS (MYD15) and Terra MODIS (MOD15) input fPAR and LAI, we saw strong correspondence in latent heat estimates (Fig. 30a), despite differences in the mean local acquisition time (morning overpass for Terra MODIS, afternoon for Aqua MODIS). When we compared estimates based on Aqua MODIS data to those based on VIIRS (VNP15), where both platforms had mean local acquisition times in the afternoon, we saw even greater consistency in latent heat estimates (Fig. 30b), indicating strong potential for seamless continuity between MODIS and VIIRS ET records. A global recalibration of model parameters and bias correction of any systematic differences in the MOD15/MYD15 and VNP15 records is expected to further improve ET consistency and performance.

4.7.5. Validation of quality of continuity product

Product validation primarily involves comparing model outputs against independent tower ET measurements and other global observational ET benchmarks, following protocols established from previous studies (Mu et al., 2011; Zhang et al., 2016). When assessed against eddy covariance (EC) tower fluxes, MOD16 (Collection 6.1) and the VNP16 test data had very similar performance, with an overall RMSE of 1.6 mm per day in relation to independent ET observations from 279 globally distributed EC tower sites. The accuracy of ET estimates was essentially the same regardless of whether Terra MODIS or Aqua MODIS data were used, with slightly lower bias and RMSE seen with Aqua MODIS data, which was likely due to greater reliance upon the fPAR and LAI climatology. Moreover, preliminary validation of an updated ET record derived from a recalibrated MOD16 model (reflecting a greater collection of EC tower fluxes for calibration) showed even better ET performance, reducing the test RMSE by about 0.5 mm day^{-1} and with a significant reduction in model bias. The largest reductions in bias were associated with Evergreen Broadleaf and Deciduous Broadleaf forests. All Plant Functional Types saw improvements except for Grasslands, which maintain similar performance to the baseline MOD16 Collection 6.1 product. Similar model recalibration, validation, and reprocessing efforts are planned for VNP16 operations.

4.7.6. Status and maturity of ET products and algorithms

The MOD16 product accuracy and performance is well documented in the literature, with extensive global validation studies involving detailed ET comparisons with tower EC measurements and other observational benchmarks (e.g., Zhang et al., 2019; Souza et al., 2019; Tang et al., 2015; Hu et al., 2015). Product refinements and improvements have also been documented, resulting from periodic reprocessing of a longer MOD16 operational record and leading to the current Collection 6.1 baseline product. While the MOD16 model and product are mature (Stage 4, CEOS LPV), the VNP16 product stream is still at an early (Stage 1) maturity level. However, given the strong consistency of the MOD16 and preliminary VNP16 results, accelerated growth in VNP16 product maturity is expected as the EOS era approaches end of mission.

4.7.7. Potential impacts of Terra/Aqua MODIS drifting orbits on ET

Potential orbital drift in the mean local overpass time (MLT) of MODIS sampling from the Terra and Aqua satellites may lead to differences in the quality of MODIS MCD43 albedo and MOD15A2H and MYD15A2H fPAR and LAI retrievals, which are key inputs for MOD16

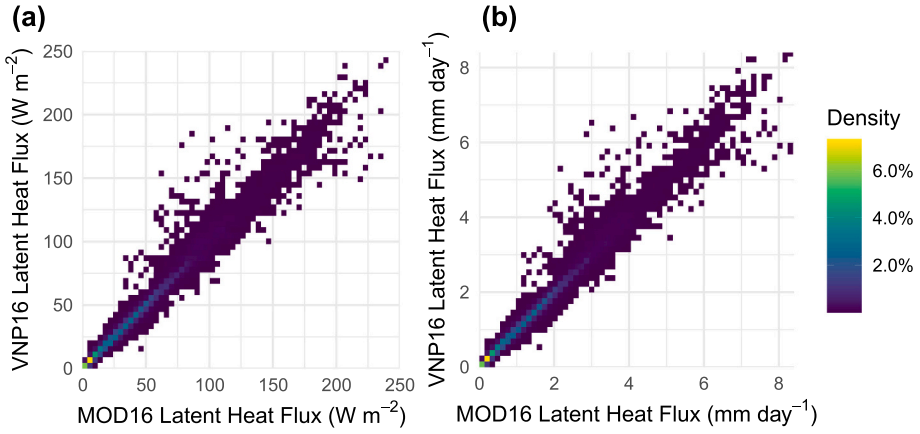

Fig. 30. Estimates of latent heat flux using the same MOD16 Collection 6.1 model framework but canopy fPAR and LAI inputs from different satellites, for 279 globally distributed EC flux towers. At left, estimates based on Aqua MODIS MYD15 data were compared to those based on Terra MODIS MOD15 data. At right, estimates based on Aqua MODIS MYD15 data were compared to those based on SNPP VIIRS VNP15 data. Even without model recalibration or harmonization, estimates from the two sensors were very similar. The same MODIS MCD43 albedo, using sensor data from both Terra and Aqua, was used to produce all datasets shown. Each cell in the density plots represents a plot area of 5 W m^{-2} along both axes. (For interpretation of the references to colour in this figure legend, the reader is referred to the web version of this article.)

production. Expected MLT drift toward earlier (Terra) and later (Aqua) daily sampling may improve MOD15 quality in the humid tropics by avoiding excessive mid-day cloud cover, whereas MYD15 quality may degrade due to greater cloud contamination from sampling later in the day in this region. Data from both platforms may also be impacted by lower solar angles, which could degrade MODIS fPAR and LAI performance. However, potential negative impacts of the drifting satellite orbits on ET performance are expected to be negligible due to ongoing recalibration and mitigation efforts of the product teams that provide the key MODIS inputs for MOD16 processing.

4.8. Gross Primary Production (GPP) and Net Primary Production (NPP)

Primary authors: John Kimball, Arthur Endsley, and Maosheng Zhao. The relevant MODIS products are 8-day MxD17A2H and annual MxD17A3HGF. The relevant VIIRS products are 8-day Vxx17A2[GF] and annual Vxx17A3GF.

4.8.1. MODIS GPP and NPP products

Terrestrial gross primary production (GPP) is the amount of carbon (in the form carbon dioxide, CO2) exchanged between the atmosphere and terrestrial plants through photosynthesis. It is the primary way that carbon (C) energy enters ecosystems, where it is stored as carbohydrates and others forms in plant tissues. As some of this assimilated C is consumed as part of plant metabolism, net primary production (NPP) is the amount of C retained in plant biomass, which provides C and energy for other ecosystem processes and services, including for use as food, fiber, or fuel in human societies. NPP is the largest part of the global land C sink and is the basis for the accumulation of biomass, an essential climate variable defined by the Global Climate Observing System (GCOS). The MODIS MOD17A2H(GF) product provides 8-day GPP estimates at 500 m resolution for the global land domain. At the same spatial and temporal resolution, the MODIS MOD17A3H(GF) product provides annual GPP and NPP estimates, the latter accounting for C lost through autotrophic respiration in annual growth of plant tissues (Running et al., 2004; Zhao et al., 2005). These products have established a consistent, long-term (23-year) record of variability and trends in GPP and NPP based on global climate datasets and MODIS observations of vegetation cover and leaf area index (LAI). The resulting products provide a climate sensitive indicator of patterns and trends in vegetation growth, terrestrial carbon sink activity, and other ecosystem services (Jones et al., 2020; Yao et al., 2020).

4.8.2. VIIRS GPP and NPP products

As NASA MODIS approaches the end of its mission, the continuity of similar spectral measurements from NOAA SNPP and NOAA-20 VIIRS provides the means for extending the global GPP and NPP environmental data records (EDRs), using the established MOD17 framework. The new VIIRS VNP17A2GF and VNP17A3GF gap-filled products have been generated using the same MOD17 algorithm. Recently, these products have been re-calibrated and validated against GPP derived from a global network of eddy covariance flux towers and field measurements of NPP, using the same meteorological driver data as MODIS (Endsley et al., 2023). The VNP17 products have the same spatial and temporal resolution as the MOD17 products and are available at 8-day and annual time intervals starting in 2012.

4.8.3. Algorithm for data product continuity

MOD17 and VNP17 products are generated using the well-established light-use efficiency approach originally described by Monteith (1972), who suggested that the NPP of well-watered plants without nutrient limitations was linearly related to the amount of solar energy that plants absorbed over the growing season. This assumption was later extended to account for reductions in the rate of photosynthesis due to unfavorable conditions, including low temperatures and excessive dryness. The resulting model has repeatedly demonstrated its robustness for global operations and underpins the 8-day and annual GPP estimates in MOD17/ VNP17 products (Endsley et al., 2023).

Allometric relationships in plant tissues, based on field studies, are further used to determine the metabolic C costs of maintaining leaves, fine roots, and live woody tissues. These autotrophic respiration costs are subtracted from GPP to estimate NPP.

A key feature of the VNP17 products is their consistency with the MOD17 products, owing to a bias correction applied to the re-calibrated model parameters of different land-cover types associated with maximum light-use efficiency (LUE) and specific leaf area (SLA) (Endsley et al., 2023). These two parameters are sensitive to differences between MODIS and VIIRS in their retrievals of canopy cover and LAI. With this correction, end-users can seamlessly extend the MOD17 record (since 2000) with VNP17 data, which will likely extend the global GPP and NPP records through 2030.

4.8.4. Comparison of MODIS and VIIRS GPP and NPP products

Differences between the MODIS and VIIRS sensor design and sampling methods can contribute to downstream MOD17/VNP17 product differences or biases, even though the underlying algorithms are the same. However, the product differences can be mitigated through model parameter cross-calibration by overlapping product streams against reference observational benchmarks.

The bias correction in VNP17 calibration has clearly reduced the bias between the two products. Fig. 31 shows a comparison of annual GPP and NPP estimates from each product, where the coefficient of determination (R^2), describing the relationship between the VNP17A3HF estimates and the MOD17A3HGF estimates, was essentially 1.0. Overall, relative differences indicated by bias, RMSE, and mean values of GPP and NPP were very minor at the global scale (54 g C m^{-2} $year^{-1}$ for GPP and 19 g C m^{-2} $year^{-1}$ for NPP), as shown in Fig. 31. Linear slopes showed that GPP was relatively lower for the afternoon Aqua MYD17 annual GPP and NPP values than for VNP17 within highly productive regions like tropical rainforests, which are frequently obscured by cloud cover during the afternoon Aqua overpass. Bias correction was based on morning Terra MODIS data and, consequently, higher cloud cover in Aqua MODIS retrievals resulted in a regression to the mean (climatological) values for fPAR and LAI, which in turn resulted in lower GPP and NPP estimates from Aqua than from Terra.

4.8.5. Validation of quality of continuity product

The updated MOD17 and new VNP17 products have almost identical parameter tables, other than small adjustments to the maximum LUE and SLA parameters. GPP estimates based on MODIS and VIIRS sensors were validated against eddy covariance flux tower data and found to have nearly identical performance metrics (Endsley et al., 2023), both improving upon the baseline MODIS Collection 6.1 product. Annual NPP estimates from both sensors were subjected to cross-validation against field studies and found to be quite similar (ibid.). In a comparison against independent top-down and bottom-up estimates, VNP17A3GF NPP estimates were found to have smaller differences than the corresponding MOD17A3HGF NPP estimates (ibid.).

4.8.6. Status and maturity of GPP and NPP products and algorithms

Global GPP and NPP data products from MODIS and VIIRS are produced with the same algorithm, and all the parameters are identical except for two bias-corrected parameters accounting for systematic differences in canopy fPAR and LAI estimates between the two sensors (Endsley et al., 2023). The MODIS GPP and NPP data products have been extensively evaluated and found to be effective for a diversity of science applications, as is documented in the literature. The products have benefited from periodic reprocessing updates and are at validation Stage 4 maturity (CEOS LPV). As a model-enhanced data product, MOD17/ VNP17 requires the use of coarse-resolution, global meteorological data as key inputs. The estimated GPP and NPP are sensitive to the quality of the input meteorological data, and the accuracy of the global

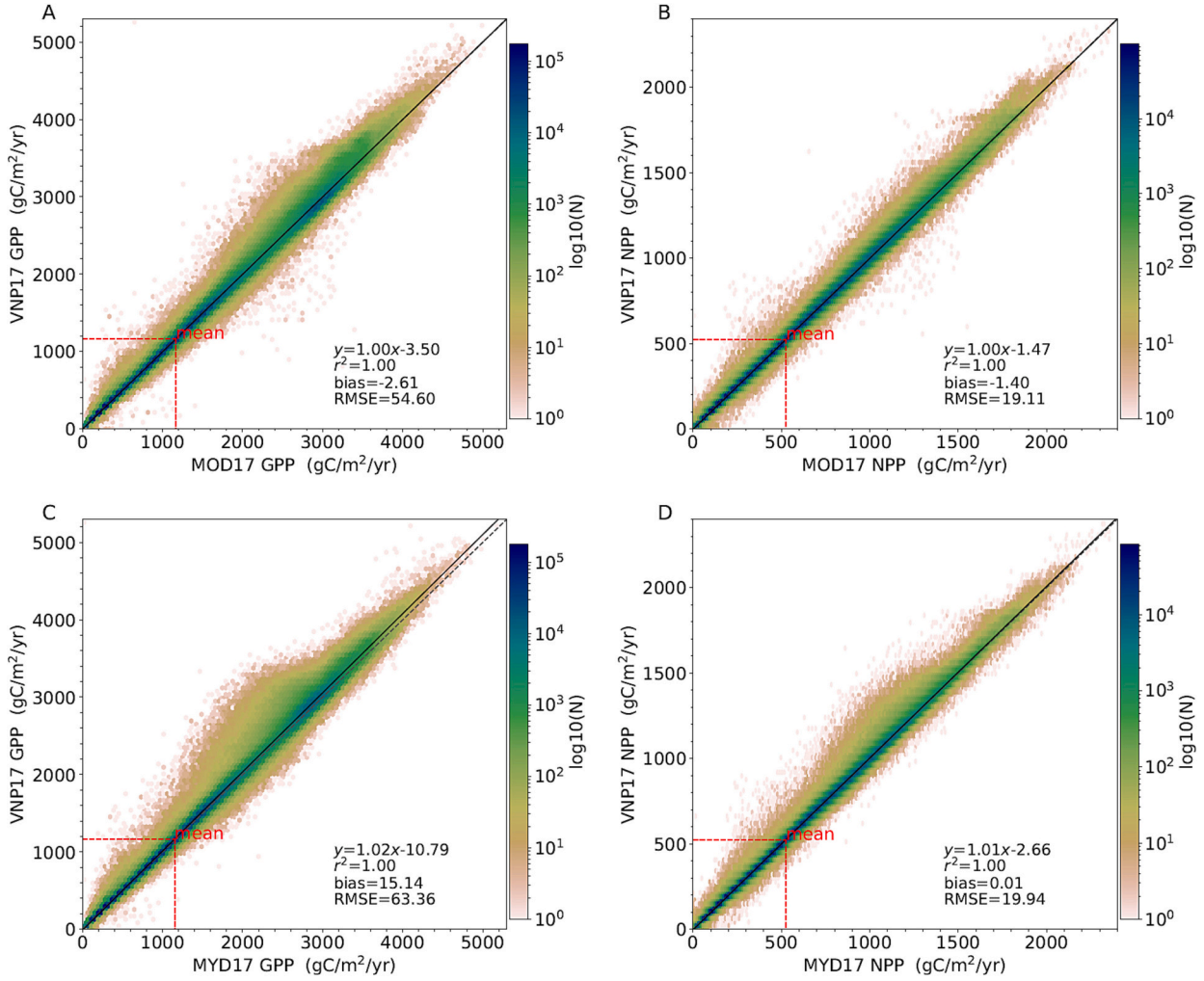

Fig. 31. Estimates of annual GPP and NPP compared between two satellite sensors for source data: VIIRS versus Terra/Aqua MODIS. Estimates of annual GPP (A and C) and annual NPP (B and D) are similar between the updated MOD17A3HGF/MYD17A3HGF and new VNP17A3GF products when both are tested at the 5 km scale between overlap periods from 2012 to 2021 using updated parameters (Endsley et al., 2023). (For interpretation of the references to colour in this figure legend, the reader is referred to the web version of this article.)

meteorological data tends to be lower in tropical regions. Because of this factor and the more frequent cloud cover in the tropics, uncertainties of GPP and NPP tend to be relatively higher in the tropics than extratropics (Zhao et al., 2006).

4.8.7. Potential impacts of Terra/Aqua MODIS drifting orbits on GPP and NPP

Differences in the mean local overpass time (MLT) of Terra and Aqua lead to differences in the quality of MODIS MOD15A2H and MYD15A2H fPAR and LAI retrievals, which are inputs to the MOD17 products, due to greater cloud cover over humid regions in the afternoon. The MLT drift is expected to have negligible impact on the quality of the MOD17 products, as the associated influence on the upstream fPAR and LAI inputs to the model will be minimized through ongoing calibration adjustments to these products. The expected orbital drift toward earlier MLT sampling from Terra may also improve the quality of fPAR and LAI (and therefore MOD17) retrievals over the tropical latitudes, owing to reductions in cloud contamination and spectral data loss from earlier local daily observations that are further from the characteristic mid-day peak in cloudiness.

4.9. Global Water Reservoir (GWR)

Primary authors: Shuai Zhang, Deep Shah, and Huilin Gao. The relevant MODIS products are MxD28. The relevant VIIRS products are Vxx28.

4.9.1. MODIS GWR products

Reservoirs play a crucial role in hydrological cycles and water resources management (Li et al., 2023b). According to global statistics, reservoirs provide roughly 40% of the water needed for irrigation (Biemans et al., 2011) and generate over 60% of renewable energy through hydroelectric power (Murdock et al., 2019). Reservoir evaporation, although invisible, accounts for a significant portion of the water loss and continues to increase under warming climate (Friedrich et al., 2018; Zhao et al., 2022). However, in-situ observations of reservoir water budget terms are often scarce and/or not shared at a global scale (Zhang et al., 2014). To fill in this critical data gap, NASA's MODIS Global Water Reservoir (GWR) product suite (MOD28 from Terra and MYD28 from Aqua) uses the moderate-resolution satellite data for monitoring of global reservoirs. MxD28 offers 8-day and monthly assessments of area, elevation, and storage along with monthly evaporation rates and evaporated volume losses for 151 manmade reservoirs and 13 regulated natural lakes.

4.9.2. VIIRS GWR products

NASA's VIIRS GWR product is generated with essentially the same algorithm that produces the MODIS reservoir products, except for a few

improvements that reduce the large uncertainties under specific conditions, which mainly include: (1) removing misclassified water pixels caused by terrain shadow effects (Leidman et al., 2021); (2) improving the enhancement algorithm using an edge detection approach developed by (Zhao et al., 2020); and (3) adopting snow/ice cover fractions for quantifying evaporation volume. In addition, quality assurance (QA) information is added to help users understand and make the best use of the product.

The VIIRS products are presented at two temporal resolutions as well: 8-day (VNP28C2 and VJ128C2 from SNPP and NOAA-20, respectively) and monthly (VNP28C3 and VJ128C3). The surface area, elevation, and storage values are available at both 8-day and monthly cadences, while the evaporation rate and volume are only available at monthly intervals.

4.9.3. Algorithm for data product continuity

The key algorithms used for generating MODIS and VIIRS water reservoir products are described in Li et al. (2021). The process starts with estimating the 8-day water surface area using an enhanced image classification algorithm to minimize errors associated with clouds/snow/ice contaminations. The estimated area values are then linked to the Area-Elevation (A-E) relationship, obtained from the Global Reservoir Bathymetry Dataset (GRBD) by (Li et al., 2020), to calculate the corresponding 8-day elevation and storage values.

The monthly water reservoir area is calculated by combining the 8-day area classifications, which are then used to infer the monthly elevation and storage. The monthly evaporation rates are estimated using the Lake Temperature and Evaporation Model (LTEM; Zhao et al., 2020), which incorporates MODIS/VIIRS Land Surface Temperature (LST) data (MxD11A2/Vxx21A2) and meteorological information from the Global Land Data Assimilation System (GLDAS). The monthly evaporative volume loss is the product of the evaporation rate and surface area.

4.9.4. Evidence of continuity between MODIS and VIIRS GWR products

Fig. 32 shows that the 8-day VIIRS-based area values agreed well with those of MODIS (Fig. 32a and b), with R^2 values of 0.99 for both VNP and VJ1. The Relative Bias (RB) values for VJ1 and VNP were − 5.54% and − 5.74%, respectively. The smaller water area estimation from VIIRS was primarily attributed to the implementation of the terrain shadow mask. This mask significantly reduced the misclassification of inland pixels covered by terrain shadows in the MODIS based reservoir areas, particularly for lakes located in mountainous and high-latitude regions. The monthly storage values (generated from the monthly area composites) also exhibited a high consistency, with RBs of −11.07% and − 11.49% and R^2 values of 0.96 for both VJ1 and VNP (Fig. 32c and d). The R^2 values between the MODIS and VIIRS-based monthly evaporation rates were 0.89 for VJ1 and 0.90 for VNP (Fig. 32 e&f). The RB for VJ1 was slightly worse (−5.53%) than that for VNP (−2.84%).

4.9.5. Validation of quality of GWR continuity product

We evaluated the monthly MODIS and VIIRS based elevation and storage from 2012 to 2021 against the in-situ data at twelve Indian reservoirs. The elevation estimations from MODIS had a strong correlation with in-situ data, with an average R^2 of 0.82, an average RMSE of 2.57 m, and an average NRMSE of 13.74%. Similarly, VIIRS based elevation estimates also exhibited substantial consistency against the in-situ data, with an average R^2 of 0.75, an average RMSE of 2.59 m, and an average NRMSE of 14.25%. The storage validations for MODIS showed similar patterns as the elevation results, with an average R^2 of 0.87, an average RMSE of 0.59 km^3, and an average NRMSE of 18.49%. Likewise, VIIRS based storage was in good agreement with the in-situ storage observations, with an average R^2 value of 0.80, an average RMSE value of 0.50 km^3, and an average NRMSE value of 17.54% (unpublished results).

In terms of evaporation rate, the MODIS evaporation rates matched well with the Eddy Covariance (EC) observations at Lake Mead from January 2012 to April 2015, with R^2 values of 0.75 and an NRMSE of 19.26%. Similarly, we compared the accuracy of the VIIRS evaporation rate with EC observations at Lake Mead from January 2012 to April 2015. The results indicate that the VNP28C3 evaporation rates had similar accuracy as MYD28C3, with a R^2 value 0.75 and a lower NRMSE value of 18.7%. The minor difference between the MODIS and VIIRS evaporation rates was mainly attributed to differences in the land surface temperature data. However, it has been reported that MODIS and VIIRS LST data have high agreement (>0.99) (Liu et al., 2015), which suggests that VIIRS-based evaporation rate values for other reservoirs should be reliable and consistent with MODIS-based values.

4.9.6. Potential impacts of Terra/Aqua MODIS drifting orbits on GWR

The water reservoir area, elevation, and storage product will not be impacted by the drifting orbits of MODIS. This is because the 8-day/monthly lake water surface area, which is used to calculate elevation and storage, is insensitive to changes in the MODIS overpass time. The drifting orbits may have a potential impact on the reservoir evaporation rate, because the heat storage term requires the water surface temperature (e.g., MxD11A2) as one of the inputs. However, we anticipate that this change will not greatly affect the evaporation results. In our algorithm, the daily water temperature is calculated by averaging temperature values from daytime and nighttime observations. The drifting orbits tend to affect the MODIS water temperature measurements during daytime and nighttime differently, with one increasing while the other is decreasing. Thus, the impact of the drifting orbits on the evaporation estimation will be limited.

4.10. MODIS and VIIRS NASA standard snow cover products

Primary authors: George Riggs and Dorothy Hall. The relevant MODIS products are MxD10A1. The relevant VIIRS product is VNP10A1.

4.10.1. Introduction

Snow cover extent (SCE) is an Essential Climate Variable (GCOS, 2022) needed to address science questions and Earth science applications objectives, including those concerning societal needs (Board and National Academies of Sciences, Engineering, and Medicine, 2019). The NASA standard MODIS and VIIRS snow cover products are produced as a series from the sensor swath Level-2 (L2) to daily gridded and projected Level-3 (L3) snow maps; they provide daily global maps of SCE. The same series of snow cover products is produced for Terra and Aqua MODIS and for SNPP and NOAA-20 VIIRS. The spatial resolutions of MODIS and VIIRS snow cover products are 500 m and 375 m, respectively (Justice et al., 2013; Román et al., 2017). The MODIS and VIIRS snow cover products are available from the National Snow and Ice Data Center (NSIDC) Distributed Active Archive Center (DAAC). The continuity of SCE among the L3 Aqua MODIS MYD10A1, SNPP VNP10A1, and NOAA-20 VIIRS products is considered in this section.

4.10.2. Snow cover products

The MODIS and VIIRS snow cover products are produced using the same algorithms and input products, as well as similar instrument bands, with the intention of creating continuity. By ensuring continuity for the snow cover products, a Climate Data Record (CDR) of moderate-resolution global SCE can be created when approximately 30 years of data become available.

The basis for snow-cover mapping using MODIS and VIIRS data is the Normalized Difference Snow Index (NDSI), which provides an interpreted measure of the fraction of snow cover in each pixel, ranging from 0 (no snow cover) to 1.0 (complete snow cover). In addition, a series of data screens designed to alleviate errors and flag uncertain snow cover detections is an integral part of the algorithm. The snow cover detection algorithm is applied in the L2 processing. The L3 data products are projected and gridded from L2 to the sinusoidal projection. A single

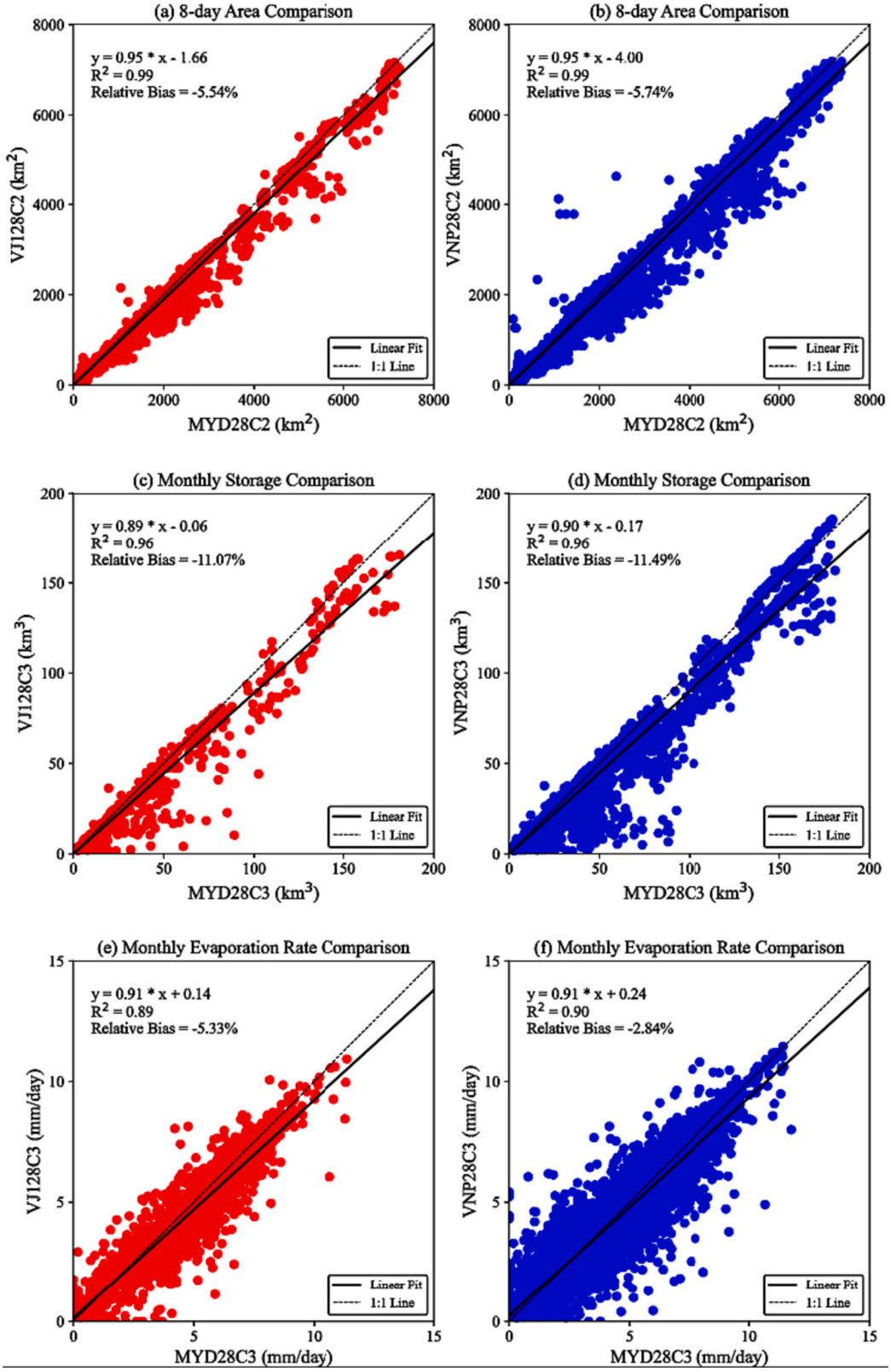

Fig. 32. The comparison of surface area, reservoir storage, and evaporation rate between MODIS Aqua (MYD), Suomi-NPP (VNP) and NOAA-20 (VJ1) at 8-day and monthly temporal intervals. Lake Baikal was excluded from the figure and analysis due to its extreme large values. (For interpretation of the references to colour in this figure legend, the reader is referred to the web version of this article.)

daily observation is selected from overlapping observations. The MODIS and VIIRS snow cover products and algorithms are described in detail in the product user guides (Riggs et al., 2019a, 2019b; Riggs and Hall, 2019).

4.10.3. Evidence of continuity between the MODIS and VIIRS snow cover products

Continuity of SCE between MODIS Aqua MYD10A1 and SNPP VIIRS VNP10A1 snow cover products was evaluated in Hall et al. (2019) and Riggs and Hall (2020). In Riggs and Hall (2020), MYD10A1 and VNP10A1 continuity was investigated by cross-comparison of NDSI Snow Cover data and comparison of binary snow cover maps derived from the NDSI Snow Cover data. Cell-to-cell cross-comparisons of the NDSI Snow Cover data values found a wide range and distribution in NDSI values in bivariate histograms between MYD10A1 and VNP10A1, as expected (Riggs and Hall, 2020). The NDSI values are expected to vary between Aqua and SNPP at the pixel-level due to many convolved factors, including differences in viewing angles, local time, scan angle, pixel spread, and others. Those convolved factors affect cross-comparisons of the NDSI and other ratio-based variables such as of MODIS and VIIRS NDVI (Skakun et al., 2018; Vargas et al., 2013), enhanced vegetation products (Moon et al., 2019), and vegetation indices (Miura et al., 2018). These effects can be reduced by using a coarser spatial resolution (e.g., the climate modeling grid (CMG) scale of ~5 km) for comparisons. Those convolved factors can also be mitigated by deriving binary snow cover maps from the MODIS and VIIRS snow cover products, and then comparing the binary snow cover maps to evaluate continuity in SCE between the products (e.g., see Riggs and Hall, 2020; Hall et al., 2019; Thapa et al., 2019; Zhang et al., 2020a, 2020b).

A 1 km resolution CMG grid covering the western United States (consisting of six tiles of the daily tiled products) was created, and the MYD10A1 and VNP10A1 binary snow cover observations were mapped to that grid and compared by Riggs and Hall (2020). The SCE derived from the MYD10A1 and VNP10A1 CMG snow maps was found to agree within ~95% of SCE, spatially and temporally. Differences in SCE were attributable to differences in the Aqua and SNPP cloud masking and to differences in sensor resolutions.

Product continuity was also investigated by comparing SCE in the cloud-gap-filled (CGF) MODIS MYD10A1F and VIIRS VNP10A1F products by Hall et al. (2019). A nearly 3 month time-series comparison of Terra and Aqua MODIS and SNPP VIIRS CGF snow-cover maps was

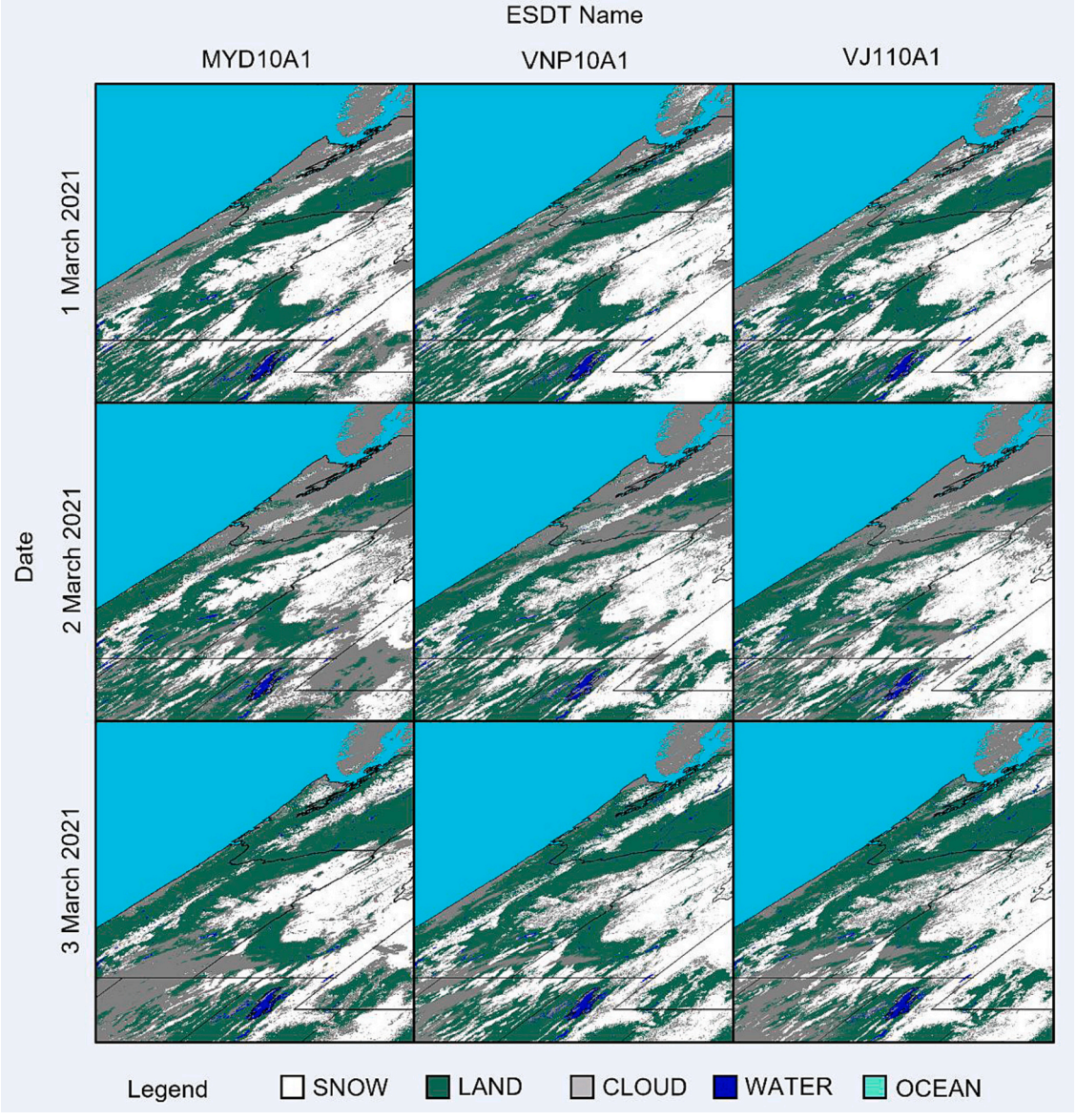

Fig. 33. Binary SCE maps from MYD10A1F, VNP10A1F, and VJ110A1 for 1–3 March 2021 for tile h09v04 covering the northwestern USA.

conducted for a large study area, covering all or parts of 11 states in the western US and part of southwestern Canada. Results revealed excellent correspondence between the Terra MODIS and SNPP VIIRS products for 99.6% of the study area (Hall et al., 2019). Accuracy was evaluated by comparing the CGF-derived snow maps with surface reflectance maps, higher-resolution maps such as those derived from Landsat and Sentinel, and other satellite-derived snow maps (e.g., the NOAA Interactive Multisensor Snow and Ice Mapping System (IMS) maps). Although the Terra MODIS and VIIRS SCE maps showed excellent correspondence, the VIIRS maps showed slightly more snow cover on average than did the Terra MODIS maps on a given day, which was largely attributable to differences in the product cloud masking.

Continuity among the MYD10A1, VNP10A1, and VJ110A1 SCE products was demonstrated by comparing binary SCE maps of each product for a single tile covering the northwestern United States for 1–11 March 2021. Binary SCE maps of the three products for 1–3 March 2021, a period with minimal cloud cover, are shown in Fig. 33.

SCE was spatially consistent among the MYD10A1, VNP10A1 and VJ110A1 products (Fig. 33). SCE was calculated for all products by counting the number of snow-covered grid cells, and then multiplying this number by the area of the grid cell (0.21 km^2 for MODIS and 0.14 km^2 for VIIRS). Similar calculations were made for cloud-cover extent in each product. The SCE and cloud extent areas were then calculated as a percentage of total land in the tile. The percentage areas of SCE, and cloud-cover extent of the products for 1–11 March 2021 are plotted in Fig. 34.

SCE was very similar between the VIIRS products, VNP10A1 and VJ110A1 (Fig. 33). The Aqua MODIS MYD10A1 SCE was consistently less than VIIRS, yet it tracked very closely with the VIIRS SCE daily observations, varying from 4 to 10% depending on the day. The Aqua MODIS cloud cover extent was consistently greater than the VIIRS cloud extent on a daily basis (Fig. 34). In this time series, MYD10A1 showed 2–14% more cloud cover than do the VIIRS products. The observed consistency of SCE among the products suggests that the products have potential to be combined to build a long term multi sensor data record of SCE.

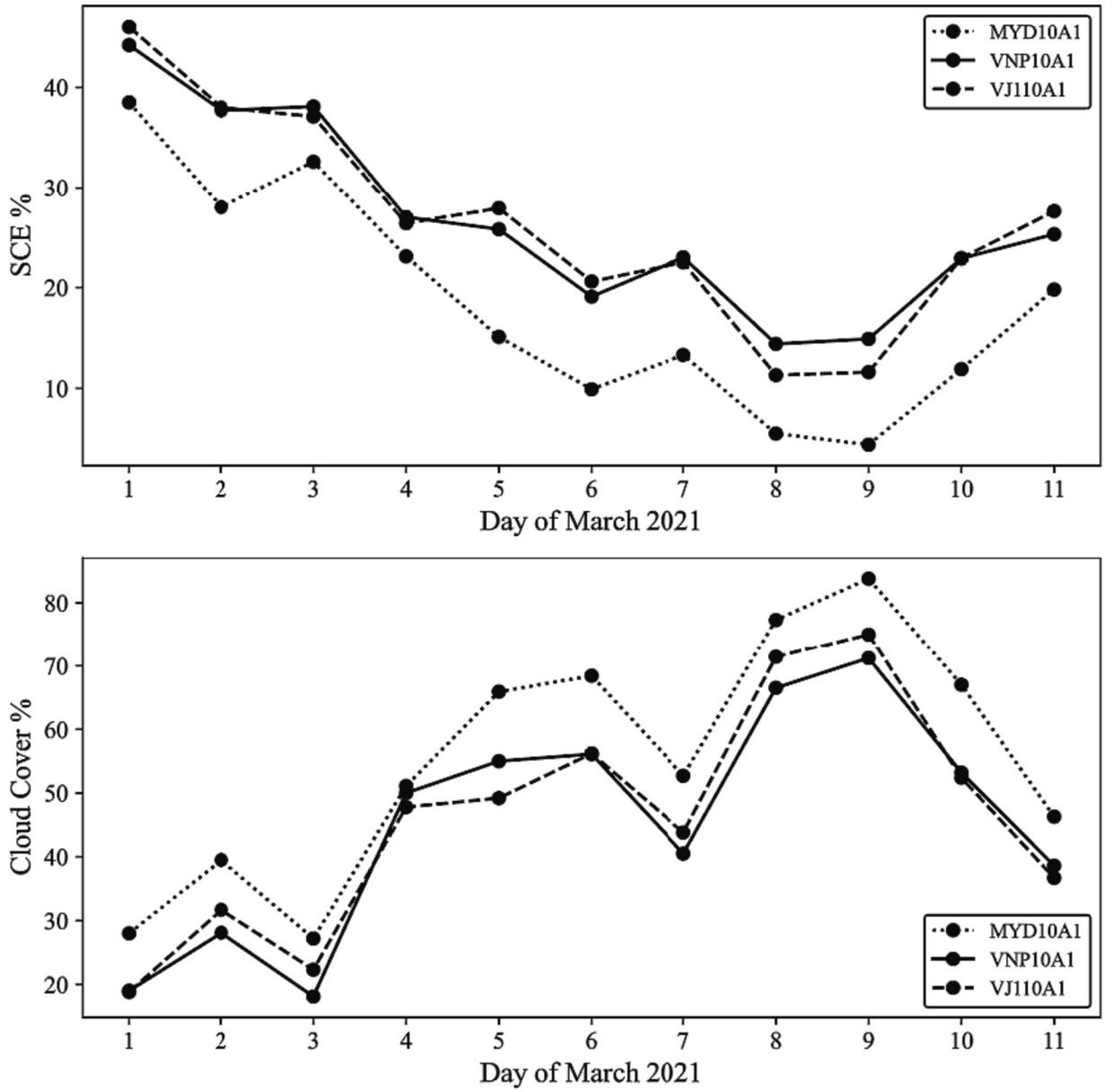

Fig. 34. Comparison of SCE and cloud cover extent of the MYD10A1, VNP10A1 and VJ110A1 data products, 1–11 March 2021. The percentage of SCE and cloud cover is based on total land area in tile h09v04.

4.10.4. Validation of quality of snow cover continuity products

The snow cover data products were validated based on the Committee on Earth Observation Satellites validation stages 0–4 (VIIRS Land, 2022b). The MODIS snow cover products have been validated to Stage 2 (MODIS Land, 2023b) and the VIIRS snow cover product has been validated to Stage 1 (VIIRS Land, 2022c). Validation case studies summarized on the VIIRS Land website (VIIRS Land, 2022c) report 97% agreement between MODIS and VIIRS SCE. The validation stage of products is expected to remain consistent if the instruments remain well calibrated, because the algorithms are mature.

Quantitative comparisons of MODIS and VIIRS snow cover products are limited. Thapa et al. (2019) made quantitative and qualitative comparisons between the MODIS Aqua swath snow cover product MYD10_L2 and the NOAA VIIRS swath binary snow cover product for the 2016 hydrologic year within a study area of central and western Canada and the U. S. Midwest. They reported an overall agreement of 97% between Aqua MODIS and VIIRS SCE.

MODIS Terra, and Aqua, and VIIRS snow cover products were compared for accuracy of mapping snow cover in China and Tibetan Plateau by Zhang et al. (2020a, 2020b). The accuracy of the snow cover maps was assessed with ground station snow-depth data. Overall, they found "substantial" agreement among the snow maps. A critical factor in their intercomparisons was selection of the NDSI threshold to produce a binary snow map for each product for the purpose of comparing the products. Additionally, Tong et al. (2020) reported that MODIS Terra and Aqua snow cover products were approximately 97% accurate when validated with snow-depth measurements in Austria over the period 2002–2014.

4.10.5. Status and maturity of snow cover products and algorithms

The MODIS snow cover products are often used as a standard for comparison with other snow maps. The NDSI has been shown to be a robust, accurate methodology for snow cover mapping (see Hall and Riggs, 2007). The MODIS snow cover products have been reprocessed several times since production began in 2000, with the most current collection being C61 (Riggs et al., 2019a, 2019b). With each reprocessing, more quality assurance data was added, and the content and format of the data products was changed. The SNPP and JPSS1 VIIRS snow cover products are currently being reprocessed and forward processed in C2. The SNPP VIIRS snow cover products are available beginning in January 2012, and the NOAA-20 products are available beginning in January 2018. Within each collection, the product quality is consistent.

4.10.6. Potential impacts of Terra/Aqua MODIS drifting orbits on snow cover products

Drifting orbits of the Terra and Aqua spacecraft are likely to influence the ability of the MODIS and VIIRS algorithms to detect snow cover. As mean local crossing times (MLT) drift earlier for Terra or later for Aqua, the lower solar zenith angle will likely result in lower top-of-atmosphere reflectance, which is the most important factor for snow cover detection. Lower solar zenith angles also increase shadows on the landscape, which may lower reflectance below the thresholds needed for snow cover detection. The impact of orbit drift on reflectance from the surface is not easily quantified. Analysis of NASA Scientific Visualization Studio animations of the Terra deorbit MLT drift suggests that at about two hours of drift, which is expected to occur sometime around late 2025 (NASA, 2021), there are likely to be notable impacts on the algorithm due primarily to landscape shadows. Coverage will probably decrease in boreal regions, varying seasonally with the tilt of the Earth.

4.11. Burned area

Primary author: Louis Giglio. The relevant MODIS product is MCD64A1. The relevant VIIRS products are Vxx64A1.

4.11.1. MODIS burned area product

Burned area is an Essential Climate Variable (GCOS, 2022) mapped in the MODIS MCD64A1 global monthly burned area product. The product reports the date of burn to the nearest day on a monthly basis at 500 m spatial resolution. The MCD64A1 data record spans more than two decades, from November 2000 to present.

4.11.2. VIIRS burned area product

NASA's VIIRS burned area product (VNP64A1) is generated using the MODIS Collection 6.1 MCD64A1 burned-area mapping algorithm with minor adjustments focused on product consistency and continuity. As with its MODIS predecessor, the VNP64A1 product reports the date of burn on a monthly basis at 500 m spatial resolution. Unlike the MODIS burned area product, which is produced from both morning (Terra) and afternoon (Aqua) surface reflectance and active-fire observation, the Collection 2 VNP64A1 burned area product is derived solely from afternoon SNPP (and optionally NOAA-20) observations.

4.11.3. Algorithm for data product continuity

The MODIS and VIIRS burned-area product mapping approach employs 500 m MODIS or 750 m VIIRS surface reflectance imagery coupled with 1 km MODIS or 750 m VIIRS active fire observations. In this approach, dynamic thresholds are applied to composites that are generated from a burn-sensitive spectral index derived from short-wave infrared observations, and a measure of temporal texture derived from the day of maximum change in the local surface reflectance time series. Cumulative active fire maps guide the selection of burned and unburned training samples and the specification of prior probabilities for use in a Bayesian model that evaluates the *burned/unburned* posterior odds ratio at each location. This combined use of active-fire and reflectance data enables the algorithm to adapt regionally over a wide range of pre- and post-burn conditions. Details of the mapping algorithm are available in Giglio et al. (2009, 2018).

4.11.4. Evidence of continuity between MODIS and VIIRS burned area products

In most regions the Collection 6.1 MODIS and Collection 2 VIIRS burned-area products were highly consistent (Fig. 35, left panel). However, the products were less consistent in some agricultural areas (Fig. 35, right panel), at least in part due to the lack of a morning VIIRS overpass. An exhaustive analysis of the product discrepancies and their root causes is underway, with findings expected soon after the forthcoming Collection 2 VNP64A1 product release.

4.11.5. Validation of quality of continuity product

When completed, the Collection 2 VNP64A1 product will be validated at the CEOS Stage 3 level using the dataset of Landsat 8 burned-area reference maps used to validate the Collection 6 MCD64A1 product (Boschetti et al., 2019). Those reference images were selected using a stratified random sampling approach that allowed for probability sampling in both space and time (Boschetti et al., 2016).

4.11.6. Status and maturity of the burned area product and algorithm

MCD64A1 has been validated at the CEOS Stage 3 and Stage 4 levels using thousands of high-resolution reference images (Boschetti et al., 2019; Padilla et al., 2018). For some applications the Collection 2 VIIRS VNP64A1 burned-area product may safely be used as a direct replacement for the MODIS MCD64A1 product. However, for other applications, such as cropland fire assessments, the VIIRS and MODIS burned products will likely be too inconsistent to intermix. Detailed guidance will be issued following the exhaustive product quality assessment and validation that will in turn commence with the imminent "tier-2" Collection-2 reprocessing.

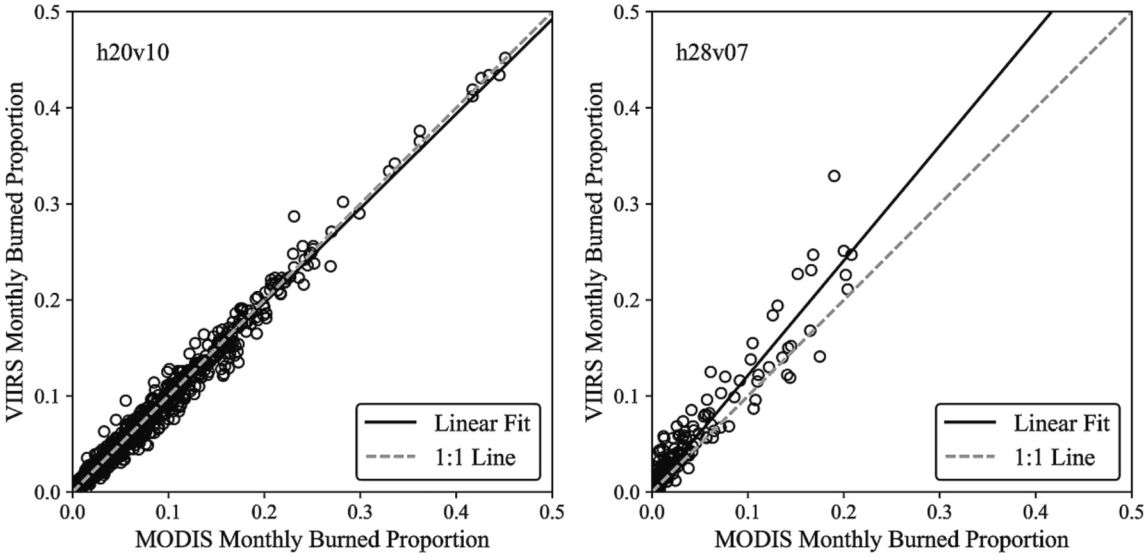

Fig. 35. Scatter plots of the monthly proportions of coarse resolution ~120 × 120 km cells labeled as burned in the Collection 2 VIIRS VNP64A1 burned area product, plotted against the corresponding proportion labeled as burned in the Collection 6.1 MODIS burned area product over a 31-month test period (July 2018 – Feb. 2020 + Feb. 2021 – Dec. 2021). Plots are for MODIS tiles located in southern Africa (h20v10; left panel) and southeast Asia (h28v07; right panel) and are representative of product consistency in savanna/non-agricultural (Pearson's $r = 0.994$) and agricultural ($r = 0.963$) regions, respectively. Solid black lines show the ordinary least squares regression lines; dashed gray 1-to-1 lines are included for reference.

4.11.7. Potential impacts of Terra/Aqua MODIS drifting orbits on burned area

Production of a high-quality MODIS burned-area product is expected to continue as the orbits of Terra and Aqua drift, since the changes in sensor footprint and diurnal sampling as a result of the orbital drift will not be drastic.

4.12. Black Marble Nighttime Lights (NTL)

Primary author: Zhuosen Wang. The relevant VIIRS products are Vxx46Ax.

4.12.1. Black Marble as a benefit of using VIIRS products to achieve MODIS product continuity

VIIRS also provides the Black Marble NTL products, which are an additional source of context and information for studies using other VIIRS products. NASA's Black Marble NTL products have been increasingly used for quantitative analysis of human activity and human behavior dynamics with reduced noise uncertainties, supporting the United Nations Sustainable Development Goals (SDGs) (Chakraborty et al., 2023; Cole et al., 2017; Enenkel et al., 2019; Román et al., 2019; Román and Stokes, 2015).

A long-term consistent daily data record of global NTL is crucial for our understanding of how human activities have changed over time, and in turn, how these changes have altered the planet. While the intra-day observations from Black Marble are not a replacement for the loss of the Terra AM overpass, the possibilities for new insights from the availability of NTL could be of great value to understanding Earth's systems.

4.12.2. VIIRS Black Marble products

The 15 arc *sec* spatial resolution Collection V001 (C1) global SNPP Black Marble product suite includes: (1) daily Top-of-Atmosphere (TOA) Day/Night Band (DNB) NTL radiance (VNP46A1); (2) daily atmospheric- and lunar-BRDF-corrected NTL radiance (VNP46A2); and (3) monthly and annual NTL composites (VNP46A3/A4) (Román et al., 2018; Wang et al., 2022). A novel "Turning off the Moon" approach is applied to derive the daily atmospheric- and lunar-BRDF-corrected NTL radiance product. This approach combines cloud-free, atmospheric-, terrain-, snow-, lunar-, and stray light-corrected nighttime VIIRS DNB radiances, daytime DNB surface reflectance, Bidirectional Reflectance Distribution Function (BRDF)/Albedo, and Lunar irradiance values to minimize the influence of extraneous artifacts and biases (Román et al., 2018; Wang et al., 2021b). The monthly and annual composite products are generated for various view angles, as well as snow conditions based on daily VNP46A2, to minimize uncertainties attributed to view geometry and snow cover (Wang et al., 2021b).

4.12.3. VIIRS inter-instrument comparison for Black Marble

An intercomparison was conducted to evaluate the influence of the spectral response functions of SNPP, NOAA-20, and NOAA-21 on DNB retrievals. Fig. 36 shows the relative spectral response (RSR) functions of NOAA-20, NOAA-21, and yearly SNPP. The SNPP DNB RSR on-orbit change (Fig. 36) was mainly due to the degradation of the rotating telescope assembly (RTA) mirrors during early stages of the mission. The DNB RSR change was faster in the first year on orbit, with the peak shifting from NIR toward a "blue" wavelength. NOAA-20 DNB RSR had no visible variation on-orbit.

The DNB onboard SNPP, NOAA-20, and NOAA-21 are calibrated monthly. As a result, the impact of the SNPP DNB RSR change was relatively small for traditional light sources such as Ceramic Metal Halide and High Pressure Sodium (Fig. 37). The mean radiances of C1 and C2 SNPP and NOAA-20 in Dubai were 93.01, 93.88, and 92.05 $nWcm^{-2}\ sr^{-1}$ respectively. The NOAA-20 DNB radiance was 6% lower than SNPP during the period from 2019 to 2022 at the Rome site (Fig. 37). The mean radiances of C1 and C2 SNPP and NOAA-20 were 57.53, 58.07, and 54.49 $nWcm^{-2}\ sr^{-1}$ respectively. The streetlights of the Rome site were transitioned to LED in 2017, which substantially decreased the DNB radiance (Wang et al., 2022). No DNB RSR adjustments were applied among SNPP, NOAA-20, and NOAA-21 in C2 reprocessing, considering the complex spectra of the different light types being observed (Levin et al., 2020).

The Black Marble products' NTL detection limit of 0.5 $nWcm^{-2}\ sr^{-1}$ meets the standard to be classified as "Breakthrough" by the key performance requirements of the mission (Román et al., 2018). Wang et al. (2021b) further quantified the sources of Black Marble NTL uncertainty due to surface BRDF/albedo, view angles, snow cover, lunar irradiance, cloud, aerosol, vegetation, and ephemeral artifacts. The assessment indicated that NTL uncertainty is dominated by angular and

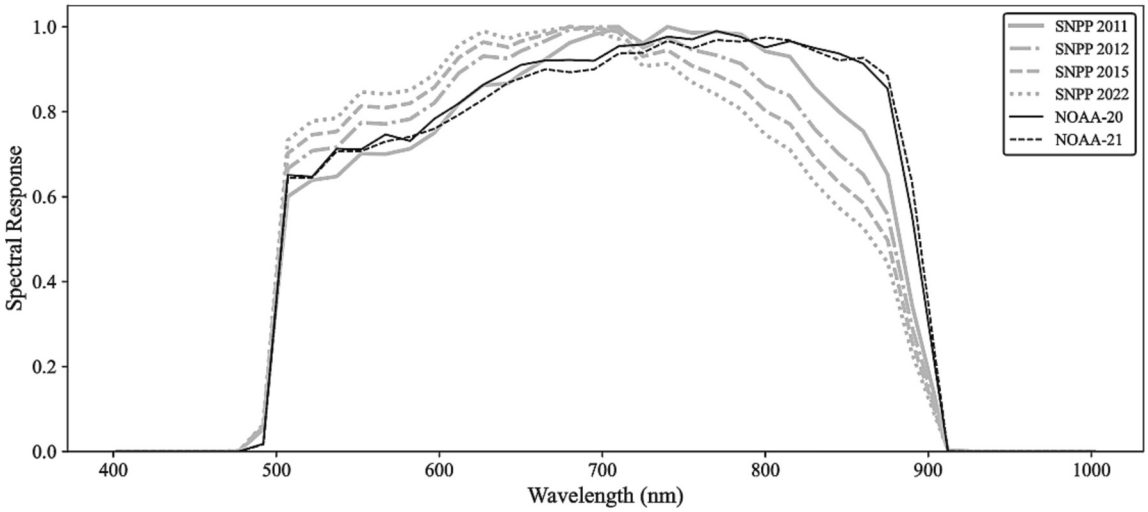

Fig. 36. The Spectral response function of NOAA-20, NOAA-21, and annual SNPP. NOAA-20 and NOAA-21 DNB RSR have no visible variation on-orbit.

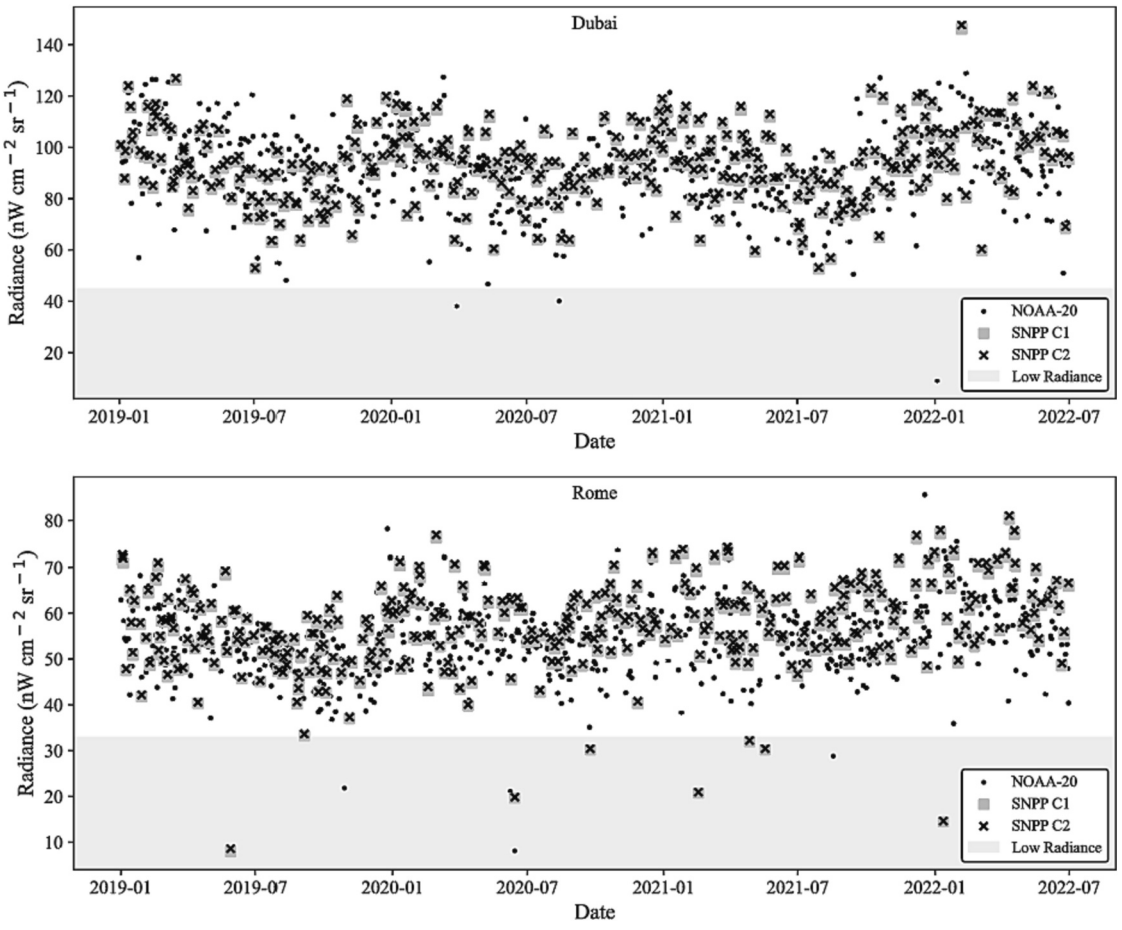

Fig. 37. The Collection 2 SNPP and NOAA-20 nighttime light radiance of one pixel in Dubai (25.06 N, 55.21E) and one pixel in Rome (41.88 N, 12.57E). The mean radiances of C1 and C2 SNPP and NOAA-20 in Dubai were 93.01, 93.88, and 92.05 $nWcm^{-2}\ sr^{-1}$ respectively. The mean radiances of C1 and C2 SNPP and NOAA-20 in Rome were 57.53, 58.07, and 54.49 $nWcm^{-2}\ sr^{-1}$ respectively.

atmospheric effects and is not due to calibration differences among sensors on different platforms.

4.12.4. Status and maturity of Black Marble products

Current Collection 2 (C2) reprocessing efforts focus on refining the Black Marble products with updated calibration LUTs. The aurora mask, identified using a machine learning method, is being added to the daily TOA NTL product (VNP46A1) (Kalb et al., 2023). Also, a new NTL change metrics product (VNP46A5) is being added to the Black Marble product suite (Li et al., 2022b). In addition to Near-Real-Time (NRT) VNP46A1, the C2 reprocessing also implements NRT lunar-BRDF and atmospherically corrected radiance (VNP46A2). Finally, the C2 Black

Marble products are expanding on the SNPP products to also include NOAA-20 and NOAA-21 products, derived with the same retrieval algorithm used in C1.

5. Additional sources for MODIS continuity

As shown above, data from both Terra and Aqua MODIS instruments are used to generate numerous land surface products that are specified as Essential Climate Variables (ECVs) by the global climate observing system (GCOS), including products related to fire, albedo, LAI/FPAR, DSR/PAR, land surface temperature, snow, and ice. With the continuity of data products solely reliant on MODIS Aqua (PM overpass) mostly served by VIIRS, attention can turn to achieving data continuity for the data products reliant on Terra MODIS (AM overpass). Following its final inclination maneuver in March 2020, Terra is currently drifting out of its specified orbit. In September 2022, the Terra-MODIS orbital overpass reached its lower limit (10:15 AM) and started exiting the 705 km AM constellation (Phase F). Assuming that Terra's operations continue to be

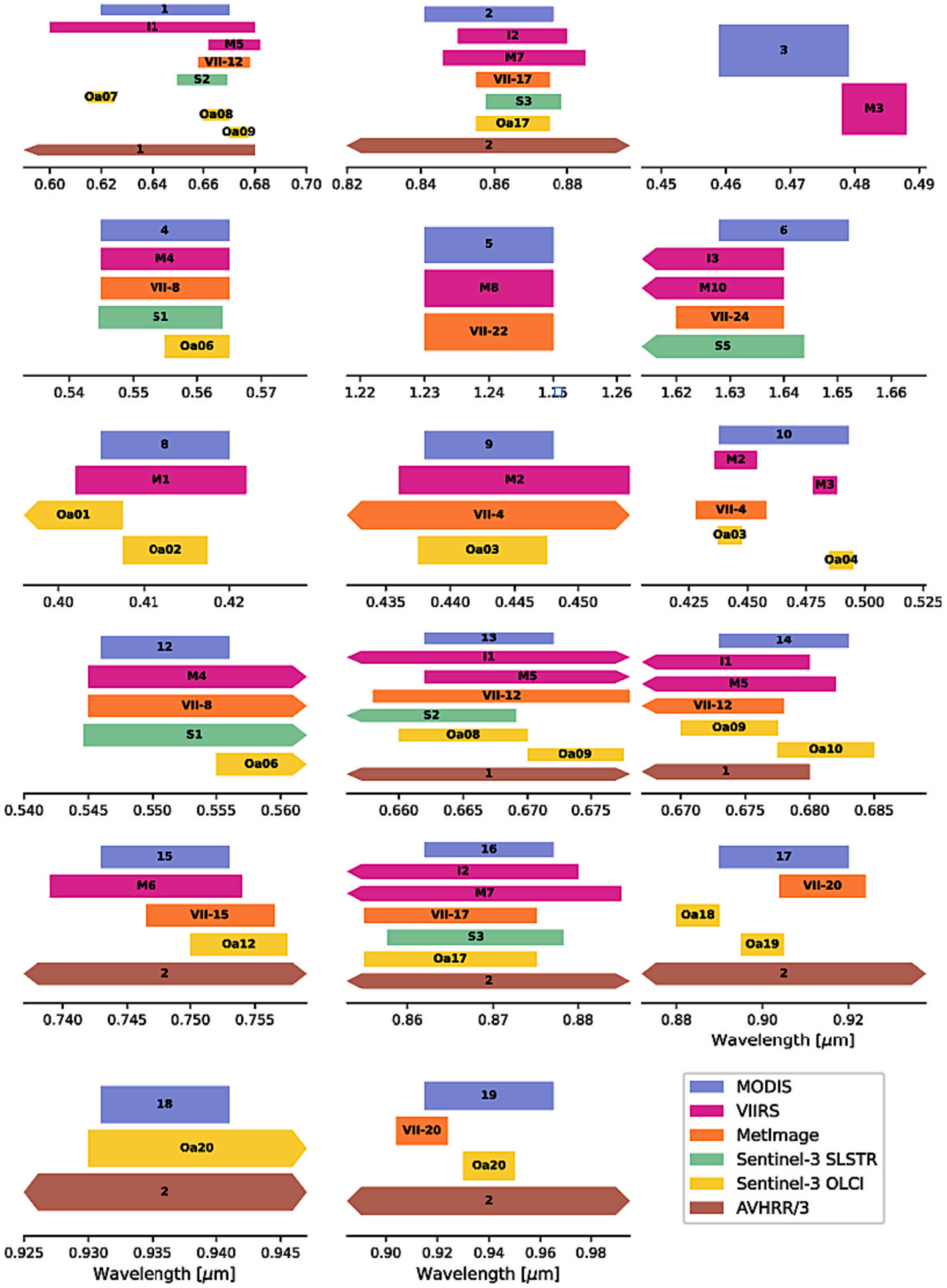

Fig. 38. Spectral overlap of MODIS bands 1–19 with bands of other instruments that are potential sources of continuity. Only MODIS bands with overlap with at least one band from another instrument are shown. Each polygon is labeled with the name of its band. Triangular ends to polygons indicate that spectral range of corresponding band extends beyond the axes of the subplot in the relevant direction.

supported, Terra is estimated to drift to a 9:00 AM overpass in 2026. The recent printed wire assembly failures and the solid-state recorder reset on the Terra platform also bring into focus the aging components and the approaching end of life of the platform.

Given that we currently have three VIIRS satellites in orbit (SNPP, NOAA-20, NOAA-21) with the same PM overpass, an immediate suggestion was to move SNPP into an AM overpass, with the rationale that NOAA and NASA have characterized the SNPP instrument calibration and performance. As shown above, the NASA VIIRS Land Discipline Team is also transitioning the EOS-era algorithms for VIIRS product generation. However, two major constraints, insufficient fuel and lack of time needed to maneuver SNPP into a 10:30 AM orbit, make this a difficult option to execute by the joint program. There are two potential viable solutions which are complementary, and the compatibility of bands from these and other relevant sources can be found in Figs. 38 and 39 and Appendix, Tables A1–A4.

5.1. *Sentinel-3 OLCI/SLSTR*

ESA's Sentinel-3 satellites have two imaging systems: (i) The Ocean

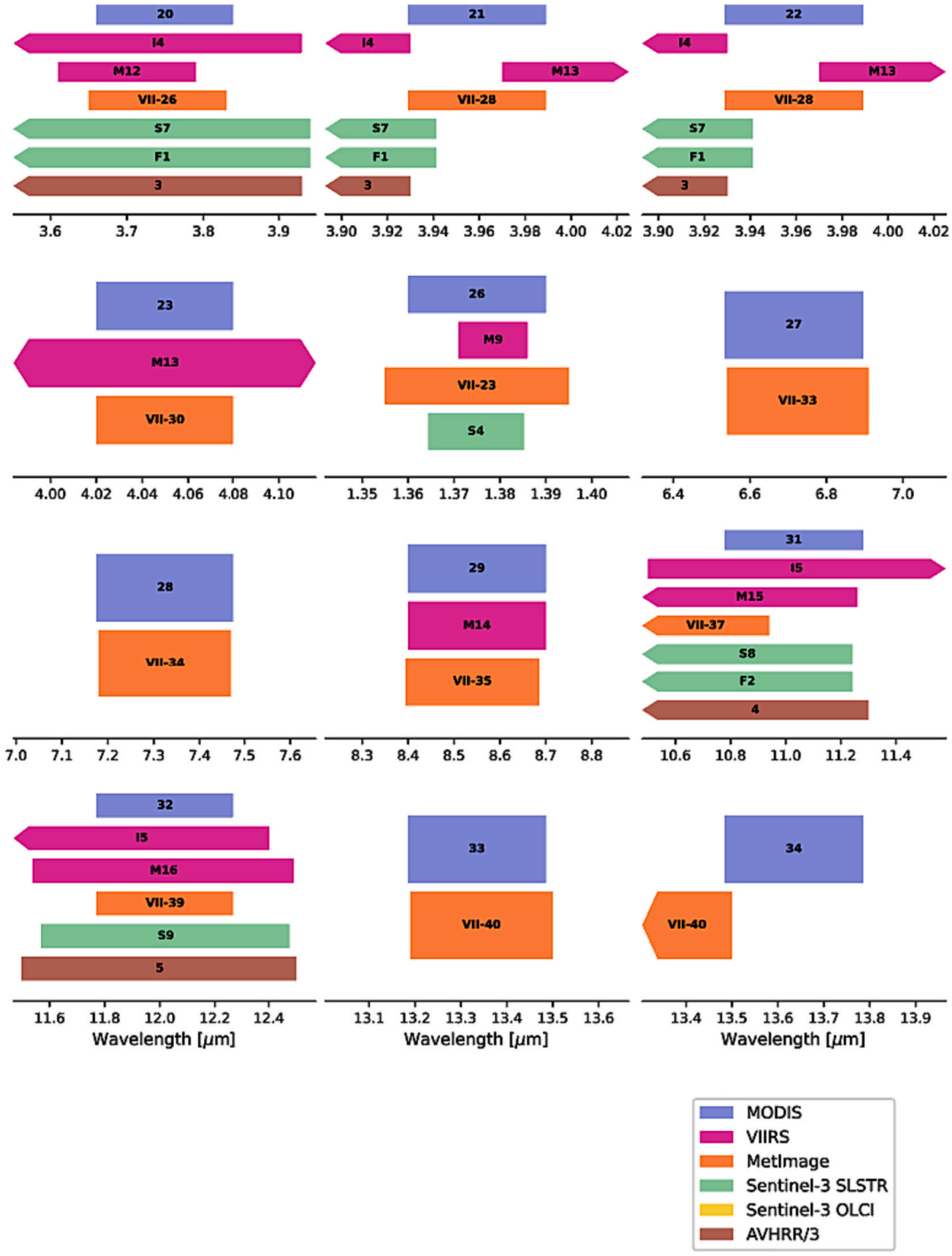

Fig. 39. Spectral overlap of MODIS bands 20–36 with bands of other instruments that are potential sources of continuity. Only MODIS bands with overlap with at least one band from another instrument are shown. Each polygon is labeled with the name of its band. Triangular ends to polygons indicate that spectral range of corresponding band extends beyond the axes of the subplot in the relevant direction.

and Land Colour Instrument (OLCI), which provides 300 m data with 21 bands in the VIS-NIR spectrum, and (ii) the Sea and Land Surface Temperature Radiometer (SLSTR), which has 11 bands at 500 m (VIS, SWIR) and a 1 km mid-long wave IR band, including bands designed for fire detection and characterization and Land Surface Temperature (LST) generation (See Appendix, Tables A2 and A3). Neither Sentinel-3 OLCI or SLSTR carry the VIIRS day/night band. Launched in 2016, Sentinel-3 has a substantial overlap with MODIS Terra allowing for product intercomparison. When combined, ESA's OLCI/SLSTR can provide a reliable land data stream equivalent to Terra-MODIS for the land community. Sentinel-3A (launched 2016) and 3B (launched 2018) have a 10:00 AM overpass. The follow-on Sentinel-3C and 3D are due for launch in 2024 and 2025 respectively, with observations planned through 2031.

NASA has already secured a data feed from Sentinel-3 and within the framework of the CEOS Working Group on Cal/Val, NASA has worked with ESA-supported scientists on atmospheric correction of the ESA-provisioned OLCI/SLSTR Synergy data through the ACIX initiative. NASA supported Eric Vermote to undertake an evaluation of Sentinel-3 for land applications and analysis, which showed the official ESA Synergy Surface Reflectance product performance to be mediocre based on an inter-comparison with MODIS Terra over a period of several months in 2018, 2019, 2020. The error was about twice the specification whereas MODIS error is about half the specification. These results were presented at the 6th Sentinel-3 Validation Team meeting in December 2020. However, a simple prototype MODIS-like algorithm applied to the top of the atmosphere Sentinel-3 Synergy reflectance showed performance better than specification could be achieved (Fig. 40). Sentinel-3 has the spectral potential to accommodate the complete MODIS (LaSRC) surface reflectance retrieval algorithm that has already been ported with success to the VIIRS, Sentinel-2 MSI, and Landsat 8 OLI instruments, reaching the advanced MODIS Collection V6.1 surface reflectance performance level. This work should be brought to completion, and a sample of merged land products should be made available for downstream product testing and intercomparison.

5.2. MetOp-SG METImage

When the Integrated Program Office (IPO) began planning and execution of the NPOESS program, budget constraints led to agreements with European partners to ensure continuity of the operational early morning portion. The current imager on MetOp-C is AVHRR/3, which does not provide continuity with MODIS. MetOp-C will be replaced in 2025 by the second generation MetOp (MetOp-SG), which will include METImage, a VIIRS-like instrument that initially conceptualized as the Visible Infrared Imager (VII). METImage has 20 bands at 500 m spatial resolution with a swath width of +/− 54 degrees (c. 2670 km). The MetOp-SG series is planned for operation from 2025 to 2039 with a 9:30 AM overpass. The operational designation of METImage ensures data continuity. It also provides an opportunity for NASA to enrich its global suite of early-morning land science products beyond a single crossing time. Combined AM (9:30–10:30) observations are akin to MODIS Terra/Aqua Combined products and offer new opportunities to characterize key land surface processes (e.g., surface energy balance, early fire detection, and snow melt.) A comparison of MODIS, VIIRS, OLCI, SLSTR and METImage band characteristics is shown in Appendix, Tables A1–A4. Although limited, simulated METImage test data are currently available from the German Aerospace Center (DLR). Though it should also be noted that METImage (i) will not include the VIIRS Day/Night Band; (ii) does not include the VIIRS (412 nm) blue band, which is used for atmospheric correction; (iii) has a lower saturation than VIIRS for the 3740 nm band, which will impact fire detection; and (iv) does not aggregate pixels across the scan like VIIRS. These constrains should inform future priorities concerning data continuity of Earth System Data Records produced by NASA and its partner agencies, including priorities of the current and future designated observables under the US Earth Science Decadal Survey.

For METImage to provide dynamic data and product continuity, NASA will need to secure a feed of Level 1B data (raw data records) and to invest in sufficient instrument calibration/characterization (both radiometric and geolocation) as well as product validation

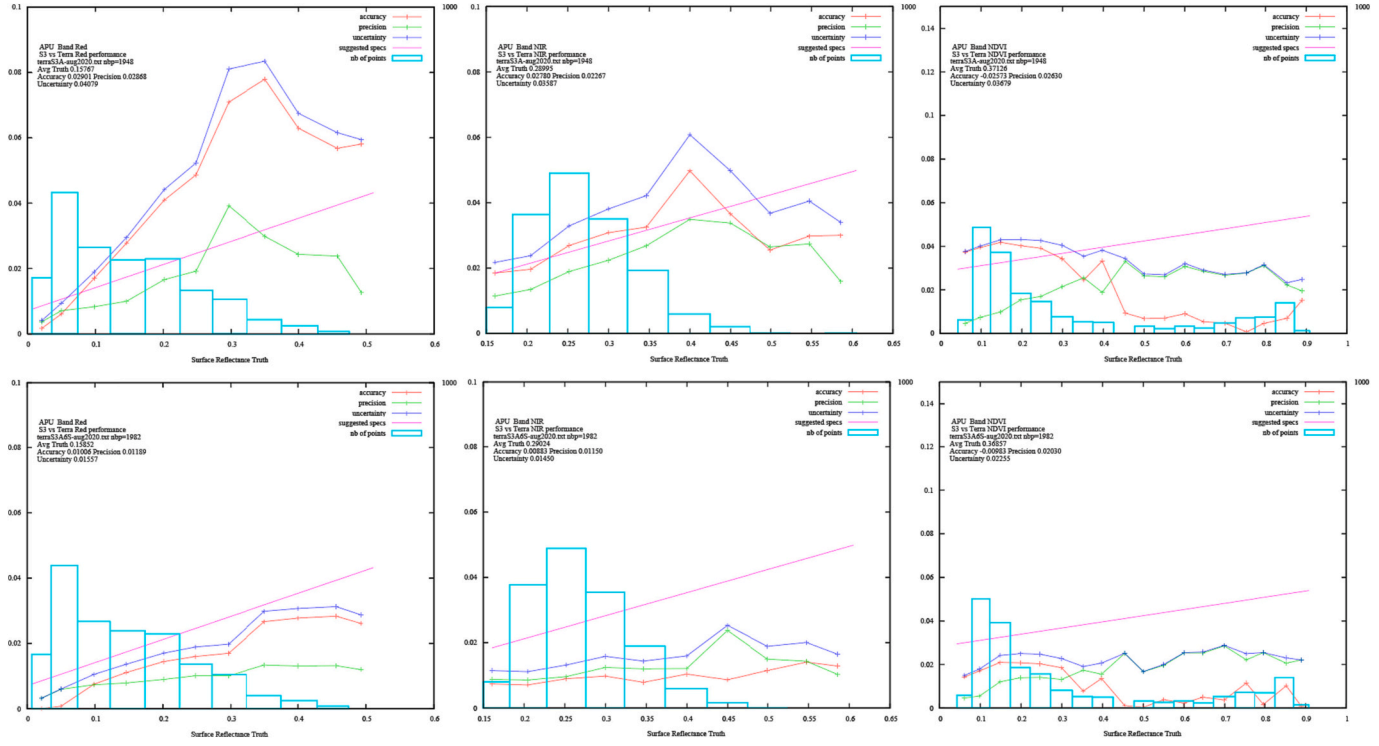

Fig. 40. Accuracy, Precision, and Uncertainty metrics comparing the performance of Sentinel-3 Surface Reflectance against Terra-AM MODIS Surface Reflectance using (top) ESA-algorithm and (bottom) NASA-algorithm for August 2020.

infrastructure to support the science. These steps will require careful coordination of cooperative activities with agencies that share similar interests. For instance, there are plans by EUMETSAT and NOAA to place METImage 'pass-through' Level 1B data in the Cloud and develop different product categories (EDRs/CDRs). Similarly, NASA's MODIS/VIIRS algorithms and products will need to be adapted and tested for differences in overpass time, spectral and spatial resolution and the continuity with MODIS and compatibility with VIIRS evaluated. Standardized intercomparison and validation, under the framework of the CEOS Working Group on Cal/Val, will also ensure the continued long-term confidence in the accuracy and quality of these products as championed by NASA during the EOS era.

The MODIS Aqua instrument has a similar afternoon overpass to VIIRS and there is continuity of pm observations. However, some of the land products are limited by the lack of morning observations. For the Terra observations, with an AM overpass, there is no NASA replacement instrument. The suitability of the morning European Sentinel 3 is being evaluated and the future METImage system may provide an additional continuity option.

6. Conclusion

This paper summarizes NASA-funded research to transition the MODIS Land data product to the VIIRS instruments. The above sections show that for many of the land products the VIIRS instrument provides suitable continuity in observations. To achieve this continuity, a significant effort has been put into instrument cross-calibration, and as a result, successive improvements have been made to the VIIRS Level 1 data processing. Similar to MODIS, the VIIRS land products are being improved, and the data from VIIRS are being reprocessed to the current, most up-to-date version, Collection 2 (C2).

Continuity of MODIS data on a product-by-product basis provides an excellent foundation for practitioners in the wider Earth observation science community, beyond the NASA and MODIS science teams and principal investigators, to continue engaging in applications that rely on the MODIS data record. However, many practitioners will still need to take additional steps to persist their applications beyond the end of the MODIS mission, such as performing targeted investigations, measurements, or calibration activities; and constructing new data processing architectures, designing new algorithms, or understanding new technologies. Any one of these externalities and their associated costs could be too much of a burden for practitioners in the wider Earth observation science community to overcome, suggesting that additional resources should be made available specifically for application continuation activities to avoid the loss of important applications. In addition to the provision of material resources, one of the most effective ways to support the community in continuing valuable applications from MODIS to VIIRS is to provide access to expertise in modern data processing architectures and development operations, as has been a growing strategy for NASA. Overall, it is hoped that the efforts to prepare for the MODIS to VIIRS transition made by the TNSNPP Land Discipline team, and captured in this review, will be of genuine help to the community, and a fitting testament to the long and wonderfully successful MODIS mission.

CRediT authorship contribution statement

Miguel O. Román: Conceptualization, Supervision, Writing – original draft, Writing – review & editing. **Chris Justice:** Conceptualization, Supervision, Writing – original draft, Writing – review & editing. **Ian Paynter:** Writing – original draft, Writing – review & editing. **Peter B. Boucher:** Writing – original draft, Writing – review & editing. **Sadashiva Devadiga:** Conceptualization, Supervision, Writing – original draft, Writing – review & editing. **Arthur Endsley:** Formal analysis, Investigation, Methodology, Visualization, Writing – original draft, Writing – review & editing. **Angela Erb:** Formal analysis, Investigation, Methodology, Visualization, Writing – original draft, Writing – review & editing. **Mark Friedl:** Formal analysis, Investigation, Methodology, Visualization, Writing – original draft, Writing – review & editing. **Huilin Gao:** Formal analysis, Investigation, Methodology, Visualization, Writing – original draft, Writing – review & editing. **Louis Giglio:** Formal analysis, Investigation, Methodology, Visualization, Writing – original draft, Writing – review & editing. **Josh M. Gray:** Formal analysis, Investigation, Methodology, Visualization, Writing – original draft, Writing – review & editing. **Dorothy Hall:** Formal analysis, Investigation, Methodology, Visualization, Writing – original draft, Writing – review & editing. **Glynn Hulley:** Formal analysis, Investigation, Methodology, Visualization, Writing – original draft, Writing – review & editing. **John Kimball:** Formal analysis, Investigation, Methodology, Visualization, Writing – original draft, Writing – review & editing. **Yuri Knyazikhin:** Formal analysis, Investigation, Methodology, Visualization, Writing – original draft, Writing – review & editing. **Alexei Lyapustin:** Formal analysis, Investigation, Methodology, Visualization, Writing – original draft, Writing – review & editing. **Ranga B. Myneni:** Formal analysis, Investigation, Methodology, Visualization, Writing – original draft, Writing – review & editing. **Praveen Noojipady:** Formal analysis, Investigation, Methodology, Visualization, Writing – original draft, Writing – review & editing. **Jiabin Pu:** Formal analysis, Investigation, Methodology, Visualization, Writing – original draft, Writing – review & editing. **George Riggs:** Formal analysis, Investigation, Methodology, Visualization, Writing – original draft, Writing – review & editing. **Sudipta Sarkar:** Formal analysis, Investigation, Methodology, Visualization, Writing – original draft, Writing – review & editing. **Crystal Schaaf:** Formal analysis, Investigation, Methodology, Visualization, Writing – original draft, Writing – review & editing. **Deep Shah:** Formal analysis, Investigation, Methodology, Visualization, Writing – original draft, Writing – review & editing. **Khuong H. Tran:** Formal analysis, Investigation, Methodology, Visualization, Writing – original draft, Writing – review & editing. **Eric Vermote:** Formal analysis, Investigation, Methodology, Visualization, Writing – original draft, Writing – review & editing. **Dongdong Wang:** Formal analysis, Investigation, Methodology, Visualization, Writing – original draft, Writing – review & editing. **Zhuosen Wang:** Formal analysis, Investigation, Methodology, Visualization, Writing – original draft, Writing – review & editing. **Aisheng Wu:** Formal analysis, Investigation, Methodology, Visualization, Writing – original draft, Writing – review & editing. **Yongchang Ye:** Formal analysis, Investigation, Methodology, Visualization, Writing – original draft, Writing – review & editing. **Yu Shen:** Formal analysis, Investigation, Methodology, Visualization, Writing – original draft, Writing – review & editing. **Shuai Zhang:** Formal analysis, Investigation, Methodology, Visualization, Writing – original draft, Writing – review & editing. **Xiaoyang Zhang:** Formal analysis, Investigation, Methodology, Visualization, Writing – original draft, Writing – review & editing. **Maosheng Zhao:** Formal analysis, Investigation, Methodology, Visualization, Writing – original draft, Writing – review & editing. **Carol Davidson:** Formal analysis, Investigation, Methodology, Visualization, Writing – original draft, Writing – review & editing. **Robert Wolfe:** Writing – review & editing.

Declaration of Competing Interest

The authors declare the following financial interests/personal relationships which may be considered as potential competing interests:

Miguel O. Román reports financial support was provided by NASA. Crystal Schaaf reports previously serving as an editor for RSE.

Data availability

As a review article this references other studies for which the data availability would be described in those studies.

Acknowledgements

Alexei Lyapustin acknowledges support from NASA MODIS Maintenance and from NASA NNH20ZDA001N-SNPPSP programs. Arthur Endsley acknowledges contributions related to MOD17 were supported by a grant from NASA (80NSSC22K0198). John Kimball, Arthur Endsley and Maosheng Zhao (PI) acknowledge support from NASA Suomi National Polar-Orbiting Partnership (NPP) and the Joint Polar Satellite System (JPSS) satellites standard products for earth system data records (grant 80NSSC22K0198). Crystal Schaaf acknowledges support from NASA Grants 80NSSC21K1906 and 80NSSC21K1964. Dongdong Wang acknowledges support from NASA under Grant 80NSSC21K0701. Huilin Gao acknowledges support for the GWR product by NASA grant 80NSSC22K1552. Xiaoyang Zhang acknowledges support by NASA grant 80NSSC21K1962. Zhuosen Wang acknowledges support from NASA's Terra, Aqua, Suomi-NPP, and NOAA-20 program grant 80NSSC22K0199.

Appendix A. Appendix

Table A1
Comparison of MODIS and METImage band specifications.

MODIS			METImage MetOp - SG		
Band	Spectral Range [μm]	Spatial Resolution [m]	Band	Spectral Range [μm]	Spatial Resolution [m]
1	0.620–0.670	250	VII-12	0.658–0.678	500
2	0.841–0.876	250	VII-17	0.855–0.875	500
3	0.459–0.479	500			
4	0.545–0.565	500	VII-8	0.545–0.565	500
5	1.230–1.250	500	VII-22	1.23–1.25	500
6	1.628–1.652	500	VII-24	1.62–1.64	500
7	2.105–2.155	500			
8	0.405–0.420	1000			
9	0.438–0.448	1000	VII-4	0.428–0.458	500
10	0.438–0.493	1000	VII-4	0.428–0.458	500
11	0.526–0.536	1000			
12	0.546–0.556	1000	VII-8	0.545–0.565	500
13	0.662–0.672	1000	VII-12	0.658–0.678	500
14	0.673–0.683	1000	VII-12	0.658–0.678	500
15	0.743–0.753	1000	VII-15	0.7465–0.7565	500
16	0.862–0.877	1000	VII-17	0.855–0.875	500
17	0.890–0.920	1000	VII-20	0.904–0.924	500
18	0.931–0.941	1000			
19	0.915–0.965	1000	VII-20	0.904–0.924	500
20	3.660–3.840	1000	VII-26	3.65–3.83	500
21	3.929–3.989	1000	VII-28	3.929–3.989	500
22	3.929–3.989	1000	VII-28	3.929–3.989	500
23	4.020–4.080	1000	VII-30	4.02–4.08	500
24	4.433–4.498	1000			
25	4.482–4.549	1000			
26	1.360–1.390	1000	VII-23	1.355–1.395	500
27	6.535–6.895	1000	VII-33	6.54–6.91	500
28	7.175–7.475	1000	VII-34	7.18–7.47	500
29	8.400–8.700	1000	VII-35	8.395–8.685	500
30	9.580–9.880	1000			
31	10.780–11.280	1000	VII-37	10.44–10.94	500
32	11.770–12.270	1000	VII-39	11.77–12.27	500
33	13.185–13.485	1000	VII-40	13.19–13.5	500
34	13.485–13.785	1000	VII-40	13.19–13.5	500
35	13.785–14.085	1000			
36	14.085–14.385	1000			

Table A2
Comparison of MODIS and Sentinel-3 SLSTR band specifications.

MODIS			Sentinel-3 SLSTR		
Band	Spectral Range [μm]	Spatial Resolution [m]	Band	Spectral Range [μm]	Spatial Resolution [m]
1	0.620–0.670	250	S2	0.649845–0.669095	500
2	0.841–0.876	250	S3	0.8577–0.8783	500
3	0.459–0.479	500			
4	0.545–0.565	500	S1	0.54464–0.5639	500
5	1.230–1.250	500			
6	1.628–1.652	500	S5	1.58306–1.64374	500
7	2.105–2.155	500			
8	0.405–0.420	1000			
9	0.438–0.448	1000			
10	0.438–0.493	1000			
11	0.526–0.536	1000			

(*continued on next page*)

Table A2 (*continued*)

MODIS			Sentinel-3 SLSTR		
Band	Spectral Range [μm]	Spatial Resolution [m]	Band	Spectral Range [μm]	Spatial Resolution [m]
12	0.546–0.556	1000	S1	0.54464–0.5639	500
13	0.662–0.672	1000	S2	0.649845–0.669095	500
14	0.673–0.683	1000			
15	0.743–0.753	1000			
16	0.862–0.877	1000	S3	0.8577–0.8783	500
17	0.890–0.920	1000			
18	0.931–0.941	1000			
19	0.915–0.965	1000			
20	3.660–3.840	1000	S7	3.543–3.941	1000
			F1	3.543–3.941	1000
21	3.929–3.989	1000	S7	3.543–3.941	1000
			F1	3.543–3.941	1000
22	3.929–3.989	1000	S7	3.543–3.941	1000
			F1	3.543–3.941	1000
23	4.020–4.080	1000			
24	4.433–4.498	1000			
25	4.482–4.549	1000			
26	1.360–1.390	1000	S4	1.3644–1.3852	500
27	6.535–6.895	1000			
28	7.175–7.475	1000			
29	8.400–8.700	1000			
30	9.580–9.880	1000			
31	10.780–11.280	1000	S8	10.466–11.242	1000
			F2	10.466–11.242	1000
32	11.770–12.270	1000	S9	11.57–12.475	1000
33	13.185–13.485	1000			
34	13.485–13.785	1000			
35	13.785–14.085	1000			
36	14.085–14.385	1000			

Table A3
Comparison of MODIS and Sentinel-3 OLCI band specifications.

MODIS			Sentinel-3 OLCI		
Band	Spectral Range [μm]	Spatial Resolution [m]	Band	Spectral Range [μm]	Spatial Resolution [m]
1	0.620–0.670	250	Oa07	0.615–0.625	300
			Oa08	0.66–0.67	300
			Oa09	0.67–0.6775	300
2	0.841–0.876	250	Oa17	0.855–0.875	300
3	0.459–0.479	500			
4	0.545–0.565	500	Oa06	0.555–0.565	300
5	1.230–1.250	500			
6	1.628–1.652	500			
7	2.105–2.155	500			
8	0.405–0.420	1000	Oa01	0.3925–0.4075	300
			Oa02	0.4075–0.4175	300
9	0.438–0.448	1000	Oa03	0.4375–0.4475	300
10	0.438–0.493	1000	Oa03	0.4375–0.4475	300
			Oa04	0.485–0.495	300
11	0.526–0.536	1000			
12	0.546–0.556	1000	Oa06	0.555–0.565	300
13	0.662–0.672	1000	Oa08	0.66–0.67	300
			Oa09	0.67–0.6775	300
14	0.673–0.683	1000	Oa09	0.67–0.6775	300
			Oa10	0.6775–0.685	300
15	0.743–0.753	1000	Oa12	0.75–0.7575	300
16	0.862–0.877	1000	Oa17	0.855–0.875	300
17	0.890–0.920	1000	Oa18	0.88–0.89	300
			Oa19	0.895–0.905	300
18	0.931–0.941	1000	Oa20	0.93–0.95	300
19	0.915–0.965	1000	Oa20	0.93–0.95	300
20	3.660–3.840	1000			
21	3.929–3.989	1000			
22	3.929–3.989	1000			
23	4.020–4.080	1000			
24	4.433–4.498	1000			
25	4.482–4.549	1000			
26	1.360–1.390	1000			
27	6.535–6.895	1000			
28	7.175–7.475	1000			

(*continued on next page*)

Table A3 (*continued*)

MODIS			Sentinel-3 OLCI		
Band	Spectral Range [μm]	Spatial Resolution [m]	Band	Spectral Range [μm]	Spatial Resolution [m]
29	8.400–8.700	1000			
30	9.580–9.880	1000			
31	10.780–11.280	1000			
32	11.770–12.270	1000			
33	13.185–13.485	1000			
34	13.485–13.785	1000			
35	13.785–14.085	1000			
36	14.085–14.385	1000			

Table A4
Comparison of MODIS and AVHRR/3 band specifications.

MODIS			AVHRR/3		
Band	Spectral Range [μm]	Spatial Resolution [m]	Band	Spectral Range [μm]	Spatial Resolution [m]
1	0.620–0.670	250	1	0.58–0.68	1100
2	0.841–0.876	250	2	0.725–1.10	1100
3	0.459–0.479	500			
4	0.545–0.565	500			
5	1.230–1.250	500			
6	1.628–1.652	500			
7	2.105–2.155	500			
8	0.405–0.420	1000			
9	0.438–0.448	1000			
10	0.438–0.493	1000			
11	0.526–0.536	1000			
12	0.546–0.556	1000			
13	0.662–0.672	1000	1	0.58–0.68	1100
14	0.673–0.683	1000	1	0.58–0.68	1100
15	0.743–0.753	1000	2	0.725–1.10	1100
16	0.862–0.877	1000	2	0.725–1.10	1100
17	0.890–0.920	1000	2	0.725–1.10	1100
18	0.931–0.941	1000	2	0.725–1.10	1100
19	0.915–0.965	1000	2	0.725–1.10	1100
20	3.660–3.840	1000	3	3.55–3.93	1100
21	3.929–3.989	1000	3	3.55–3.93	1100
22	3.929–3.989	1000	3	3.55–3.93	1100
23	4.020–4.080	1000			
24	4.433–4.498	1000			
25	4.482–4.549	1000			
26	1.360–1.390	1000			
27	6.535–6.895	1000			
28	7.175–7.475	1000			
29	8.400–8.700	1000			
30	9.580–9.880	1000			
31	10.780–11.280	1000	4	10.3–11.3	1100
32	11.770–12.270	1000	5	11.5–12.5	1100
33	13.185–13.485	1000			
34	13.485–13.785	1000			
35	13.785–14.085	1000			
36	14.085–14.385	1000			

References

Alonso, K., Bachmann, M., Burch, K., Carmona, E., Cerra, D., De los Reyes, R., Dietrich, D., Heiden, U., Hölderlin, A., Ickes, J., Knodt, U., 2019. Data products, quality and validation of the DLR earth sensing imaging spectrometer (DESIS). Sensors. 19 (20), 4471. https://doi.org/10.3390/s19204471.

Baret, F., Morissette, J.T., Fernandes, R.A., Champeaux, J.L., Myneni, R.B., Chen, J., Plummer, S., Weiss, M., Bacour, C., Garrigues, S., Nickeson, J.E., 2006. Evaluation of the representativeness of networks of sites for the global validation and intercomparison of land biophysical products: proposition of the CEOS-BELMANIP. IEEE Trans. Geosci. Remote Sens. 44 (7), 1794–1803. https://doi.org/10.1109/TGRS.2006.876030.

Benedict, T.D., Brown, J.F., Boyte, S.P., Howard, D.M., Fuchs, B.A., Wardlow, B.D., Tadesse, T., Evenson, K.A., 2021. Exploring VIIRS continuity with MODIS in an expedited capability for monitoring drought-related vegetation conditions. Remote Sens. 13 (6), 1210. https://doi.org/10.3390/rs13061210.

Biemans, H., Haddeland, I., Kabat, P., Ludwig, F., Hutjes, R.W.A., Heinke, J., Von Bloh, W., Gerten, D., 2011. Impact of reservoirs on river discharge and irrigation water supply during the 20th century. Water Resour. Res. 47 (3) https://doi.org/10.1029/2009WR008929.

Board, S.S., National Academies of Sciences, Engineering, and Medicine, 2019. Thriving on our changing planet: A decadal strategy for Earth observation from space. National Academies Press. https://doi.org/10.17226/24938.

Boschetti, L., Stehman, S.V., Roy, D.P., 2016. A stratified random sampling design in space and time for regional to global scale burned area product validation. Remote Sens. Environ. 186, 465–478. https://doi.org/10.1016/j.rse.2016.09.016.

Boschetti, L., Roy, D.P., Giglio, L., Huang, H., Zubkova, M., Humber, M.L., 2019. Global validation of the collection 6 MODIS burned area product. Remote Sens. Environ. 235, 111490 https://doi.org/10.1016/j.rse.2019.111490.

Brown, L.A., Meier, C., Morris, H., Pastor-Guzman, J., Bai, G., Lerebourg, C., Gobron, N., Lanconelli, C., Clerici, M., Dash, J., 2020. Evaluation of global leaf area index and fraction of absorbed photosynthetically active radiation products over North America using Copernicus ground based observations for validation data. Remote Sens. Environ. 247, 111935 https://doi.org/10.1016/j.rse.2020.111935.

Cao, C., Sullivan, J., Maturi, E., Sapper, J., 2004. The effect of orbit drift on the calibration of the 3.7 μ m channel of the AVHRR onboard NOAA-14 and its impact

on night-time sea surface temperature retrievals. Int. J. Remote Sens. 25 (5), 975–986. https://doi.org/10.1080/0143116031000095899.
Cao, C., Xiong, X., Wu, A., Wu, X., 2008. Assessing the consistency of AVHRR and MODIS L1B reflectance for generating fundamental climate data records. J. Geophys. Res. Atmos. 113 (D9) https://doi.org/10.1029/2007JD009363.
Chakraborty, S., Oda, T., Kalb, V.L., Wang, Z., Román, M.O., 2023. Potentially underestimated gas flaring activities—a new approach to detect combustion using machine learning and NASA's Black marble product suite. Environ. Res. Lett. 18 (3), 035001 https://doi.org/10.1088/1748-9326/acb6a7.
Chen, J.M., Black, T.A., 1992. Defining leaf area index for non-flat leaves plant. Cell Environ. 15, 421–429. https://doi.org/10.1111/j.1365-3040.1992.tb00992.x.
Chen, C., Knyazikhin, Y., Park, T., Yan, K., Lyapustin, A., Wang, Y., Yang, B., Myneni, R. B., 2017. Prototyping of LAI and FPAR retrievals from MODIS multi-angle implementation of atmospheric correction (MAIAC) data. Remote Sens. 9 (4), 370. https://doi.org/10.3390/rs9040370.
Chen, C., Park, T., Wang, X., Piao, S., Xu, B., Chaturvedi, R.K., Fuchs, R., Brovkin, V., Ciais, P., Fensholt, R., Tømmervik, H., 2019. China and India lead in greening of the world through land-use management. Nat. Sustain. 2 (2), 122–129. https://doi.org/10.1038/s41893-019-0220-7.
Cleland, E.E., Allen, J.M., Crimmins, T.M., Dunne, J.A., Pau, S., Travers, S.E., Zavaleta, E. S., Wolkovich, E.M., 2012. Phenological tracking enables positive species responses to climate change. Ecology. 93 (8), 1765–1771. https://doi.org/10.1890/11-1912.1.
Cole, T.A., Wanik, D.W., Molthan, A.L., Román, M.O., Griffin, R.E., 2017. Synergistic use of nighttime satellite data, electric utility infrastructure, and ambient population to improve power outage detections in urban areas. Remote Sens. 9 (3), 286. https://doi.org/10.3390/rs9030286.
Cooper, M.J., Martin, R.V., Lyapustin, A.I., McLinden, C.A., 2018. Assessing snow extent data sets over North America to inform and improve trace gas retrievals from solar backscatter. Atmos. Meas. Tech. 11 (5), 2983–2994. https://doi.org/10.5194/amt-11-2983-2018.
Doelling, D.R., Morstad, D., Bhatt, R., Scarino, B., 2011. Algorithm Theoretical Basis Document (ATBD) for deep convective cloud (DCC) technique of calibrating GEO sensors with Aqua-MODIS for GSICS. http://gsics.nesdis.noaa.gov/pub/Development/AtbdCentral/GSICS_ATBD_DCC_NASA_2011_09.pdf (accessed 14 July 2023).
Doelling, D.R., Morstad, D., Scarino, B.R., Bhatt, R., Gopalan, A., 2012. The characterization of deep convective clouds as an invariant calibration target and as a visible calibration technique. IEEE Trans. Geosci. Remote Sens. 51 (3), 1147–1159. https://doi.org/10.1109/TGRS.2012.2225066.
Endsley, K.A., Zhao, M., Kimball, J.S., Devadiga, S., 2023. Continuity of global MODIS terrestrial primary productivity estimates in the VIIRS era using model-data fusion. Journal of geophysical research. Biogeosciences. 128 (9) https://doi.org/10.1029/2023JG007457 e2023JG007457.
Enenkel, M., Shrestha, R.M., Stokes, E., Roman, M., Wang, Z., Espinosa, M.T.M., Hajzmanova, I., Ginnetti, J., Vinck, P., 2019. Emergencies do not stop at night: advanced analysis of displacement based on satellite-derived nighttime light observations. IBM J. Res. Dev. 64 (1/2) https://doi.org/10.1147/JRD.2019.2954404, 8-1.
Friedrich, K., Grossman, R.L., Huntington, J., Blanken, P.D., Lenters, J., Holman, K.D., Gochis, D., Livneh, B., Prairie, J., Skeie, E., Healey, N.C., 2018. Reservoir evaporation in the Western United States: current science, challenges, and future needs. Bull. Am. Meteorol. Soc. 99 (1), 167–187. https://doi.org/10.1175/BAMS-D-15-00224.1.
Ganguly, S., Samanta, A., Schull, M.A., Shabanov, N.V., Milesi, C., Nemani, R.R., Knyazikhin, Y., Myneni, R.B., 2008a. Generating vegetation leaf area index earth system data record from multiple sensors. Part 2: implementation, analysis, and validation. Remote Sens. Environ. 112 (12), 4318–4332. https://doi.org/10.1016/j.rse.2008.07.013.
Ganguly, S., Schull, M.A., Samanta, A., Shabanov, N.V., Milesi, C., Nemani, R.R., Knyazikhin, Y., Myneni, R.B., 2008b. Generating vegetation leaf area index earth system data record from multiple sensors. Part 1: theory. Remote Sens. Environ. 112 (12), 4333–4343. https://doi.org/10.1016/j.rse.2008.07.014.
GCOS, 2022. Essential Climate Variables, Snow. https://gcos.wmo.int/en/essential-climate-variables/snow/ (accessed 27 February 2023).
Giglio, L., Loboda, T., Roy, D.P., Quayle, B., Justice, C.O., 2009. An active-fire based burned area mapping algorithm for the MODIS sensor. Remote Sens. Environ. 113 (2), 408–420. https://doi.org/10.1016/j.rse.2008.10.006.
Giglio, L., Boschetti, L., Roy, D.P., Humber, M.L., Justice, C.O., 2018. The collection 6 MODIS burned area mapping algorithm and product. Remote Sens. Environ. 217, 72–85. https://doi.org/10.1016/j.rse.2018.08.005.
Gillespie, A., Rokugawa, S., Matsunaga, T., Cothern, J.S., Hook, S., Kahle, A.B., 1998. A temperature and emissivity separation algorithm for advanced spaceborne thermal emission and reflection radiometer (ASTER) images. IEEE Trans. Geosci. Remote Sens. 36 (4), 1113–1126. https://doi.org/10.1109/36.700995.
Gray, J.M., Sulla-menashe, D., Friedl, M.A., 2019. User Guide to Collection 6 MODIS Land Cover Dynamics (MCD12Q2) Product. https://modis-land.gsfc.nasa.gov/pdf/MCD12Q2_Collection6_UserGuide.pdf (accessed 26 June 2023).
Guillevic, P.C., Biard, J.C., Hulley, G.C., Privette, J.L., Hook, S.J., Olioso, A., Göttsche, F. M., Radocinski, R., Román, M.O., Yu, Y., Csiszar, I., 2014. Validation of land surface temperature products derived from the visible infrared imaging radiometer suite (VIIRS) using ground-based and heritage satellite measurements. Remote Sens. Environ. 154, 19–37. https://doi.org/10.1016/j.rse.2014.08.013.
Guillevic, P., Gottsche, F., Nickeson, J., Hulley, G., Ghent, D., Yu, Y., Trigo, I.F., Hook, S., Sobrino, J.A., Remedios, J., Roman, M.O., Camacho, F., 2018. Land surface temperature product validation best practice protocol, version 1.1. In: Guillevic, P., Göttsche, F., Nickeson, J., Román, M. (Eds.), Best Practice for Satellite-Derived Land Product Validation: Land Product Validation Subgroup (WGCV/CEOS), 58. https://doi.org/10.5067/doc/ceoswgcv/lpv/lst.001.
Hall, D.K., Riggs, G.A., 2007. Accuracy assessment of the MODIS snow-cover products. Hydrol. Process. 21 (12), 1534–1547. https://doi.org/10.1002/hyp.6715.
Hall, D.K., Riggs, G.A., DiGirolamo, N.E., Román, M.O., 2019. Evaluation of MODIS and VIIRS cloud-gap-filled snow-cover products for production of an earth science data record. Hydrol. Earth Syst. Sci. 23, 5227–5241. https://doi.org/10.5194/hess-23-5227-2019.
Hammer, M.S., van Donkelaar, A., Li, C., Lyapustin, A., Sayer, A.M., Hsu, N.C., Levy, R. C., Garay, M.J., Kalashnikova, O.V., Kahn, R.A., Brauer, M., 2020. Global estimates and long-term trends of fine particulate matter concentrations (1998–2018). Environ. Sci. Technol. 54 (13), 7879–7890. https://doi.org/10.1021/acs.est.0c01764.
Hammer, M.S., Van Donkelaar, A., Martin, R.V., McDuffie, E.E., Lyapustin, A., Sayer, A. M., Hsu, N.C., Levy, R.C., Garay, M.J., Kalashnikova, O.V., Kahn, R.A., 2021. Effects of COVID-19 lockdowns on fine particulate matter concentrations. Sci. Adv. 7 (26), 7670. https://doi.org/10.1126/sciadv.abg7670.
Hilker, T., Lyapustin, A.I., Tucker, C.J., Sellers, P.J., Hall, F.G., Wang, Y., 2012. Remote sensing of tropical ecosystems: atmospheric correction and cloud masking matter. Remote Sens. Environ. 127, 370–384. https://doi.org/10.1016/j.rse.2012.08.035.
Holben, B.N., Eck, T.F., Slutsker, I.A., Tanré, D., Buis, J.P., Setzer, A., Vermote, E., Reagan, J.A., Kaufman, Y.J., Nakajima, Lavenu, F., 1998. AERONET—A federated instrument network and data archive for aerosol characterization. Remote Sens. Environ. 66 (1), 1–16.
Hu, G., Jia, L., Menenti, M., 2015. Comparison of MOD16 and LSA-SAF MSG evapotranspiration products over Europe for 2011. Remote Sens. Environ. 156, 510–526. https://doi.org/10.1016/j.rse.2014.10.017.
Hulley, G., Ghent, D. (Eds.), 2019. Taking the Temperature of the Earth: Steps towards Integrated Understanding of Variability and Change. Elsevier.
Hulley, G.C., Hook, S.J., Hughes, C., 2012a. MODIS MOD21 land surface temperature and emissivity algorithm theoretical basis document. Jet Propulsion Laboratory, California Institute of Technology, National Aeronautics and Space Administration (NASA), Pasadena, CA.
Hulley, G.C., Hughes, C.G., Hook, S.J., 2012b. Quantifying uncertainties in land surface temperature and emissivity retrievals from ASTER and MODIS thermal infrared data. J. Geophys. Res.-Atmos. 117 (D23) https://doi.org/10.1029/2012JD018506.
Hulley, G.C., Malakar, N.K., Islam, T., Freepartner, R.J., 2017. NASA's MODIS and VIIRS land surface temperature and emissivity products: A long-term and consistent earth system data record. IEEE J. Sel. Top. Appl. Earth Obs. Remote Sens. 11 (2), 522–535. https://doi.org/10.1109/JSTARS.2017.2779330.
Hulley, G.C., Göttsche, F.M., Rivera, G., Hook, S.J., Freepartner, R.J., Martin, M.A., Cawse-Nicholson, K., Johnson, W.R., 2021. Validation and quality assessment of the ECOSTRESS level-2 land surface temperature and emissivity product. IEEE Trans. Geosci. Remote Sens. 60, 1–23. https://doi.org/10.1109/TGRS.2021.3079879.
Islam, T., Hulley, G.C., Malakar, N.K., Radocinski, R.G., Guillevic, P.C., Hook, S.J., 2017. A physics-based algorithm for the simultaneous retrieval of land surface temperature and emissivity from VIIRS thermal infrared data. IEEE Trans. Geosci. Remote Sens. 55 (1), 563–576. https://doi.org/10.1109/TGRS.2016.2611566.
Jones, M.O., Running, S.W., Kimball, J.S., Robinson, N.P., Allred, B.W., 2020. Terrestrial primary productivity indicators for inclusion in the National Climate Indicators System. Clim. Chang. 163, 1855–1868. https://doi.org/10.1007/s10584-018-2155-9.
Justice, C.O., Vermote, E., Townshend, J.R.G., DeFries, R., Roy, D.R., Hall, D.K., Salomonson, V.V., Privette, J.L., Riggs, G., Strahler, A., Lucht, W., Myneni, R., Knyazikhin, Y., Running, S.W., Nemani, R.R., Wan, Z., Huete, A., van Leeuwen, W., Wolfe, R.E., Giglio, L., Muller, J.-P., Lewis, P., Barnsley, M.J., 1998. The moderate resolution imaging Spectroradiometer (MODIS): Land remote sensing for global change research. Trans. IEEE Geosci. Remote Sens. 36 (4), 1228–1249.
Justice, C.O., Townshend, J.R.G., Vermote, E.F., Masuoka, E., Wolfe, R.E., El Saleous, N., Roy, D.P., Morisette, J.T., 2002. An overview of MODIS Land data processing and product status. Remote Sens. Environ. 83, 1–15. https://doi.org/10.1016/S0034-4257(02)00084-6.
Justice, C.O., Román, M.O., Csiszar, I., Vermote, E.F., Wolfe, R.E., Hook, S.J., Friedl, M., Wang, Z., Schaaf, C.B., Miura, T., Tschudi, M., 2013. Land and cryosphere products from Suomi NPP VIIRS: overview and status. J. Geophys. Res. Atmos. 118 (17), 9753–9765. https://doi.org/10.1002/jgrd.50771.
Kalb, V., Kosar, B., Collado-Vega, Y., Davidson, C., 2023. Aurora detection from nighttime lights for earth and space science applications. Earth Space Sci. 10 (1) e2022EA002513.
Kalluri, S., Cao, C., Heidinger, A., Ignatov, A., Key, J., Smith, T., 2021. The advanced very high resolution radiometer: contributing to earth observations for over 40 years. Bull. Am. Meteorol. Soc. 102 (2), E351–E366. https://doi.org/10.1175/BAMS-D-20-0088.1.
King, M.D., Platnick, S., 2018. The earth observing system (EOS). In: Liang, S. (Ed.), Comprehensive Remote Sensing, vol. 1. Elsevier, pp. 7–26.
Kloog, I., Chudnovsky, A.A., Just, A.C., Nordio, F., Koutrakis, P., Coull, B.A., Lyapustin, A., Wang, Y., Schwartz, J., 2014. A new hybrid spatio-temporal model for estimating daily multi-year PM2. 5 concentrations across northeastern USA using high resolution aerosol optical depth data. Atmos. Environ. 95, 581–590. https://doi.org/10.1016/j.atmosenv.2014.07.014.
Knyazikhin, Y., 1999. MODIS leaf area index (LAI) and fraction of photosynthetically active radiation absorbed by vegetation (FPAR) product (MOD 15) algorithm theoretical basis document. https://modis.gsfc.nasa.gov/data/atbd/atbd_mod15.pdf (accessed 26 June 2023).
Knyazikhin, Y., Myneni, R., 2018. VIIRS leaf area index (LAI) and fraction of photosynthetically active radiation absorbed by vegetation (FPAR) user guide. https

://lpdaac.usgs.gov/documents/126/VNP15_User_Guide.pdf (accessed 26 June 2023).
Knyazikhin, Y., Martonchik, J.V., Myneni, R.B., Diner, D.J., Running, S.W., 1998. Synergistic algorithm for estimating vegetation canopy leaf area index and fraction of absorbed photosynthetically active radiation from MODIS and MISR data. J. Geophys. Res. Atmos. 103 (D24), 32257–32275. https://doi.org/10.1029/98JD02462.
Leidman, S., Rennermalm, Å.K., Lathrop, R.G., Cooper, M., 2021. Terrain-based shadow correction method for assessing supraglacial features on the Greenland ice sheet. Front. Remote Sens. 20 https://doi.org/10.3389/frsen.2021.690474.
Levin, N., Kyba, C.C., Zhang, Q., de Miguel, A.S., Román, M.O., Li, X., Portnov, B.A., Molthan, A.L., Jechow, A., Miller, S.D., Wang, Z., 2020. Remote sensing of night lights: A review and an outlook for the future. Remote Sens. Environ. 237, 111443 https://doi.org/10.1016/j.rse.2019.111443.
Li, Y., Gao, H., Zhao, G., Tseng, K.H., 2020. A high-resolution bathymetry dataset for global reservoirs using multi-source satellite imagery and altimetry. Remote Sens. Environ. 244, 111831.
Li, Y., Zhao, G., Shah, D., Zhao, M., Sarkar, S., Devadiga, S., Zhao, B., Zhang, S., Gao, H., 2021. Nasa's modis/viirs global water reservoir product suite from moderate resolution remote sensing data. Remote Sens. 13 (4), 565. https://doi.org/10.3390/rs13040565.
Li, R., Wang, D., Liang, S., Jia, A.L., Wang, Z., 2022a. Estimating global downward shortwave radiation from VIIRS data using a transfer-learning neural network. Remote Sens. Environ. 274, 112999 https://doi.org/10.1016/j.rse.2022.112999.
Li, T., Zhu, Z., Wang, Z., Román, M.O., Kalb, V.L., Zhao, Y., 2022b. Continuous monitoring of nighttime light changes based on daily NASA's Black marble product suite. Remote Sens. Environ. 282, 113269 https://doi.org/10.1016/j.rse.2022.113269.
Li, R., Wang, D., Liang, S., 2023a. Comparison between deep learning architectures for the 1 km, 10/15-min estimation of downward shortwave radiation from AHI and ABI. Remote Sens. Environ. 295, 113697 https://doi.org/10.1016/j.rse.2023.113697.
Li, Y., Zhao, G., Allen, G.H., Gao, H., 2023b. Diminishing storage returns of reservoir construction. Nat. Commun. 14 (1), 3203. https://doi.org/10.1038/s41467-023-38843-5.
Liu, Y., Yu, Y., Yu, P., Göttsche, F.M., Trigo, I.F., 2015. Quality assessment of S-NPP VIIRS land surface temperature product. Remote Sens. 7 (9), 12215–12241.
Liu, Y., Sun, Q., Wang, Z., Li, Z., Román, M.O., Schaaf, C., 2017a. VIIRS BRDF, Albedo, and NBAR Product Algorithm Theoretical Basis Document (ATBD). NASA Goddard Space Flight Center. https://lpdaac.usgs.gov/documents/194/VNP43_ATBD_V1.pdf.
Liu, Y., Wang, Z., Sun, Q., Erb, A.M., Li, Z., Schaaf, C.B., Zhang, X., Román, M.O., Scott, R.L., Zhang, Q., Novick, K.A., 2017b. Evaluation of the VIIRS BRDF, albedo and NBAR products suite and an assessment of continuity with the long term MODIS record. Remote Sens. Environ. 201, 256–274. https://doi.org/10.1016/j.rse.2017.09.020.
Liu, Y., Hill, M.J., Zhang, X., Wang, Z., Richardson, A.D., Hufkens, K., Filippa, G., Baldocchi, D.D., Ma, S., Verfaillie, J., Schaaf, C.B., 2017c. Using data from Landsat, MODIS, VIIRS and PhenoCams to monitor the phenology of California oak/grass savanna and open grassland across spatial scales. Agric. For. Meteorol. 237, 311–325. https://doi.org/10.1016/j.agrformet.2017.02.026.
Lyapustin, A., Wang, Y., Laszlo, I., Korkin, S., 2012. Improved cloud and snow screening in MAIAC aerosol retrievals using spectral and spatial analysis. Atmos. Meas. Tech. 5 (4), 843–850. https://doi.org/10.5194/amt-5-843-2012.
Lyapustin, A., Alexander, M.J., Ott, L., Molod, A., Holben, B., Susskind, J., Wang, Y., 2014a. Observation of mountain lee waves with MODIS NIR column water vapor. Geophys. Res. Lett. 41 (2), 710–716. https://doi.org/10.1002/2013GL058770.
Lyapustin, A., Wang, Y., Xiong, X., Meister, G., Platnick, S., Levy, R., Franz, B., Korkin, S., Hilker, T., Tucker, J., Hall, F., 2014b. Scientific impact of MODIS C5 calibration degradation and C6+ improvements. Atmos. Meas. Tech. 7 (12), 4353–4365. https://doi.org/10.5194/amt-7-4353-2014.
Lyapustin, A., Wang, Y., Korkin, S., Huang, D., 2018. MODIS collection 6 MAIAC algorithm. Atmos. Meas. Tech. 11 (10), 5741–5765. https://doi.org/10.5194/amt-11-5741-2018.
Lyapustin, A., Wang, Y., Korkin, S., Kahn, R., Winker, D., 2019. MAIAC thermal technique for smoke injection height from MODIS. IEEE Geosci. Remote Sens. Lett. 17 (5), 730–734. https://doi.org/10.1109/LGRS.2019.2936332.
Lyapustin, A., Zhao, F., Wang, Y., 2021a. A comparison of multi-angle implementation of atmospheric correction and MOD09 daily surface reflectance products from MODIS. Front. Remote Sens. 2, 712093 https://doi.org/10.3389/frsen.2021.712093.
Lyapustin, A., Wang, Y., Go, S., Choi, M., Korkin, S., Huang, D., Knyazikhin, Y., Blank, K., Marshak, A., 2021b. Atmospheric correction of DSCOVR EPIC: version 2 MAIAC algorithm. Front. Remote Sens. 2, 748362 https://doi.org/10.3389/frsen.2021.748362.
Lyapustin, A., Wang, Y., Choi, M., Xiong, X., Angal, A., Wu, A., Doelling, D.R., Bhatt, R., Go, S., Korkin, S., Franz, B., Meister, G., Sayer, A.M., Roman, M., Holz, R.E., Meyer, K., Gleason, J., Levy, R., 2023. Calibration of the SNPP and NOAA 20 VIIRS sensors for continuity of the MODIS climate data records. Remote Sens. Environ. 295, 113717 https://doi.org/10.1016/j.rse.2023.113717.
Ma, L., Bo, J., Li, X., Fang, F., Cheng, W., 2019. Identifying key landscape pattern indices influencing the ecological security of inland river basin: the middle and lower reaches of Shule River basin as an example. Sci. Total Environ. 674, 424–438. https://doi.org/10.1016/j.scitotenv.2019.04.107.
Makkaroon, P., Tong, D.Q., Li, Y., Hyer, E.J., Xian, P., Kondragunta, S., Campbell, P.C., Tang, Y., Baker, B.D., Cohen, M.D., Darmenov, A., 2023. Development and evaluation of a North America ensemble wildfire air quality forecast: Initial application to the 2020 Western United States "Gigafire. J. Geophys. Res. Atmos. 128 (22) e2022JD037298.
Malakar, N.K., Hulley, G.C., 2016. A water vapor scaling model for improved land surface temperature and emissivity separation of MODIS thermal infrared data. Remote Sens. Environ. 182, 252–264. https://doi.org/10.1016/j.rse.2016.04.023.
Martins, V.S., Lyapustin, A., Wang, Y., Giles, D.M., Smirnov, A., Slutsker, I., Korkin, S., 2019. Global validation of columnar water vapor derived from EOS MODIS-MAIAC algorithm against the ground-based AERONET observations. Atmos. Res. 225, 181–192. https://doi.org/10.1016/j.atmosres.2019.04.005.
Masuoka, E., Roy, D., Wolfe, R., Morisette, J., Sinno, S., Teague, M., Saleous, N., Devadiga, S., Justice, C.O., Nickeson, J., 2011. MODIS land data products: Generation, quality assurance and validation. In: Ramachandran, B., Justice, C., Abrams, M. (Eds.), Land Remote Sensing and Global Environmental Change: NASA's Earth Observing System and the Science of ASTER and MODIS. Springer, New York, pp. 509–531. https://doi.org/10.1007/978-1-4419-6749-7_22.
Menne, M.J., Durre, I., Vose, R.S., Gleason, B.E., Houston, T.G., 2012. An overview of the global historical climatology network-daily database. J. Atmos. Ocean. Technol. 29 (7), 897–910. https://doi.org/10.1175/JTECH-D-11-00103.1.
Mildrexler, D., Yang, Z., Cohen, W.B., Bell, D.M., 2016. A forest vulnerability index based on drought and high temperatures. Remote Sens. Environ. 173, 314–325. https://doi.org/10.1016/j.rse.2015.11.024.
Miura, T., Muratsuchi, J., Vargas, M., 2018. Assessment of cross-sensor vegetation index compatibility between VIIRS and MODIS using near-coincident observations. J. Appl. Remote. Sens. 12 (4), 045004 https://doi.org/10.1117/1.JRS.12.045004.
MODIS Land, 2023a. MODIS Land Science Team. https://modis-land.gsfc.nasa.gov/ (accessed 25 July 2023).
MODIS Land, 2023b. Status for: Snow Cover/Sea Ice (MOD10/29). https://modis-land.gsfc.nasa.gov/ValStatus.php?ProductID=MOD10/29 (accessed 27 February 2023).
Monteith, J.L., 1972. Solar radiation and productivity in tropical ecosystems. J. Appl. Ecol. 9 (3), 747–766. https://doi.org/10.2307/2401901.
Moon, M., Zhang, X., Henebry, G.M., Liu, L., Gray, J.M., Melaas, E.K., Friedl, M.A., 2019. Long-term continuity in land surface phenology measurements: A comparative assessment of the MODIS land cover dynamics and VIIRS land surface phenology products. Remote Sens. Environ. 226, 74–92. https://doi.org/10.1016/j.rse.2019.03.034.
Morisette, J.T., Privette, J.L., Justice, C.O., 2002. A framework for the validation of MODIS land products. Remote Sens. Environ. 83, 77–96. https://doi.org/10.1016/S0034-4257(02)00088-3.
Morisette, J.T., Richardson, A.D., Knapp, A.K., Fisher, J.I., Graham, E.A., Abatzoglou, J., Wilson, B.E., Breshears, D.D., Henebry, G.M., Hanes, J.M., Liang, L., 2009. Tracking the rhythm of the seasons in the face of global change: phenological research in the 21st century. Front. Ecol. Environ. 7 (5), 253–260. https://doi.org/10.1890/070217.
Mu, Q., Zhao, M., Running, S.W., 2011. Improvements to a MODIS global terrestrial evapotranspiration algorithm. Remote Sens. Environ. 115 (8), 1781–1800. https://doi.org/10.1016/j.rse.2011.02.019.
Murdock, H.E.G., André, T., Appavou, F., Brown, A., Epp, B., Kondev, B., McCrone, A., Musolino, E., Ranalder, L., 2019. Renewables 2019 Global Status Report. Secretariat, Paris, France. https://www.ren21.net/wp-content/uploads/2019/05/gsr_2019_full_report_en.pdf (accessed 11 November 2020).
Murphy, R.E., 2006. The NPOESS preparatory project. In: Qu, J.J., Gao, W., Kafatos, M., Murphy, R.E., Salomonson, V.V. (Eds.), Earth Science Satellite Remote Sensing, Science and Instruments, vol. 1. Springer, Berlin, Heidelberg, pp. 182–198. https://doi.org/10.1007/978-3-540-37293-6_10.
Myneni, R.B., Park, T., 2015. MODIS collection 6 (C6) LAI/FPAR product user's guide. https://lpdaac.usgs.gov/documents/624/MOD15_User_Guide_V6.pdf (accessed 26 June 2023).
Myneni, R., Knyazikhin, Y., Park, T., 2015. MYD15A2H MODIS/Aqua Leaf Area Index/FPAR 8-Day L4 Global 500m SIN Grid V006. NASA EOSDIS Land Processes DAAC. https://doi.org/10.5067/MODIS/MYD15A2H.006.
NASA, 2021. NASA's Scientific Visualization Studio, Terra Orbit Drift, Visualizations by Kel Elkins, Released on 24 September 2021. https://svs.gsfc.nasa.gov/4938?_ga=2.253003200.898334881.1636566917-528527108.1601490090 (accessed 27 February 2023).
NASA CEOS, 2023. Land Product Validation Subgroup: CEOS Validation Hierarchy. https://lpvs.gsfc.nasa.gov/ (accessed 14 September 2023).
NASA LDOPE, 2023. Golden Tile Time Series. https://landweb.modaps.eosdis.nasa.gov/cgi-bin/QS/ts/timeseries2.cgi?GENPLOT=1 (accessed 25 July 2023).
Ohmura, A., Dutton, E.G., Forgan, B., Fröhlich, C., Gilgen, H., Hegner, H., Heimo, A., König-Langlo, G., McArthur, B., Müller, G., Philipona, R., 1998. Baseline surface radiation network (BSRN/WCRP): new precision radiometry for climate research. Bull. Am. Meteorol. Soc. 79 (10), 2115–2136. https://doi.org/10.1175/1520-0477(1998)079<2115:BSRNBW>2.0.CO;2.
Padilla, M., Wheeler, J., Tansey, K., 2018. ESA CCI ECV Fire Disturbance: D4.1.1. Product Validation Report, Version 2.1. https://eu-west-1.staged.climate.esa.int/media/documents/Fire_cci_D4.1.1_PVR_v2.1.pdf (accessed 26 June 2023).
Park, T., Yan, K., Chen, C., Xu, B., Knyazikhin, Y., Myneni, R., 2017. VIIRS Leaf Area Index (LAI) and Fraction of Photosynthetically Active Radiation Absorbed by Vegetation (FPAR) Product Algorithm Theoretical Basis Document (ATBD). https://lpdaac.usgs.gov/documents/125/VNP15_ATBD.pdf (accessed 26 June 2023).
Parkinson, C.L., 2022. The earth-observing aqua satellite Mission: 20 years and counting. Earth Space Sci. 9 (9) https://doi.org/10.1029/2022EA002481 e2022EA002481.
Pedelty, J., Devadiga, S., Masuoka, E., Brown, M., Pinzon, J., Tucker, C., Vermote, E., Prince, S., Nagol, J., Justice, C., Roy, D., 2007. Generating a long-term land data record from the AVHRR and MODIS instruments. In: IEEE international Geoscience

and remote sensing Symposium, pp. 1021–1025. https://doi.org/10.1109/IGARSS.2007.4422974.
Pu, J., Yan, K., Zhou, G., Lei, Y., Zhu, Y., Guo, D., Li, H., Xu, L., Knyazikhin, Y., Myneni, R.B., 2020. Evaluation of the MODIS LAI/FPAR algorithm based on 3D-RTM simulations: A case study of grassland. Remote Sens. 12 (20), 3391. https://doi.org/10.3390/rs12203391.
Richardson, M., Cowtan, K., Millar, R.J., 2018. Global temperature definition affects achievement of long-term climate goals. Environ. Res. Lett. 13 (5), 054004 https://doi.org/10.1088/1748-9326/aab305.
Riggs, G.A., Hall, D.K., 2019. NASA S-NPP VIIRS Snow Cover Products Collection 2 User Guide Version 1.0. https://nsidc.org/data/viirs/documents (accessed 7 July 2023).
Riggs, G.A., Hall, D.K., 2020. Continuity of MODIS and VIIRS snow cover extent data products for development of an earth science data record. Remote Sens. 12, 3781. https://doi.org/10.3390/rs12223781.
Riggs, G.A., Hall, D.K., Román, M.O., 2019a. VIIRS/NPP Snow Cover Daily L3 Global 375m SIN Grid, Version 1. NASA National Snow and Ice Data Center Distributed Active Archive Center. https://doi.org/10.5067/VIIRS/VNP10A1.001.
Riggs, G.A., Hall, D.K., Román, M.O., 2019b. MODIS Snow Products Collection 6.1 User Guide, Version 1.0. https://nsidc.org/sites/default/files/c61_modis_snow_user_guide.pdf (accessed 6 February 2023).
Román, M.O., Stokes, E.C., 2015. Holidays in lights: tracking cultural patterns in demand for energy services. Earth's Future 3 (6), 182–205. https://doi.org/10.1002/2014EF000285.
Román, M.O., Riggs, G.A., Hall, D.K., 2017. VIIRS/NPP Snow Cover 6-Min L2 Swath 375m, Version 1. https://nsidc.org/sites/default/files/vnp10-v001-userguide.pdf (accessed 6 February 2023).
Román, M.O., Wang, Z., Sun, Q., Kalb, V., Miller, S.D., Molthan, A., Schultz, L., Bell, J., Stokes, E.C., Pandey, B., Seto, K.C., 2018. NASA's Black marble nighttime lights product suite. Remote Sens. Environ. 210, 113–143. https://doi.org/10.1016/j.rse.2018.03.017.
Román, M.O., Stokes, E.C., Shrestha, R., Wang, Z., Schultz, L., Carlo, E.A.S., Sun, Q., Bell, J., Molthan, A., Kalb, V., Ji, C., 2019. Satellite-based assessment of electricity restoration efforts in Puerto Rico after Hurricane Maria. PLoS One 14 (6), e0218883. https://doi.org/10.1371/journal.pone.0218883.
Roy, D.P., Borak, J.S., Devadiga, S., Wolfe, R.E., Zheng, M., Descloitres, J., 2002. The MODIS land product quality assessment approach. Remote Sens. Environ. 83 (1–2), 62–76. https://doi.org/10.1016/S0034-4257(02)00087-1.
Roy, P.S., Ramachandran, R.M., Paul, O., Thakur, P.K., Ravan, S., Behera, M.D., Sarangi, C., Kanawade, V.P., 2022. Anthropogenic land use and land cover changes—A review on its environmental consequences and climate change. J. Indian Soc. Remote Sens. 50 (8), 1615–1640. https://doi.org/10.1007/s12524-022-01569-w.
Running, S.W., Nemani, R.R., Heinsch, F.A., Zhao, M., Reeves, M., Hashimoto, H., 2004. A continuous satellite-derived measure of global terrestrial primary production. Bioscience 54 (6), 547–560. https://doi.org/10.1641/0006-3568(2004)054[0547:ACSMOG]2.0.CO;2.
Salomonson, V.V., Barnes, W., Masuoka, E.J., 2006. Introduction to MODIS and an overview of associated activities. In: Qu, J.J., Gao, W., Kafatos, M., Murphy, R.E., Salomonson, V.V. (Eds.), Earth Science Satellite Remote Sensing, vol. 1. Springer, Berlin, Heidelberg, pp. 12–32. https://doi.org/10.1007/978-3-540-37293-6_2.
Schneider, P., Hook, S.J., 2010. Space observations of inland water bodies show rapid surface warming since 1985. Geophys. Res. Lett. 37 (22) https://doi.org/10.1029/2010GL045059.
Schutgens, N., Sayer, A.M., Heckel, A., Hsu, C., Jethva, H., De Leeuw, G., Leonard, P.J., Levy, R.C., Lipponen, A., Lyapustin, A., North, P., 2020. An AeroCom–AeroSat study: intercomparison of satellite AOD datasets for aerosol model evaluation. Atmos. Chem. Phys. 20 (21), 12431–12457. https://doi.org/10.5194/acp-20-12431-2020.
Skakun, S., Justice, C.O., Vermote, E., Roger, J.C., 2018. Transitioning from MODIS to VIIRS: an analysis of inter-consistency of NDVI data sets for agricultural monitoring. Int. J. Remote Sens. 39 (4), 971–992. https://doi.org/10.1080/01431161.2017.1395970.
Souza, V.D.A., Roberti, D.R., Ruhoff, A.L., Zimmer, T., Adamatti, D.S., Gonçalves, L.G.G. D., Diaz, M.B., Alves, R.D.C.M., Moraes, O.L.D., 2019. Evaluation of MOD16 algorithm over irrigated rice paddy using flux tower measurements in southern Brazil. Water 11 (9), 1911. https://doi.org/10.3390/w11091911.
Strahler, A., Lucht, W., Schaaf, C., Tsang, T., Gao, F., Li, X., Muller, J.P., Lewis, P., Barnsley, M., 1999. MODIS BRDF / Albedo Product: Algorithm Theoretical Basis Document (ATBD) Version 5.0. NASA Goddard Space Flight Center. https://modis.gsfc.nasa.gov/data/atbd/atbd_mod09.pdf.
Su, X., Cao, M., Wang, L., Gui, X., Zhang, M., Huang, Y., Zhao, Y., 2023. Validation, intercomparison, and usage recommendation of six latest VIIRS and MODIS aerosol products over the ocean and land on the global and regional scales. Sci. Total Environ. 884, 163794 https://doi.org/10.1016/j.scitotenv.2023.163794.
Sun, Q., Wang, Z., Li, Z., Erb, A., Schaaf, C.L.B., 2017. Evaluation of the global MODIS 30 arc-second spatially and temporally complete snow-free land surface albedo and reflectance anisotropy dataset. Int. J. Appl. Earth Obs. Geoinf. 58, 36–49. https://doi.org/10.1016/j.jag.2017.01.011.
Susskind, J., Schmidt, G.A., Lee, J.N., Iredell, L., 2019. Recent global warming as confirmed by AIRS. Environ. Res. Lett. 14 (4), 044030.
Tang, R., Shao, K., Li, Z.L., Wu, H., Tang, B.H., Zhou, G., Zhang, L., 2015. Multiscale validation of the 8-day MOD16 evapotranspiration product using flux data collected in China. IEEE J. Sel. Top. Appl. Earth Obs. Remote Sens. 8 (4), 1478–1486. https://doi.org/10.1109/JSTARS.2015.2420105.
Thapa, S., Chhetri, P.K., Klein, A.G., 2019. Cross-comparison between MODIS and VIIRS snow cover products for the 2016 hydrological year. Climate. 7 (4), 57. https://doi.org/10.3390/cli7040057.
Tong, R., Parajka, J., Komma, J., Blöschl, G., 2020. Mapping snow cover from daily collection 6 MODIS products over Austria. J. Hydrol. 590, 125548 https://doi.org/10.1016/j.jhydrol.2020.125548.
Tonooka, H., 2005. Atmospheric correction of MODIS thermal infrared bands by water vapor scaling method. Remote Sens. Clouds Atmos. X 5979, 152–163. SPIE. https://doi.org/10.1117/12.629290.
Tran, K.H., Zhang, X., Ketchpaw, A.R., Wang, J., Ye, Y., Shen, Y., 2022. A novel algorithm for the generation of gap-free time series by fusing harmonized Landsat 8 and Sentinel-2 observations with PhenoCam time series for detecting land surface phenology. Remote Sens. Environ. 282, 113275 https://doi.org/10.1016/j.rse.2022.113275.
Van Donkelaar, A., Hammer, M.S., Bindle, L., Brauer, M., Brook, J.R., Garay, M.J., Hsu, N.C., Kalashnikova, O.V., Kahn, R.A., Lee, C., Levy, R.C., 2021. Monthly global estimates of fine particulate matter and their uncertainty. Environ. Sci. Technol. 55 (22), 15287–15300. https://doi.org/10.1021/acs.est.1c05309.
Vargas, M., Miura, T., Shabanov, N., Kato, A., 2013. An initial assessment of Suomi NPP VIIRS vegetation index EDR. J. Geophys. Res. Atmos. 118 (22), 12–301. https://doi.org/10.1002/2013JD020439.
Vermote, E., Kaufman, Y.J., 1995. Absolute calibration of AVHRR visible and near-infrared channels using ocean and cloud views. Int. J. Remote Sens. 16 (13), 2317–2340. https://doi.org/10.1080/01431169508954561.
VIIRS Land, 2022a. VIIRS NASA Land Surface Temperature and Emissivity Product Validation. https://viirsland.gsfc.nasa.gov/Val/LST_Val.html (accessed 25 July 2023).
VIIRS Land, 2022b. VIIRS Land Validation Status. https://viirsland.gsfc.nasa.gov/Val_overview.html (accessed 27 February 2023).
VIIRS Land, 2022c. Suomi NPP VIIRS Land, VIIRS NASA Snow Cover Product Validation. https://viirsland.gsfc.nasa.gov/Val/Snow_Val.html (accessed 27 February 2023).
Wang, D., Morton, D., Masek, J., Wu, A., Nagol, J., Xiong, X., Levy, R., Vermote, E., Wolfe, R., 2012. Impact of sensor degradation on the MODIS NDVI time series. Remote Sens. Environ. 119, 55–61. https://doi.org/10.1016/j.rse.2011.12.001.
Wang, D., Liang, S., Zhang, Y., Gao, X., Brown, M.G., Jia, A., 2020. A new set of MODIS land products (MCD18): downward shortwave radiation and photosynthetically active radiation. Remote Sens. 12 (1), 168. https://doi.org/10.3390/rs12010168.
Wang, D., Liang, S., Li, R., Jia, A., 2021a. A synergic study on estimating surface downward shortwave radiation from satellite data. Remote Sens. Environ. 264, 112639 https://doi.org/10.1016/j.rse.2021.112639.
Wang, Z., Román, M.O., Kalb, V.L., Miller, S.D., Zhang, J., Shrestha, R.M., 2021b. Quantifying uncertainties in nighttime light retrievals from Suomi-NPP and NOAA-20 VIIRS day/night band data. Remote Sens. Environ. 263, 112557.
Wang, Z., Shrestha, R.M., Román, M.O., Kalb, V.L., 2022. NASA's black marble multiangle nighttime lights temporal composites. IEEE Geosci. Remote Sens. Lett. 19, 1–5. https://doi.org/10.1109/LGRS.2022.3176616.
Wei, J., Li, Z., Lyapustin, A., Sun, L., Peng, Y., Xue, W., Su, T., Cribb, M., 2021. Reconstructing 1-km-resolution high-quality PM2. 5 data records from 2000 to 2018 in China: spatiotemporal variations and policy implications. Remote Sens. Environ. 252, 112136 https://doi.org/10.1016/j.rse.2020.112136.
Xiong, X., Barnes, W., 2006. An overview of MODIS radiometric calibration and characterization. Adv. Atmos. Sci. 23, 69–79. https://doi.org/10.1007/s00376-006-0008-3.
Xiong, X., Sun, J., Barnes, W., Salomonson, V., Esposito, J., Erives, H., Guenther, B., 2007. Multiyear on-orbit calibration and performance of Terra MODIS reflective solar bands. IEEE Trans. Geosci. Remote Sens. 45 (4), 879–889. https://doi.org/10.1109/TGRS.2006.890567.
Xiong, X., Angal, A., Chang, T., Chiang, K., Lei, N., Li, Y., Sun, J., Twedt, K., Wu, A., 2020. MODIS and VIIRS calibration and characterization in support of producing long-term high-quality data products. Remote Sens. 12 (19), 3167. https://doi.org/10.3390/rs12193167.
Xu, B., Park, T., Yan, K., Chen, C., Zeng, Y., Song, W., Yin, G., Li, J., Liu, Q., Knyazikhin, Y., Myneni, R.B., 2018. Analysis of global LAI/FPAR products from VIIRS and MODIS sensors for spatio-temporal consistency and uncertainty from 2012–2016. Forests 9 (2), 73. https://doi.org/10.3390/f9020073.
Yan, K., Park, T., Yan, G., Chen, C., Yang, B., Liu, Z., Nemani, R.R., Knyazikhin, Y., Myneni, R.B., 2016. Evaluation of MODIS LAI/FPAR product collection 6. Part 1: consistency and improvements. Remote Sens. 8 (5), 359. https://doi.org/10.3390/rs8050359.
Yan, K., Park, T., Chen, C., Xu, B., Song, W., Yang, B., Zeng, Y., Liu, Z., Yan, G., Knyazikhin, Y., Myneni, R.B., 2018. Generating global products of LAI and FPAR from SNPP-VIIRS data: theoretical background and implementation. IEEE Trans. Geosci. Remote Sens. 56 (4), 2119–2137. https://doi.org/10.1109/TGRS.2017.2775247.
Yan, K., Pu, J., Park, T., Xu, B., Zeng, Y., Yan, G., Weiss, M., Knyazikhin, Y., Myneni, R.B., 2021. Performance stability of the MODIS and VIIRS LAI algorithms inferred from analysis of long time series of products. Remote Sens. Environ. 260, 112438 https://doi.org/10.1016/j.rse.2021.112438.
Yao, J., Liu, H., Huang, J., Gao, Z., Wang, G., Li, D., Yu, H., Chen, X., 2020. Accelerated dryland expansion regulates future variability in dryland gross primary production. Nat. Commun. 11, 1665. https://doi.org/10.1038/s41467-020-15515-2.
Ye, Y., Zhang, X., Shen, Y., Wang, J., Crimmins, T., Scheifinger, H., 2022. An optimal method for validating satellite-derived land surface phenology using in-situ observations from national phenology networks. ISPRS J. Photogramm. Remote Sens. 194, 74–90. https://doi.org/10.1016/j.isprsjprs.2022.09.018.
Zhang, X., 2015. Reconstruction of a complete global time series of daily vegetation index trajectory from long-term AVHRR data. Remote Sens. Environ. 156, 457–472. https://doi.org/10.1016/j.rse.2014.10.012.

Zhang, X., Friedl, M.A., Schaaf, C.B., Strahler, A.H., Hodges, J.C., Gao, F., Reed, B.C., Huete, A., 2003. Monitoring vegetation phenology using MODIS. Remote Sens. Environ. 84 (3), 471–475. https://doi.org/10.1016/S0034-4257(02)00135-9.

Zhang, S., Gao, H., Naz, B.S., 2014. Monitoring reservoir storage in South Asia from multisatellite remote sensing. Water Resour. Res. 50 (11), 8927–8943. https://doi.org/10.1002/2014WR015829.

Zhang, K., Kimball, J.S., Running, S.W., 2016. A review of remote sensing based actual evapotranspiration estimation. Wiley Interdiscip. Rev. Water 3 (6), 834–853. https://doi.org/10.1002/wat2.1168.

Zhang, X., Liu, L., Yan, D., 2017a. Comparisons of global land surface seasonality and phenology derived from AVHRR, MODIS, and VIIRS data. J. Geophys. Res. Biogeosci. 122 (6), 1506–1525. https://doi.org/10.1002/2017JG003811.

Zhang, X., Wang, J., Gao, F., Liu, Y., Schaaf, C., Friedl, M., Yu, Y., Jayavelu, S., Gray, J., Liu, L., Yan, D., 2017b. Exploration of scaling effects on coarse resolution land surface phenology. Remote Sens. Environ. 190, 318–330. https://doi.org/10.1016/j.rse.2017.01.001.

Zhang, X., Jayavelu, S., Liu, L., Friedl, M.A., Henebry, G.M., Liu, Y., Schaaf, C.B., Richardson, A.D., Gray, J., 2018. Evaluation of land surface phenology from VIIRS data using time series of PhenoCam imagery. Agric. For. Meteorol. 256, 137–149. https://doi.org/10.1016/j.agrformet.2018.03.003.

Zhang, K., Zhu, G., Ma, J., Yang, Y., Shang, S., Gu, C., 2019. Parameter analysis and estimates for the MODIS evapotranspiration algorithm and multiscale verification. Water Resour. Res. 55 (3), 2211–2231. https://doi.org/10.1029/2018WR023485.

Zhang, H., Zhang, F., Che, T., Wang, S., 2020a. Comparative evaluation of VIIRS daily snow cover product with MODIS for snow detection in China based on ground observations. Sci. Total Environ. 724, 138156 https://doi.org/10.1016/j.scitotenv.2020.138156.

Zhang, X., Wang, J., Henebry, G.M., Gao, F., 2020b. Development and evaluation of a new algorithm for detecting 30 m land surface phenology from VIIRS and HLS time series. ISPRS J. Photogramm. Remote Sens. 161, 37–51. https://doi.org/10.1016/j.isprsjprs.2020.01.012.

Zhang, X., Gao, F., Wang, J., Ye, Y., 2021. Evaluating a spatiotemporal shape-matching model for the generation of synthetic high spatiotemporal resolution time series of multiple satellite data. Int. J. Appl. Earth Obs. Geoinf. 104, 102545 https://doi.org/10.1016/j.jag.2021.102545.

Zhao, M., Heinsch, F.A., Nemani, R.R., Running, S.W., 2005. Improvements of the MODIS terrestrial gross and net primary production global data set. Remote Sens. Environ. 95 (2), 164–176. https://doi.org/10.1016/j.rse.2004.12.011.

Zhao, M., Running, S.W., Nemani, R.R., 2006. Sensitivity of moderate resolution imaging Spectroradiometer (MODIS) terrestrial primary production to the accuracy of meteorological reanalyses. Journal of geophysical research. Biogeosciences. 111 (G1) https://doi.org/10.1029/2004JG000004.

Zhao, G., Gao, H., Cai, X., 2020. Estimating lake temperature profile and evaporation losses by leveraging MODIS LST data. Remote Sens. Environ. 251, 112104 https://doi.org/10.1016/j.rse.2020.112104.

Zhao, G., Li, Y., Zhou, L., Gao, H., 2022. Evaporative water loss of 1.42 million global lakes. Nat. Commun. 13 (1), 3686. https://doi.org/10.1038/s41467-022-31125-6.

Zhu, Z., Piao, S., Myneni, R.B., Huang, M., Zeng, Z., Canadell, J.G., Ciais, P., Sitch, S., Friedlingstein, P., Arneth, A., Cao, C., 2016. Greening of the earth and its drivers. Nat. Clim. Chang. 6 (8), 791–795. https://doi.org/10.1038/nclimate3004.

Zubkova, M., Boschetti, L., Abatzoglou, J.T., Giglio, L., 2022. Fire regions as environmental niches: A new paradigm to define potential fire regimes in Africa and Australia. Journal of geophysical research. Biogeosciences. 127 (8) https://doi.org/10.1029/2021JG006694 e2021JG006694.